12-2009

Effects of Overload and Underload on Internal Strains/Stresses and Crack Closure during Fatigue-Crack Propagation

Soo Yeol Lee
University of Tennessee - Knoxville

To the Graduate Council:

I am submitting herewith a dissertation written by Soo Yeol Lee entitled "Effects of Overload and Underload on Internal Strains/Stresses and Crack Closure during Fatigue-Crack Propagation." I have examined the final electronic copy of this dissertation for form and content and recommend that it be accepted in partial fulfillment of the requirements for the degree of Doctor of Philosophy, with a major in Materials Science and Engineering.

Peter K. Liaw, Major Professor

We have read this dissertation and recommend its acceptance:

Hahn Choo, Yanfei Gao, John D. Landes

Accepted for the Council:

Carolyn R. Hodges

Vice Provost and Dean of the Graduate School

(Original signatures are on file with official student records.)

To the Graduate Council:

I am submitting herewith a dissertation written by Soo Yeol Lee entitled "Effects of Overload and Underload on Internal Strains/Stresses and Crack Closure during Fatigue-Crack Propagation." I have examined the final electronic copy of this dissertation for form and content and recommend that it be accepted in partial fulfillment of the requirements for the degree of Doctor of Philosophy, with a major in Materials Science and Engineering.

Peter K. Liaw
Major Professor

We have read this dissertation
and recommend its acceptance:

Hahn Choo

Yanfei Gao

John D. Landes

Accepted for the Council:

Carolyn R. Hodges
Vice Provost and Dean of the Graduate School

(Original signatures are on file with official student records.)

Effects of Overload and Underload on Internal Strains/Stresses and Crack Closure during Fatigue-Crack Propagation

A Dissertation
Presented for the
Doctor of Philosophy
Degree
The University of Tennessee, Knoxville

Soo Yeol Lee
December 2009

DEDICATION

This dissertation is dedicated to my wife, Namsoon Kang, my daughter, Julia Sehyun Lee, my parents, Won Seok Lee and Young Sook Kim, my brother, Shin Gu Lee, my sister (and her husband), Hyun Joo Lee (Dae Young Kim), my father-and mother-in-law, Ok Nam Kang and Jeong A Kim, my brothers-in-law, Hui Su Kang and Nam Gu Kang, for always believing me, encouraging me, and supporting me in achieving my goals.

ACKNOWLEDGEMENTS

I am deeply indebted to many people who have helped me during my Ph.D. study. My advisors, Dr. Peter K. Liaw and Dr. Hahn Choo, has been kindly helping me with my research throughout these years, providing abundant environments and resources for me to extend my potentials, and encouraging me to successfully develop my academic capabilities and interpersonal skills. I would like to thank Dr. Yanfei Gao for his help in understanding general aspects of the finite-element simulations. I would like to thank Dr. John D. Landes for his good suggestions and helpful discussions on the fatigue study. Special thanks should be given to Dr. Camden R. Hubbard at the Oak Ridge National Laboratory (ORNL), Dr. Ronald B. Rogge at the Chalk River Laboratories, and Dr. Edward C. Oliver at the ISIS Facility, Rutherford Appleton Laboratory, for their great help on conducting the neutron experiments and giving good suggestions on my paper writings. I would like to thank Dr. Ke An, Dr. Anna Paradowska, Dr. Michael Gharghouri, Dr. Donald W. Brown, Dr. John H. Root, Dr. Gene E. Ice, Dr. Rozaliya Barabash, Dr. Tom Holden, Dr. Yandong Wang, and Dr. Jin-Seok Chung for their valuable suggestions/comments in this work. I also want to thank Dr. Dwaine L. Klarstrom and Dr. Lee M. Pike from Haynes International, Inc. for providing me with unlimited support in all aspects.

I would like to express my appreciations to many people who helped me during this study. I am grateful to Dr. Thomas R. Watkins and Mr. William Bailey for the neutron experiments at the Oak Ridge National Laboratory; Mr. Douglas E. Fielden,

Mr. Frank Holiway, Mr. Greg Jones, and Mr. John Dunlap in machine and electronic shops at The University of Tennessee. I would also like to thank our group members and friends who helped and encouraged me to achieve my goals during my Ph.D. study. Many thanks are given to Mr. E-Wen Huang, Mr. Feng Jiang, Ms. Li Li, Ms. Zhenzhen Yu, Dr. Michael Benson, Dr. Yulin Lu, Dr. Yinan Sun, Dr. Wanchuck Woo, Dr. Jiawan Tian, Dr. Liang Wu, Dr. Fengxiao Liu, Dr. Dongchun Qiao, Dr. Gongyao Wang, Dr. Wenhui Jiang, Dr. Sheng Cheng, Dr. Cang Fan, Dr. Hongqi Li, Ms. Shenyan Huang, Mr. Zhenke Teng, Ms. Lu Huang, Mr. Wei Wu, Mr. Jun Mo Kim, and Mr. Jin ha Huang.

This project is supported by the US National Science Foundation (NSF) International Materials Institutes (IMI) Program under contract DMR-0231320, with Drs. U. Venkateswaran, D. Finotello, and C. Huber as the program directors. Experiments at the ISIS Pulsed Neutron and Muon Source were supported by a beamtime allocation from the Science and Technology Facilities Council. I am grateful to the beam time from the Canadian Neutron Beam Centre, National Research Council Canada. Measurements at the neutron residual stress mapping facility (NRSF2) are sponsored by the Assistant Secretary for Energy Efficiency and Renewable Energy, Office of FreedomCAR and Vehicle Technologies, as a part of the High Temperature Materials Laboratory User Program, Oak Ridge National Laboratory, managed by UT-Battelle, LLC, for the U.S. Department of Energy under contract number, DE-AC05-00OR22725.

ABSTRACT

The overload and/or underload occurring during constant-amplitude fatigue-crack growth result in the retardation and/or acceleration in the crack-growth rate, making it difficult to predict the crack-propagation behavior and fatigue lifetime. Although there have been numerous investigations to account for these transient crack-growth behavior, the phenomena are still not completely understood.

Neutron and X-ray diffraction, and electric-potential measurements were employed to investigate these transient crack-growth micromechanisms; gain a thorough understanding of the crack-tip deformation and fracture behaviors under applied loads; and establish a quantitative relationship between the crack-tip-driving force and crack-growth behavior. Five different fatigue-crack-growth experiments (i.e., fatigued, tensile overloaded, compressive underloaded, tensile overloaded-compressive underloaded, and compressive underloaded-tensile overloaded) were performed to observe these transient crack-growth behaviors. The development of internal-strain distributions during variable-amplitude loadings, and the resultant residual-stress distributions around a crack tip were examined using neutron diffraction.

The effects of a single tensile overload on fatigue-crack growth were focused on probing the crack-growth-retardation micromechanisms. Neutron diffraction and polychromatic X-ray microdiffraction showed high dislocation densities and considerable crystallographic tilts near the crack tip immediately after the overload. The interactions between the overload-induced plastic zone and newly-developed fatigue-

plastic zone, and their influences on the evolution of residual-strain profiles are discussed.

Neutron-diffraction and electric-potential measurements provide *in-situ* observation of the crack-opening/closing processes and internal-stress distributions in the vicinity of the crack tip during real-time fatigue-crack propagation following a tensile overload. Immediately after applying a tensile overload, the crack-tip became blunt and the large compressive residual stresses were developed around the crack tip. In the retardation period after the tensile overloading, the combined effects of the crack-tip blunting at an overload point and compressive-residual stresses accompanying the crack closure induced the stress concentration at a blunting region until a maximum crack-arrest load was reached. Then, the stress concentration was transferred from the blunting region to actual crack-tip position with gradual crack opening, requiring a higher applied load. This observation of the stress-transfer phenomenon significantly promotes the fundamental understanding of overload-retardation phenomena. The post-overload crack-growth rates were normalized with the effective-stress-intensity-factor range, which suggests that it can be considered as the fatigue-crack-tip-driving force.

TABLE OF CONTENTS

LIST OF FIGURES

Chapter 1

1. Introduction

In terms of many fatigue-critical parts of structures, vehicles, and machines, fatigue-crack propagation under service conditions generally involves random or variable amplitude rather than constant-amplitude-loading conditions (Borrego et al., 2003). Sudden changes, e.g., overload and/or underload, in the constant-amplitude cyclic-loading patterns could complicate the plastic zone and distribution of the stress states near a fatigue crack, and give rise to a significant crack-growth retardation and/or acceleration, making it difficult to quantitatively predict the crack-propagation behavior and fatigue lifetime. Therefore, the accurate understanding of these load-interaction phenomena, i.e., overload and/or underload, are crucial to develop the damage-tolerance design and lifetime-prediction methodology.

The load-interaction effects under general variable-amplitude loading are highly complex. As a simplest case, the effects of a single tensile overload on fatigue-crack growth have extensively been studied since its discovery in the 1960s, because this sort of loading condition gives rise to the beneficial effects on the improvement in the fatigue lifetime. The application of a single tensile overload during fatigue-crack growth results in an instantaneous acceleration of the crack-growth rate, followed by a large

crack-growth retardation period, i.e., the crack-growth rate temporarily slows down, which increases the fatigue lifetime significantly. There have been numerous efforts to account for these crack-growth-retardation phenomena, which include the experimental studies (Elber, 1971; Wheeler, 1972; Jones, 1973; Gan & Weertman, 1981; Newman, 1981; Suresh, 1982; Suresh, 1983; Ward-Close et al., 1989; Shin & Hsu, 1993; Dougherty et al., 1997; Borrego et al., 2003; Makabe et al., 2004; Bichler & Pippan, 2007; Codrington & Kotousov, 2009) and computer simulation studies (Zhang et al., 1992; Pommier et al., 2002; Roychowdhury & Dodds, 2005; Singh et al., 2006). Among them, the plasticity-induced crack-closure concept suggested by Elber (1971) has been supported by many investigations. Elber introduced the effective-stress-intensity-factor range as a fatigue-crack-tip-driving force, emphasizing the significance of a crack-closure phenomenon in the wake of a crack. However, there exist many recent claims to deny the significance of crack closure (Vasudevan et al., 1992; Louat et al., 1993; Vasudevan et al., 1994; Sadananda et al., 1999; Zhang et al., 2005; Croft et al., 2007; Vallellano et al., 2009), which ultimately suggests a new approach of the fatigue-crack-tip-driving force. For instance, Sadananda et al. (1999) demonstrated that the perturbation of the stresses ahead of the crack tip is the major cause for the overload retardation, not due to the crack closure behind the crack tip, and suggested a new "unified approach" in which the maximum stress-intensity factor, K_{max}, and the stress-intensity-factor range, ΔK (= $K_{max} - K_{min}$), are considered as the two parameters that provide the two driving forces required for fatigue-crack growth. To summarize, the exact retardation micromechanism, fatigue-crack-tip-driving force, and the crack-

closure phenomenon in a fatigue wake still remain an open question. It might be due to experimental difficulties to measure quantitative strain/stress fields near a fatigue-crack tip under applied loads and to observe *in-situ* crack-tip deformation and failure phenomena during real-time fatigue experiments.

A crack-closure approach has played an important role in explaining many load-interaction effects on the fatigue-crack-growth behavior under variable-amplitude loading (Schijve & Arkema, 1976; Schijve 1988). The exact determination of crack opening and closing loads (or stresses) is important to predict the accurate crack-tip-driving force. Most of the experimental crack-closure measurements are based on the analysis of the specimen compliance, i.e., displacement/load (Elber, 1971; Liaw et al., 1982; Brahma et al., 1989; Yisheng et al., 1995). An alternative method to measure the crack closure is to use the direct-current-potential-drop (DCPD) technique. When a constant current is passed through the test specimen, the crack-mouth potential is measured. The higher potential means the longer crack length due to an increased resistivity of the material. If a crack closes and yields an electric contact between the fracture surfaces, a crack-closing (or opening) point should be determined from the curve of the applied load vs. potential during a single fatigue cycle. Using this method, an understanding of crack-tip deformation and fracture behaviors as well as the crack-closure phenomena during a single loading-unloading cycle can be enhanced from the observation of changes in the electric potential.

Neutron diffraction provides a unique tool in the study of mechanical behavior. The deep-penetration and volume-averaging capabilities of the neutron-diffraction

technique enable the spatially-resolved mapping of internal strain/stress distributions in the bulk sample *in situ* under applied loads. At the same time, the dislocation density can be carried out from the diffraction-peak-profile analyses (Mughrabi, 1983; Ungar et al., 1999; Barabash, 2001). On the other hand, polychromatic X-ray microdiffraction (PXM) is an emerging tool for studying the mesoscale structure and dynamics in materials. From the polychromatic methods combined with differential aperture X-ray microscopy (Larson et al., 2002), the local crystal phase, orientation (texture), and local defect distribution including elastic and plastic strain can be determined (Ice et al., 2005; Ice et al., 2006).

In summary, a careful investigation of the crack-tip deformation and failure characteristics *in situ* during real-time fatigue experiments, and simultaneous direct measurements of the stress/strain fields and plastic deformation near a fatigue-crack tip are crucial for a full understanding of the exact retardation micromechanism and fatigue-crack-tip-driving force, as well as the crack-closure phenomenon. In this aspect, neutron and X-ray diffraction, and electric-potential techniques will play a significant role in (i) probing the crack-tip deformation and failure phenomena under applied loads; (ii) studying the plastic deformation near the crack tip; (iii) examining the accurate crack-growth retardation micromechanisms; (iv) validating the effective-stress-intensity-factor range based on the crack-closure approach as the fatigue-crack-tip-driving force; and (v) establishing a quantitative relationship between the crack-tip-driving force and crack-propagation behavior.

Chapter 2

Overview of This Research

2.1 Background: Literature Review

The prediction, prevention, or postponement of failure in components and structures upon the basis of sound physics is not just an interesting topic for research, but is essential for the safe execution of our daily lives (James, 1998; Miller, 2003; Withers, 2007). In case of many engineering structures and components, they are often exposed to fatigue failure that occurs due to the repeated external application of stresses or strains. In practical applications of these materials, variable-amplitude fatigue loadings are generally involved, making it difficult to accurately evaluate the fatigue damage, and its influence on the crack-growth prediction and total fatigue lifetime (Borrego et al., 2003). Thus, the fundamental understanding of these fatigue-damage mechanisms is crucial for the improvement of the damage-tolerance design and development of new materials with excellent failure resistances.

Crack closure is one of the important mechanisms, which can explain many load-interaction effects on the fatigue-crack-growth behavior under variable-amplitude loading (Schijve & Arkema, 1976). Since Elber (1971) discovered the plasticity-induced crack closure, many researchers observed the various forms of fatigue-crack closure that are induced by a variety of mechanical, microstructural, and environmental

factors. These includes: oxide-induced crack closure, roughness-induced crack closure, viscous fluid-induced crack closure, transformation-induced crack closure. Several other mechanisms, which impede fatigue-crack growth, are found in advanced metallic systems, nonmetallic materials, and composites. These mechanisms include: crack deflection, crack-bridging or trapping, and crack shielding by particles. Figure 2.1 shows a schematic of the various mechanisms by which fatigue-crack growth can be retarded. It is noted that the evolution of different crack closure and retardation mechanisms is a process that can not be quantified precisely, because the crack-closure mechanism can be strongly influenced by even small variations in the path of the crack, environmental conditions, loading conditions, and testing procedures. Furthermore, it is often impossible to identify the individual contributions to the overall crack-growth rates from each of these retardation mechanisms. Therefore, it is not surprising that there exists considerable controversy and difference of opinion on the applicability and significance of different retardation mechanisms to fatigue-crack propagation.

In the late 1960s, Elber (1971) discovered the plasticity-induce crack-closure concept from the change in the compliance, i.e., displacement/load, of the test specimen during the load cycle. He interpreted this change as a variation in the crack length due to a gradual opening of a closed crack and used the compliance curve to measure the amount of crack closure. He suggested that crack-growth rates are influenced not only by the conditions in front of the crack tip, but also by the nature of crack-face contact behind the crack tip. This nature of crack closure in a crack wake is a natural result of

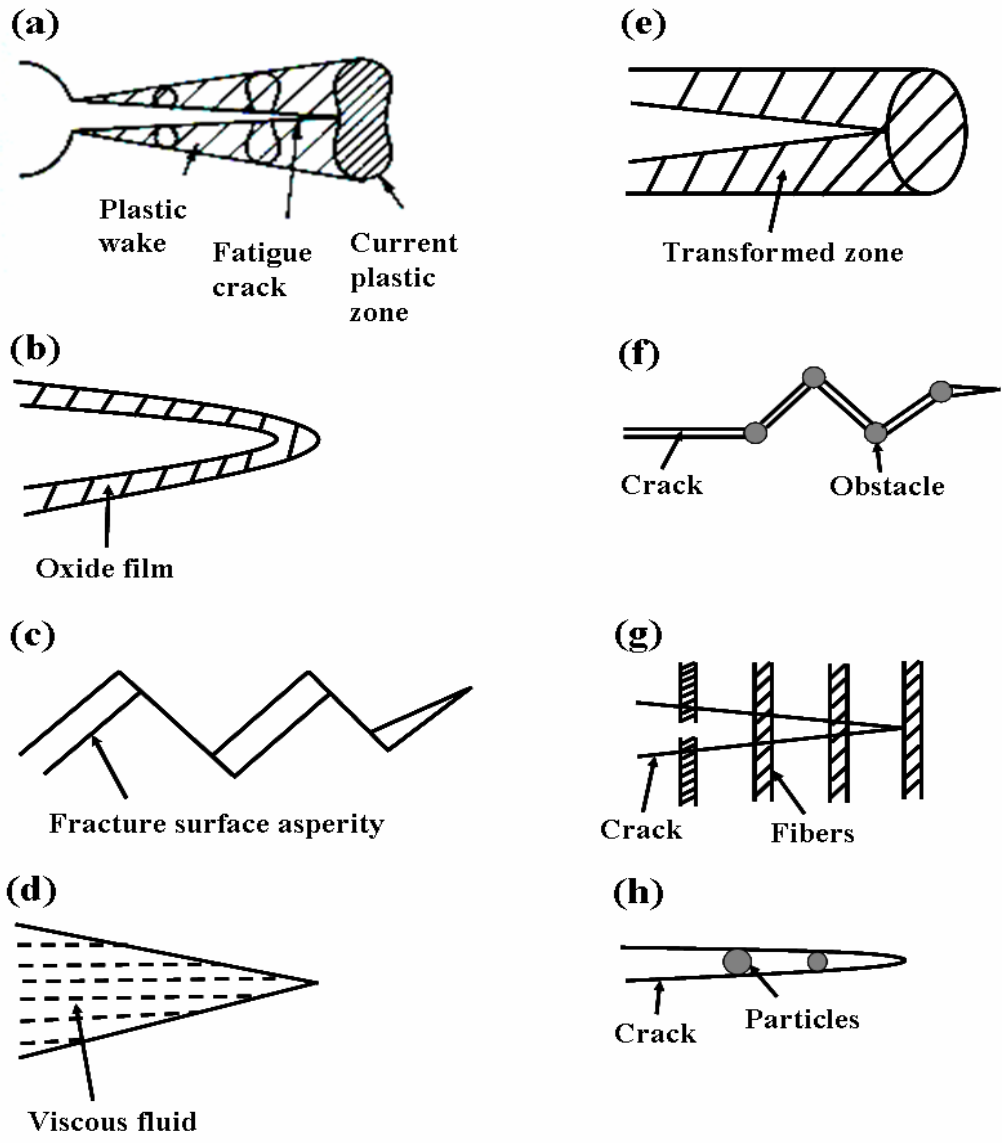

Figure 2.1: A schematic illustration of the mechanisms, which promote retardation of fatigue-crack growth in constant-amplitude fatigue. (a) plasticity-induced crack closure; (b) oxide-induce crack closure; (c) roughness-induced crack closure; (d) fluid-induced crack closure; (e) transformation-induced crack closure; (f) crack deflection; (g) crack-bridging by fibers; and (h) crack-bridging by particles. (Suresh, 1998)

such factors as the prior loading history, the length of crack, and the stress states. Elber reasoned that crack growth would not occur if the crack tip was closed, and the crack closure would reduce the driving force of fatigue-crack growth (i.e., the effective-stress-intensity-factor range, $\Delta K_{eff} = K_{max} - K_{op}$, where K_{max} and K_{op} denote the stress intensities at the maximum load and crack opening, respectively).

Investigations are not limited to experimental observations. Budiansky and Hutchinson (1978) employed the strip-yield hypothesis, generally attributed to the work by Dugdale (1960) and Barenblatt (1962), to model the plasticity-induced fatigue-crack closure. They showed that the residual stretch in the plastic crack wake caused the crack-face contact at a positive remote stress. They also found that cyclic strain hardening enhanced the effects of crack closure, whereas cyclic softening reduced closure levels. Their results rationalize the effect of R ratio on crack closure in the Paris regime of fatigue and are consistent with the experimental observations of Elber. Several investigations on the plasticity-induced crack closure have been reported by finite-element modeling. Ohji et al. (1975) used an incremental plasticity model incorporating kinematic hardening and crack growth simulated by extending the fatigue flaw in each stress cycle by a prescribed length which was equal to the finite-element mesh size. Although they did not explore the validity of ΔK_{eff} to characterize fatigue fracture over a wide range of R ratios or nominal ΔK values, they showed that the strain amplitude around a crack tip scaled with ΔK_{eff}. Newman (1976) also carried out two-dimensional finite-element analyses for the plane-stress condition using an incremental theory of plasticity. He found that the predicted results of the dependence of crack

closure on *R* ratio were in good agreement with the experimental investigations of Elber for aluminum alloys.

Oxide-induced crack closure is caused by the effects of environment on near-threshold fatigue-crack growth. Basically, fracture-surface oxidation gives rise to crack closure by reducing the driving force of fatigue-crack growth. Benoit et al. (1980) reported the differences between oxidation kinetics near the fatigue threshold and at higher growth rates qualitatively for austenitic stainless steels. Suresh et al. (1981) showed the first quantification of the effect of oxide layers formed within fatigue cracks on the threshold-fatigue behavior in ferritic-pearlitic, bainitic, and martensitic steels. They estimated the thickness of oxide layers on fracture surfaces using scanning-auger spectroscopy, and found that the oxide thickness within the fatigue crack is comparable to the scale of the crack-tip opening displacement near the threshold. Liaw et al. (1982) showed that oxide-induced crack closure is known to have a decisive effect on the near-threshold crack propagation of copper.

Roughness-induced crack closure is one of the mechanisms considering microstructural effects on fatigue-crack growth. This mechanism can provide an explanation for many anomalous phenomena of microstructure on fatigue-crack growth especially in the near-threshold regime. The stage I fatigue-crack-growth shows the serrated or faceted fracture morphology and an elevation in the crack-closure stress. It is known that the permanent plastic deformation ahead of the crack tip, as well as the possibility of slip irreversibility during unloading from the maximum stress, gives rise to the mismatch between the fracture-surface asperities. Gray et al. (1983) showed the

role of coarser grains and rough fracture surfaces in accelerating slower near-threshold crack-propagation rates at low load ratios as a result of the roughness-induced crack closure. They found that the coarser-grained material shows a significantly higher fatigue threshold at low load ratios. However, grain size has little influence on near-threshold fatigue-crack growth at high load ratios, supporting that the higher fatigue-crack resistance observed in the coarser-grained material at low load ratio is due to the roughness-induced crack closure.

Viscous fluid-induced crack closure has been the subject of considerable research interest in the effects of oil environments on the fatigue life. The mechanism is that viscous fluids penetrate within growing fatigue cracks by influencing the fatigue-crack-growth rate. Tzou et al. (1985) conducted an experimental study of the influence of dehumidified silicone and paraffin oils with different kinematic viscosities on fatigue-crack propagation in low-strength bainitic steels. They found that the net effect of oil environments on crack closure is strongly dependent upon several competing factors, such as the minimization of oxide-induced crack closure, environmental embrittlement, penetration of fluids within cracks, and the hydrodynamic wedging action. Thus, they concluded that it is difficult to extract general trends pertaining to the viscous fluid-induced crack closure.

It has been recognized that phase transformation at the fatigue-crack tip can lead to retardation in crack-growth rates (Pineau & Pelloux, 1974; Hornbogen, 1978). This is commonly referred to as the TRansformation-Induced Plasticity (TRIP) effect. The crack-tip phase transformation is analogous to the crack-tip plasticity in that

compressive residual stresses are induced within the nonlinear zone during cyclic tension. In both cases, the residual displacement is left in the crack wake, and acts to close the crack prematurely at a far-field tensile stress. Transformation-induced closure is strongly influenced by the size and geometry of the test specimen and of the fatigue crack.

Fatigue-crack deflection is viewed as one of the mechanisms for the toughening of brittle and ductile matrix composites. The obstacles in the path of the crack may cause an apparently beneficial resistance to crack growth by tilting or twisting the crack front (Faber & Evans, 1983). It was found that even small deflections in the path of a fatigue crack can lead to a reduction in crack-growth rates by several orders of magnitude, especially in the near-threshold fatigue regime (Suresh, 1998). When the crack tip is deflected from its nominal mode I growth direction, the effective driving force for crack growth is typically smaller than that of a straight crack of the same total length which is subjected to the same far-field. Therefore, the propagation of a deflected crack at the same rate as the corresponding straight crack requires an apparently larger driving force.

In composite materials, different failure mechanisms occur under the far-field tension. If the fiber strength is high enough, the tensile cracks advance completely through the matrix, and the crack faces are bridged by the fibers [Figure 2.1(g)]. On the other hand, if the fiber strength is lower than a certain critical value, the matrix failure results in a complete failure of the composite, because the fibers break in the wake of the advancing crack. Marshall and Cox (1987) developed a fracture-mechanics analysis

for fiber-reinforced composites where brittle matrix-cracking precedes the fiber failure and where only frictional bonding exists between the fibers and the matrix. While crack bridging promotes apparent improvements in the resistance to fatigue-crack growth in composites with continuous fiber reinforcements, the interaction of the crack tip with discontinuous particles is shown to have a strong effect on the geometry near the crack front and the crack-growth rate. The effect of particles on fatigue fracture is as follows: If the particles are impenetrable, they deflect the crack tip and cause a reduction in the effective ΔK. The particles, dispersed in the ductile matrix, trap the crack front, as shown in Fig. 2.1(h). Changes in the geometry of the crack front lead to apparent improvements in the fatigue-crack-growth resistance, depending on the size, shape, and distribution of the particles.

The determination of crack opening and closing stresses (or loads) is an important step in understanding the fatigue-crack-propagation behavior. A number of different experimental techniques, such as the compliance-based method (Liaw et al, 1982; Sunder, 1985; Roberson & Kirk, 1988; Donald & Paris, 1999), moiré interferometry method (Gray & Mackenzie, 1990; Fellow & Nowell, 2004), ultrasonic method (Rokhlin & Kim, 2003), potential-drop technique (Shih & Wei, 1974; Bachmann & Munz, 1976), acoustic-emission technique (Lee et al., 1986), photoelasticity method (Pacey et al, 2005), and synchrotron X-ray microtomography (Toda et al, 2004) are used to study the load at which the crack tip opens. Moreover, analytical models proposed by Budiansky and Hutchinson (1978), and Newman (1981) have also been developed to predict the crack opening and closing stresses. Many

researchers have simulated the plasticity-induced crack closure in the two-dimensional (2D) geometries using the finite-element analysis under plane-strain (Fleck, 1986; Wang et al., 2002; Pommier, 2002) or plane-stress conditions (McClung & Sehitoglu, 1989).

Most of the experimental crack-closure studies are based on the analysis of the specimen compliance. An estimate of the crack-opening stress level can be derived from a record of the stress (load) versus crack-opening displacement (COD) shown in Figure 2.2. The fatigue specimen has two linear and two nonlinear segments. The first linear segment (A-B) exhibits the elastic response of the partially closed-crack face. The nonlinear portion (B-C) represents the gradual crack-tip opening from the surface to interior. The beginning of the second linear response (C) marks the load level where the crack tip is fully open, and the linear segment (C-D) indicates the elastic response of the specimen. The last nonlinear region (D-E) represents the loading phase where the plastic deformation ahead of the crack tip dominates. Likewise, the first linear segment (E-F) in the unloading phase exhibits the elastic response of the fully-open crack. The other sections in the unloading half cycle can similarly be explained.

An alternative method to measure crack closure is to use the direct-current-potential-drop (DCPD) technique, as shown in Figure 2.3. When a constant current is passed through the specimen, the crack-mouth potential is measured. This technique is often used to measure the crack length, especially in corrosion environments or at high temperatures. As the crack propagates, the resistivity of the material is increased, and,

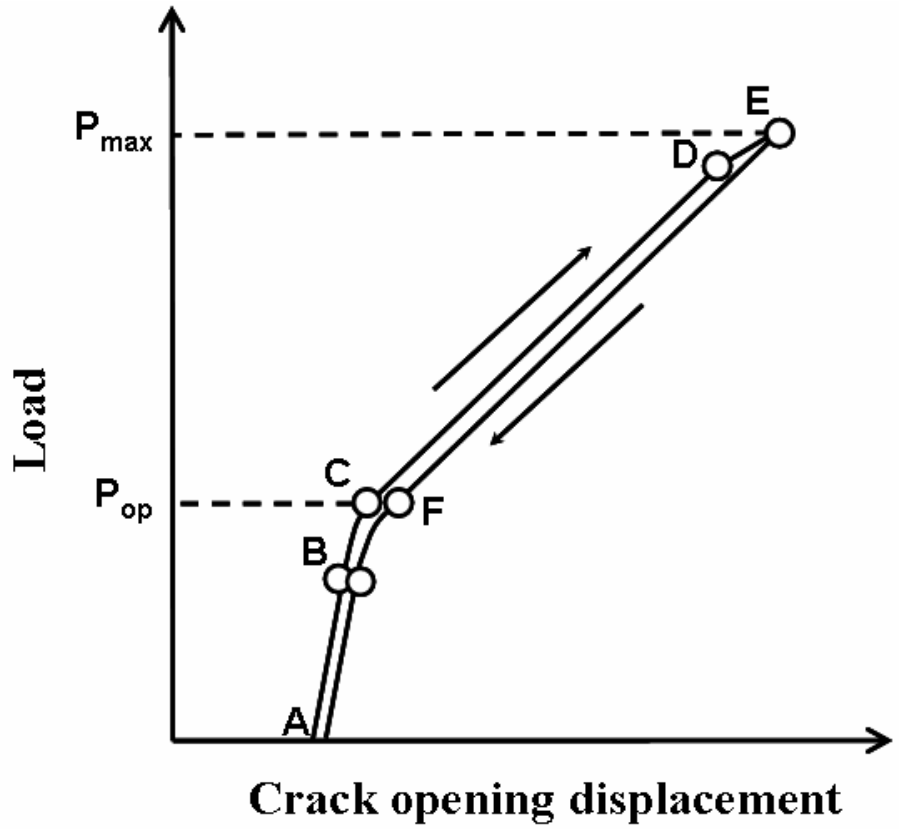

Figure 2.2: Schematic of load-COD curves. (Brahma et al., 1989)

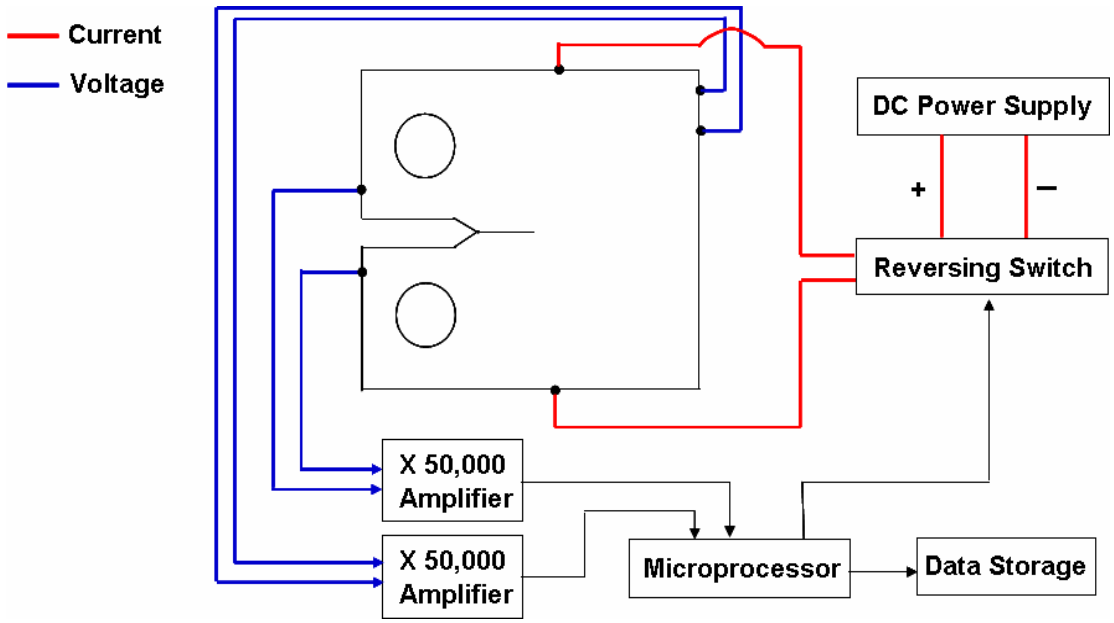

Figure 2.3: A schematic of direct-current-potential-drop technique.

thus, the change of the crack-mouth potential occurs. By detecting the change of the potential drop, the corresponding crack length is calculated. If the crack closes and produces an electric contact between the fracture surfaces, the crack-opening point should be determined from the curve of the load versus potential. Recently, Andersson et al. (2006) examined the possibility to use DCPD for crack-closure measurements by comparing the closure results from in-situ scanning-electron microscope (SEM). Figure 2.4 shows the loading phase of two experimentally obtained potential curves. Figure 2.5 presents a sequence of SEM images at a gradually increasing load. In Fig. 2.4, the point of crack opening as determined through the SEM-observations is marked on the PD-curves. They found that crack-closure measurements made by the potential drop have been shown to produce results similar to closure measurements determined from in-situ SEM observations, and concluded that the crack-opening point is reliable if crack closure is detected by potential measurements.

The effects of a single tensile overload have been the subject of much attention, because this type of loading can lead to a significant increase of the fatigue lifetime. Figure 2.6 shows a schematic of the overload effects on fatigue-crack growth. Some general observations can be summarized (Sadananda et al., 1999): (1) The retardation is generally measured in terms of delayed cycles, N_d, before the original steady-state conditions re-established [Fig. 2.6(b)]; (2) The retardation effect depends on the overload ratio (OLR), the background ΔK, where a single tensile overload is applied, and the background R ratio; (3) Overloads can give rise to a very short initial acceleration before significant deceleration occurs, Fig. 2.6(c). This initial acceleration

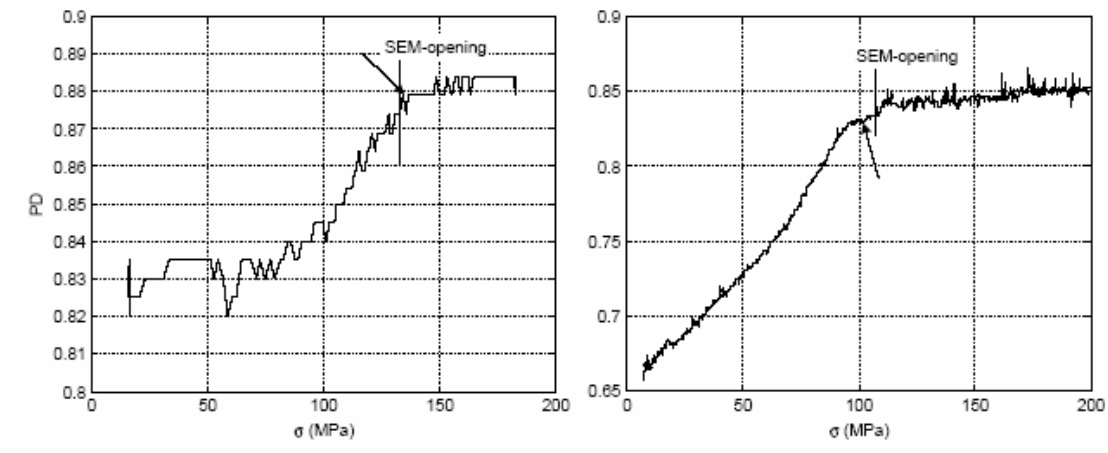

(a) (b)

Figure 2.4: Experimentally obtained PD-signals as functions of applied load. (a) Ti–6Al–4V and (b) steel. The arrows indicate the point of crack opening as defined from the PD-curves. (Andersson et al., 2006)

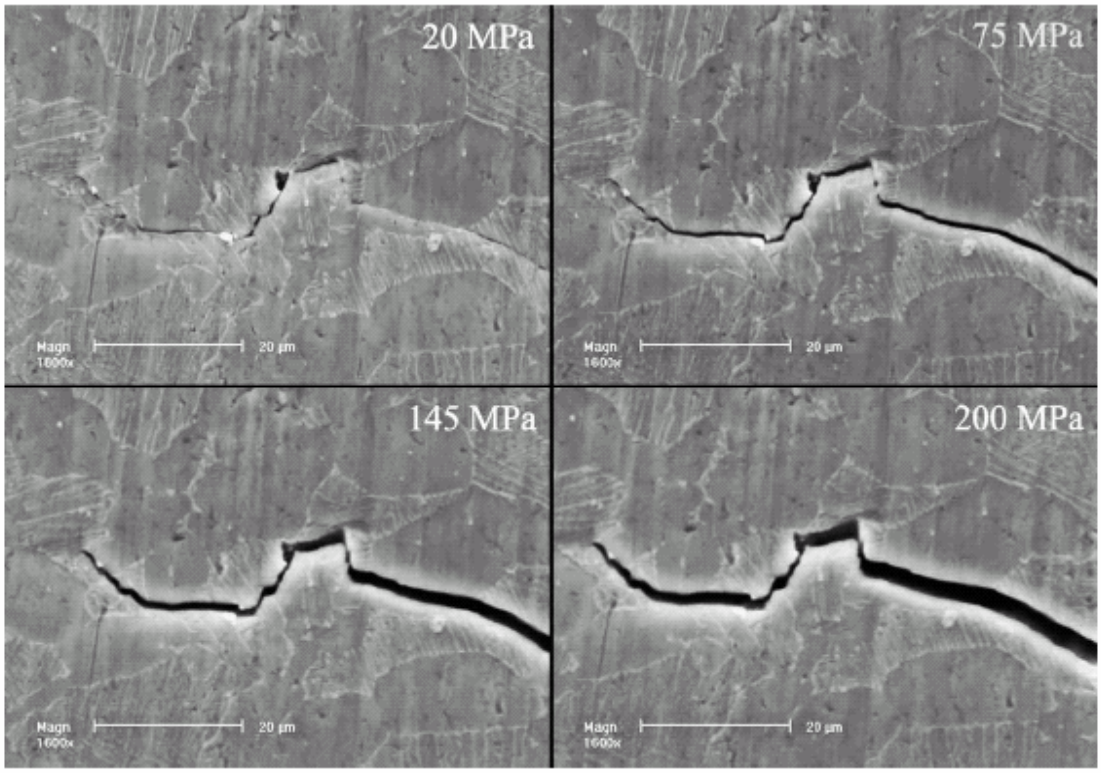

Figure 2.5: SEM image sequence showing the crack-opening event. (Andersson et al., 2006)

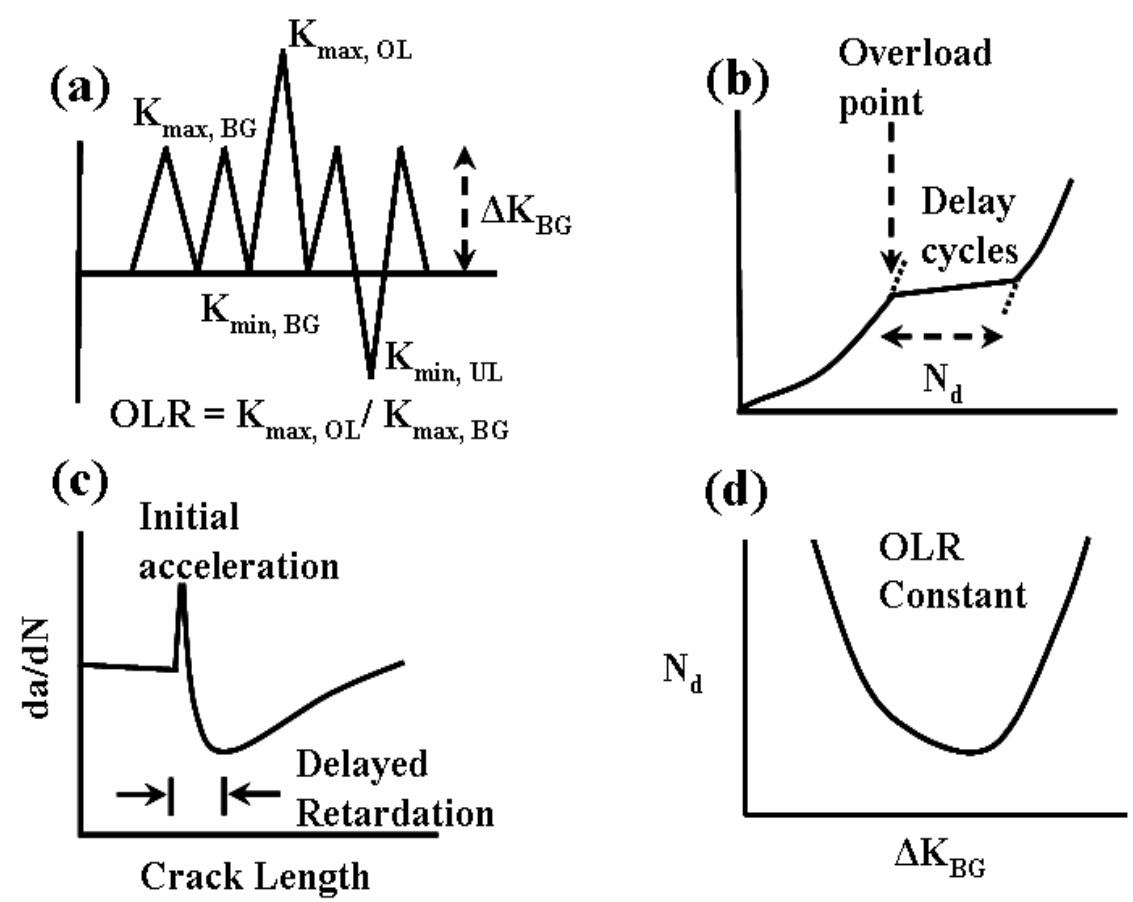

Figure 2.6: Schematic illustration of the overload effects on fatigue-crack growth. (Sadananda et al., 1999)

is observed at only high OLR and depends on the materials flow behavior. This can be seen in a constant ΔK test, Fig. 2.6(c); (4) The maximum deceleration of growth rates occurs a short distance away from the point of overload, and this effect is termed as the delayed retardation, Fig. 2.6(c). This delayed retardation depends again on the OLR and the background ΔK and R; (5) For the same OLR, N_d reaches a minimum as a function of ΔK, Fig. 2.6(d).(6) Retardation persists until the crack has propagated out of the perturbed plastic zone, a distance related to both the background plastic zone and the spectrum of the overload. Therefore, N_d depends on both the background plastic zone and the overload plastic-zone sizes; (7) Retardation effect depends on the specimen thickness since plastic zone sizes, PZS, under plane stress and plane strain differ. Retardation effects generally are larger under plane-stress conditions; (8) All factors that influence the plasticity at the crack tip will have direct or indirect influence on overload effects. These include the specimen geometry, temperature, environment, and material properties. The extent of systematic work in this area is limited.

Various possible mechanisms have been proposed to account for the overload-induced transient crack-growth phenomena, which include the crack-tip blunting (Christensen, 1959; Bathias & Vancon, 1978), compressive residual stress ahead of the crack tip (Schijve & Broek, 1962; Sadananda et al., 2001), crack branching (Suresh, 1983), plasticity-induced crack closure (Elber, 1971; Trebules et al., 1973; Reynolds, 1992), and roughness-induced crack closure (Suresh, 1983). It has been argued that the crack-tip blunting by the overloading can persist even during post-overload crack growth, and lead to crack-propagation retardation (Christensen, 1959). They suggested

that the blunted crack tip behaves like a notch with a less severe stress concentration than the originally sharp crack tip. Although crack-tip blunting does influence the post-overload crack-growth rate, it cannot account for the existence of delayed retardation and cannot quantitatively rationalize the experimentally-observed reductions in post-overload crack growth (Suresh, 1998).

Several investigators have attributed the crack retardation to residual stresses ahead of the crack tip (Schijve, 1962; Donald & Anderson, 1961). Figure 2.7 shows the development of a reversed plastic zone ahead of a crack tip upon an unloading process. A monotonic plastic zone is created by the application of a stress-intensity factor of magnitude K_1. Since the elastic-stress distribution associated with K_1 was truncated at σ_{ys} by local yielding, the subtraction of an elastic-stress distribution in going from K_1 to K_2 will cause the final crack-tip stress filed to drop sharply near the crack tip and even go into compression. At K_2, a smaller plastic zone, called a reversed plastic zone, is formed in which the material undergoes compressive yielding. When a tensile overload is applied, the size of the zone of residual compression is increased. It has been suggested that these residual stresses can retard the post-overload crack growth (Willenborg et al., 1971; Wheeler, 1972). It was found that the largest residual compressive stresses exist in the immediate vicinity of the crack tip. However, instantaneous retardation or crack arrest, rather than the delayed retardation, is predicted, which is contrary to experimental observations. Moreover, Suresh (1983) reported that retardation can persist even when the post-overload crack has traversed through the predicted zone of residual compressive stresses. Crack-tip branching,

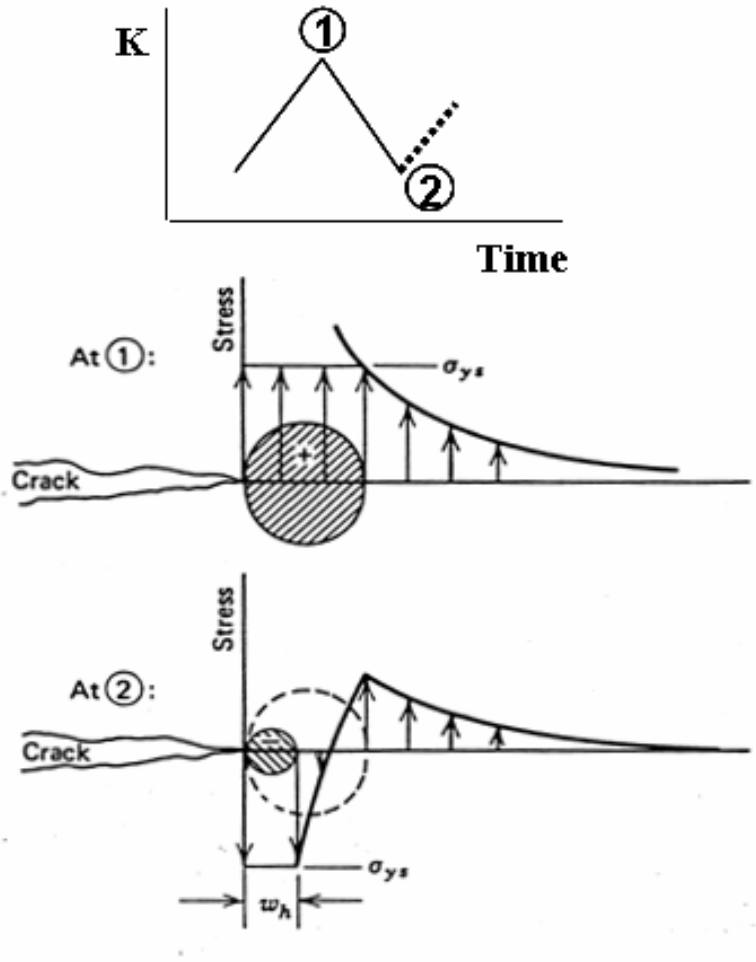

Figure 2.7: Monotonic and reversed plastic zone development at the tip of an advancing fatigue crack. (Hertzberg, 1996)

deflection, and secondary cracking affect the crack-tip-driving force (Suresh, 1983) because Mode II and Mode III components are superimposed on Mode I. The mechanisms (Bucci et al., 1980) are important for materials with significant planarity of slip and these mechanisms can be accentuated by certain environments or microstructures. The geometrical effects related to the bifurcation of the fatigue-crack tip by tensile overloads can contribute markedly to retardation effects. However, these mechanisms are not sufficiently general and cannot account for the generic behavior observed under overloads. Furthermore, it should be noted that if crack deflection occurs preferentially along a path of the low fracture resistance in some materials such as composites, it is likely to accelerate rather than retard post-overload growth rates.

Plasticity-induced crack closure and roughness-induced crack closure shift the attention to factors behind the crack tip. The plasticity-induced crack closure is based on the contact between fracture surfaces due to permanent residual tensile displacements formed by the plastic deformation at the crack tip. Elber (1971) suggested that this mechanism also can explain the retardation phenomena due to overloads by increasing the level of crack closure in the post-overload regime. Although a lot of experimental evidences support the plasticity-induced crack-closure mechanism, many observations are also inconsistent with this mechanism (Knott & Pickiard, 1977; Bucci et al., 1980; Suresh, 1983).

Roughness does not arise from the overload plasticity, but from the slip planarity and crack-path tortuosity. Hence, roughness is expected to play a role in planar slip materials. Since overload effects are common across the board, it is unlikely

that the roughness induced closure is the general cause for the overload-retardation effects (Sadananda et al., 1999). Louat et al. (1993) indicates that while the plasticity-induced closure is unlikely, the roughness-induced closure is possible, but that contribution is also very small.

Among several possible retardation mechanisms, the plasticity-induced crack closure has received considerable support in the fatigue community. However, other investigators have argued that plasticity always opens the crack rather than closing the crack (Louat et al., 1993; Sadananda & Vasudevan, 1998). Sadananda et al. (1999) reported that the residual stress ahead of the crack tip is a major factor for the retardation, rather than the crack closure behind the crack tip, and suggested a new "unified approach" in which both ΔK ($K_{max} - K_{min}$, the stress-intensity-factor range) and K_{max} are the fatigue-crack-tip-driving force. Recently, there exist many investigations to deny the significance of crack closure, following the unified approach as a fatigue-crack-tip-driving force (Vasudevan et al., 1992; Louat et al., 1993; Vasudevan et al., 1994; Sadananda et al., 1999; Zhang et al., 2005; Croft et al., 2007; Vallellano et al., 2009).

A variety of nondestructive-diffraction techniques, e.g., the X-ray diffraction and tomography (Ramos et al., 2003; Steuwer et al., 2006; Withers et al., 2006; Croft et al., 2007), and neutron diffraction (Sun et al., 2005; Lee et al., 2008, Lee et al., 2009) have been utilized to study the overload effects on fatigue-crack growth. Ramos et al. (2003, see Figure 2.8) investigated the residual-stress fields in the vicinity of the crack

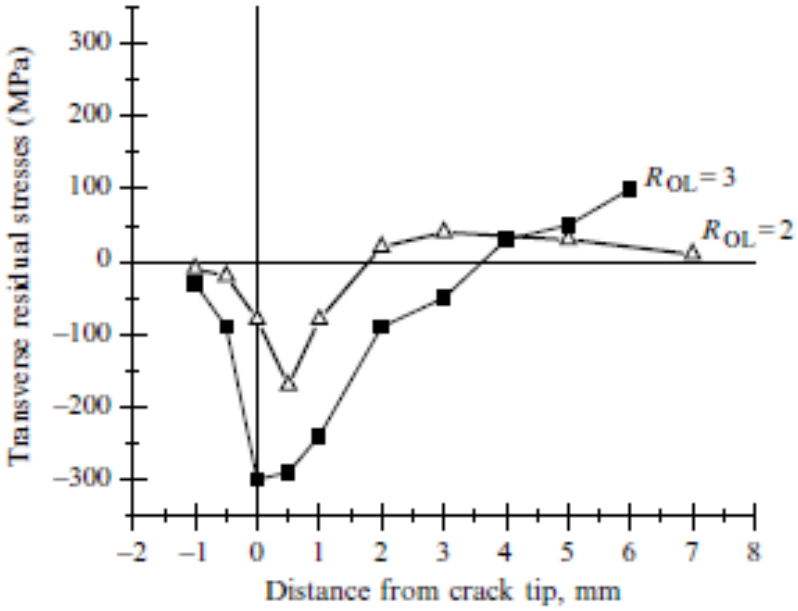

Figure 2.8: Residual-stress distribution on the specimen surface after single overload cycles. (Ramos et al., 2003)

tip on the overloaded samples with the overload ratios of 2 and 3 using a laboratory X-ray diffraction technique. They measured the transverse residual stresses as a function of the distance from the crack tip by providing the stress information on the sample surface. They showed that an increase in the overload ratio from 2 to 3 causes the compressive residual stresses to increase and to extend over a larger distance ahead of the crack tip. As a result, an overload ratio of 3 gives rise to a greater fatigue-life extension than that observed with a ratio of 2. They pointed out that the explanation of this behavior is related to the compressive-residual stress distribution ahead of the crack tip, which, in turn, depends on the size of the overload monotonic plastic zone.

Sun et al. (2005) investigated the elastic-lattice strain evolution during tensile loading and unloading cycles using neutron diffraction. After a tensile overload, they observed that a large compressive strain is generated near the crack tip. Steuwer et al. (2006) examined the local geometry of fatigue-crack growth and measured associated crack-tip strains/stresses, in particular with respect to crack closure using high-energy synchrotron X-ray tomography and diffraction. They found a large compressive strain just behind the crack-tip position at overload. Withers et al. (2006) employed high spatial resolution X-ray microtomography to map the variation of crack-opening displacement (COD) across matrix cracks in unidirectional Ti-6Al-4V/SCS-6 SiC fiber composites. They observed the tomography sequence by applying the overload of 3 K_{max}, as shown in Figure 2.9. They found that an overload of 3 K_{max} introduces the considerable local plasticity, interface sliding, residual COD, and crack-tip blunting.

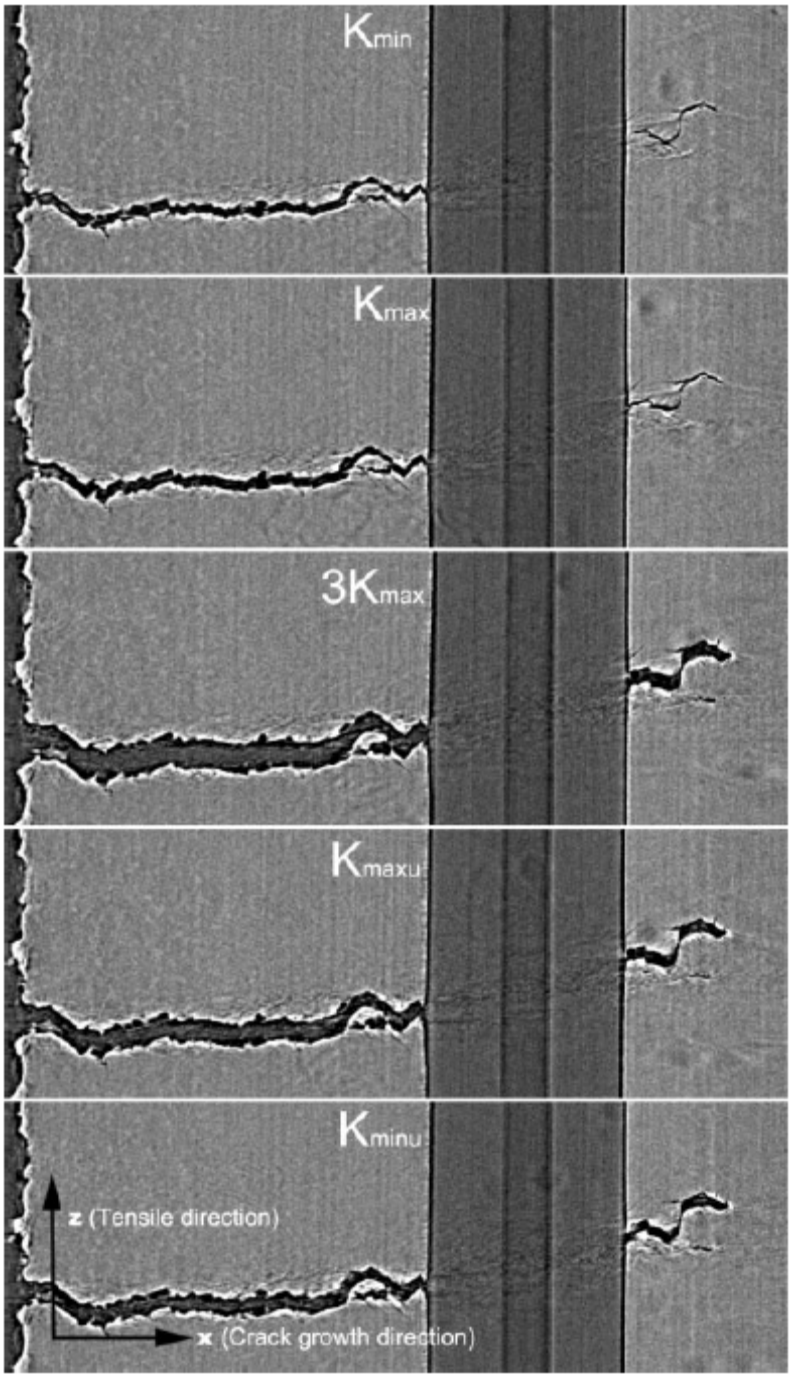

Figure 2.9: Tomographic sections through 3 K_{max} loading cycle. (Withers et al., 2006)

More detail work on the overload effects is reported by Croft et al. (2007). They prepared four compact-tension specimens, representing various different fatigue stages (e.g., just before the overload, right after the overload, maximum retardation point, and 50% retardation point). Then, they observed the elastic-strain evolutions in the vicinity of the crack tip with four different *in-situ* loading levels using synchrotron X-ray diffraction. They pay attention to obtain the strain change ($\Delta\varepsilon_{yy}$) and maximum strain (ε_{yy}) to correlate them to the driving force of crack tip using a unified approach (the combination form of ΔK & K_{max}). They assumed that the behaviors of strains $\Delta\varepsilon_{yy}$ and ε_{yy} can be used as indicators of the behaviors of stresses $\Delta\sigma_{yy}$ and σ_{yy} and of the crack-tip stress intensities ΔK and K_{max}. Their most interesting observation is the nonlinear load response of strains at different locations from the crack tip at the maximum retardation fatigue stage, as shown in Figure 2.10. They observed that the ratios of the low load responses (see dashed lines in the figure) are 1:2:6.5 at the 1 mm, tip, and OL positions, respectively. They also found that the OL-region dominates the response at low loads, whereas the crack-tip region dominates at high loads. These results indicate that a nonlinear load-dependent transfer of stress concentration between the OL and crack-tip regions is associated with the post-overloading behavior. More recently, Lee et al. (2008, 2009) showed how the internal strains around the crack tip are evolved under the application of various variable-amplitude loadings (e.g., overload, underload, and their mixed loads) and that large compressive residual strains and high dislocation densities are measured near the crack tip immediately after the overload using neutron diffraction.

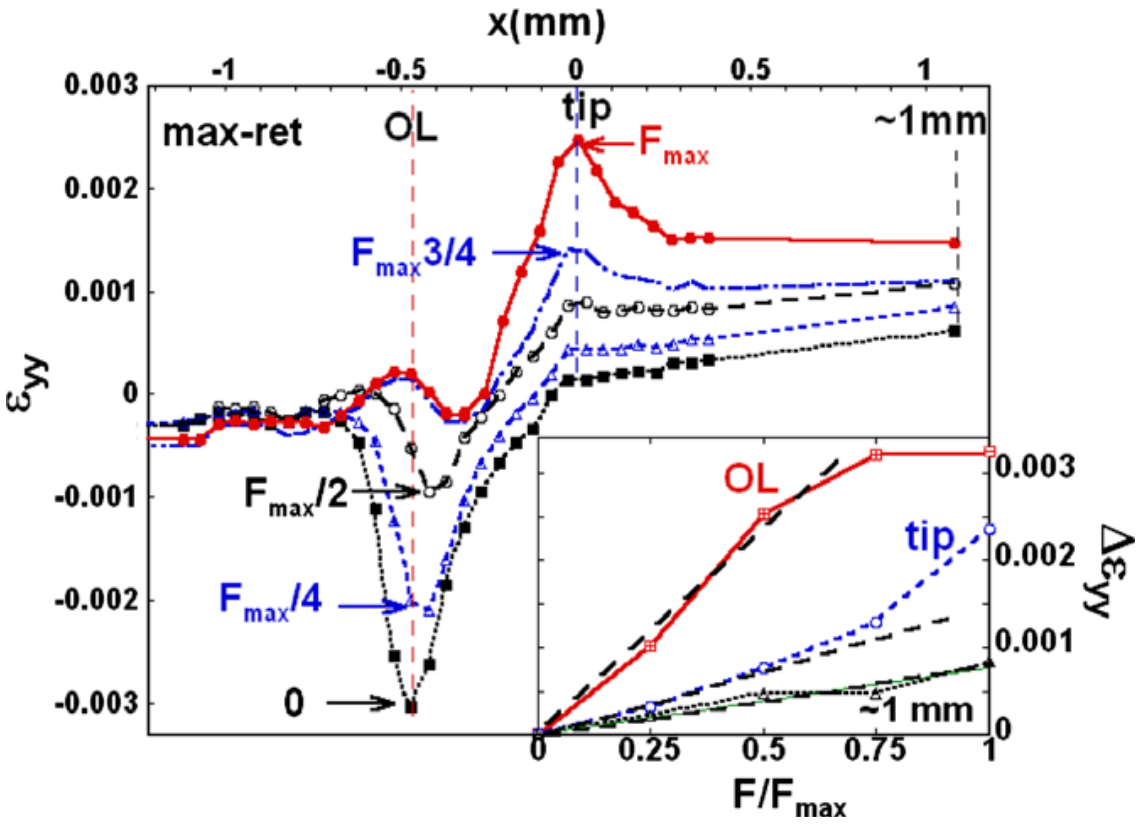

Figure 2.10: A series of strain profiles (measured at somewhat lower spatial resolution) at five load levels between F = 0 and F = F_{max}. Dashed lines indicate the OL and tip positions as well as a position of about 1 mm beyond the tip. Inset: the strain range, relative to the zero load strain versus load for these three positions. (Croft et al. 2007)

In summary, neutron and synchrotron X-ray diffraction techniques are a useful tool for the direct determination of the strains and stresses near the crack tip. These techniques enable the residual strain/stress mapping in the bulk sample as a function of the distance from the crack tip and the ability to conduct *in-situ* measurements of internal strains under applied loads. The direct measurements of residual and internal strain variations near the crack tip under various loading conditions will be of importance to the further development of modeling work and to the advancement of a fundamental understanding of the crack-tip deformation and fracture behavior.

2.2 Scientific Issues

Based on the above discussion, the retardation mechanisms are still not fully understood. Some people believe that the plasticity-induced crack closure, based on the contact between the fracture surface behind the crack tip due to the crack-wake plasticity, is the main cause of the retardation phenomena, whereas others argue that the compressive-residual stresses in front of the crack tip are the most important factor for the retardation, and the crack closure behind the crack tip is negligible. The fatigue-crack-tip-driving forces between the ΔK_{eff} and unified approach are also in the debate.

The calculation of the ΔK_{eff} is intrinsically based on the crack-closure behavior behind the crack tip. Thus, the determination of an exact crack-opening load is essential to obtain the correct crack-tip-driving force in the ΔK_{eff} concept. On the other hand, the unified approach is based on the magnitude and sign of the internal stresses ahead of the

crack tip, and, thus, it is of great importance to measure the precise internal-stress values.

In summary, the direct measurements of the internal strains/stresses near the crack tip and the precise determination of the crack-opening/closure levels will be an important matter on solving the above arguments shown in the literature. In this aspect, it is expected that the neutron-diffraction and electric-potential techniques will be of great importance to investigate the accurate crack-growth retardation and/or acceleration mechanisms and validate the exact fatigue-crack-tip-driving force between the ΔK_{eff} and unified approach.

2.3 Objectives

The overall objective of this work is to obtain a comprehensive understanding of the fatigue-crack-growth behavior under variable-amplitude loading conditions (e.g., overload and/or underload), in particular with respect to a single tensile overload case, and to probe the crack-growth retardation/acceleration mechanism as well as the crack-tip-driving force. The neutron-diffraction technique will help us understand the crack-tip-deformation behavior by measuring not only bulk residual strain/stress fields around the crack tip, but also internal strains *in situ* under an applied load. The electric-potential and *in-situ* neutron-diffraction techniques will enable us to measure accurate crack-closure levels for establishing the crack-tip-driving force and to investigate the relationship between the crack-tip-driving force and crack-growth rate. Crack-opening

levels obtained from both techniques will be compared. Therefore, this research will address the following specific goals:

(1) Examining the crack-growth behavior under overload, underload, and their mixed loads;

(2) Characterizing the residual stresses/strains fields around the crack tip under the various loading conditions and examining their effects on the crack-growth behavior;

(3) Investigating the evolution of the plastic zone through an overload-induced retardation period and its influence on the development of residual-strain distribution around a crack tip;

(4) Studying the load response of internal strains as a function of the distance from the crack tip;

(5) Determining the crack-opening levels at the various crack-growth stages;

(6) Identifying the crack-tip-driving force and establishing the relationship between the crack-tip-driving force and crack-growth rate;

(7) Understanding the key processes of overload-induced transient crack-growth micromechanisms.

Chapter 3

In-Situ Neutron-Diffraction Study of Internal-Strain Evolution around a Crack Tip under Variable-Amplitude Fatigue-Loading Conditions

3.1 Introduction

Many structural engineering materials exposed to fatigue failures experience variable-amplitude loading rather than constant-amplitude loading. Sudden changes in the cyclic mechanical-loading patterns could result in a significant acceleration and/or retardation in the crack-growth rate. Thus, the precise understanding of load-interaction effects, i.e., overload/underload effects, is essential to develop lifetime-prediction capabilities and saftety models, and to improve the design for critical applications subjected to random loadings. Many investigations have been reported regarding the overload/underload effects and crack-closure mechanisms (Elber, 1971; Gan & Weertman, 1981; Shin & Hsu, 1993; Dabayeh & Topper, 1995; Borrego et al., 2003; Makabe et al., 2004; Bichler & Pippan, 2007). More sepcifically, the retardation/acceleration phenomena have been intensively studied in terms of overload/underload ratio, baseline ΔK, R ratio, and specimen thickness, suggesting several possible mechanisms. Furthermore, various techniques have been used to determine the accurate crack-opening load (stress) for establishing the crack-tip driving force to explain such changes in the crack-growth rate related to crack closure.

Although much attention has been drawn to account for these transient behaviors, the phenomena are still not fully understood.

Neutron diffraction provides a unique tool in the study of mechanical behavior. The deep-penetration and volume-averaging capabilities of the neutron-diffraction technique enable the spatially-resolved mapping of internal strain/stress distribution in the bulk *in situ* under applied loads. Recently, nondestructive-diffraction techniques, e.g., high-energy synchrotron X-ray diffraction and neutron diffraction, have been employed to examine the residual-strain field, internal-strain evolution, texture, plastic-zone size, and dislocation-density distribution around the fatigue-crack tip (Sun et al., 2005; Steuwer et al., 2006; Croft et al., 2007; Daymond et al., 2007; Lee et al., 2008). The direct measurements of residual and internal strain variations near the crack tip under various loading conditions will be of importance to further development of modeling work and to the advancement of a fundamental understanding of the crack-growth behavior and crack-closure mechanism.

In this study, the lattice strain evolutions were examined during tensile overloading, compressive underloading, and their combinations using neutron diffraction. The results provide the relationship between strain distribution and crack-growth behavior under variable-amplitude fatigue-loading conditions.

3.2 Experimental Details

The fatigue-crack-growth experiments were performed on a compact-tension (CT) specimen of HASTELLOY C-2000 (56Ni-23Cr-16Mo, in weight percent) alloy

(Haynes). The specimen, prepared according to the American Society for Testing and Materials (ASTM) Standards E647-99, has a notch length of 10.16 mm, a width of 50.8 mm, and a thickness of 6.35 mm. The crack-growth experiments were conducted, employing a computer-controlled Material Test System (MTS) servohydraulic machine. Prior to the crack-growth tests, the CT specimens were precracked to a crack length of 1.27 mm, and then the crack-growth experiments were performed under a constant-load-range-control mode with a frequency of 10 Hz and a load ratio, R, of 0.01 [$R = P_{min}/P_{max}$, P_{min} and P_{max} are the applied minimum (89 N) and maximum (8,880 N) loads, respectively]. The crack length was measured by crack-opening-displacement (COD) gauge using the compliance method. The location of the crack tip was also confirmed using scanning electron microscope (SEM) and the difference of crack length between the compliance method and SEM was about 0.2 mm. For the setup of neutron strain mapping, the crack-tip location indentified by SEM was marked on the surface of the sample with a marker, which was tracked using a set of theodolites. The stress-intensity factor, K, was obtained using the following equation (Liaw et al., 1982):

$$K = \frac{P(2+\alpha)}{B\sqrt{W}(1-\alpha)^{3/2}}(0.886 + 4.64\alpha - 13.32\alpha^2 + 14.72\alpha^3 - 5.6\alpha^4) \qquad (3.1)$$

where P = applied load, B = thickness, $\alpha = a/W$, a = crack length, and W = width. When the crack length reached 16 mm, one of the following loading scenarios was applied to study the effects of overloading, underloading, and their combinations on fatigue crack growth: (*Case 1*) continuing with the fatigue loading under the same baseline condition,

(*Case 2*) a single tensile overloading (13,320 N), (*Case 3*) a single compressive underloading (-13,320 N), (*Case 4*) overloading-underloading, or (*Case 5*) underloading-overloading. After applying various loading conditions, the constant-amplitude fatigue experiment was resumed for all cases to monitor the crack-growth behavior.

In-situ neutron-diffraction experiments under loading were carried out using the time-of-flight (TOF) neutron diffractometer ENGIN-X at the ISIS facility, STFC Rutherford Appleton Laboratory, UK (Daymond & Priesmeyer, 2002). The specimen was aligned in a load frame with the loading axis oriented 45° relative to the incident neutron beam. The entire diffraction pattern was recorded in two stationary detector banks centred on diffraction angles of $2\theta = \pm 90°$. Thus, the diffraction vectors were parallel to the in-plane (IP, parallel to the loading direction) and through-thickness (TT) directions of the specimen. The incident beam was defined by 2-mm horizontal and 1-mm vertical slits, and the diffracted beams were collimated using 2-mm radial collimators, resulting in a 4-mm^3 gauge volume. The lattice parameters were obtained from Rietveld refinement (Rietveld, 1969) using the General Structure Analysis System (GSAS) (Larson & Von Dreele, 2004). The lattice strains were calculated from

$$\varepsilon = (a\text{-}a_0)/a_0 \tag{3.2}$$

where a is the lattice parameter under applied load and a_0 is the stress-free reference lattice parameter measured away from the crack tip at a corner of each CT specimen. Only in-plane lattice strain (parallel to the loading direction) will be discussed in this

study. The two fatigued specimens with the same crack length of 16 mm were used for *in-situ* loading neutron-diffraction measurements. The strain mappings were carried out at five different loading conditions for the first specimen and at four different loading cases for the second sample, as shown in Figure 3.1. At each load, a total of 19 (the first specimen) and 16 (the second specimen) points were measured as a function of the distance from the crack tip along the direction of crack growth. There were no complications with holding at applied loads during the neutron-diffraction data acquisition since creep is negligible for this material under the current condition.

3.3 Results and Discussion

The crack-growth rates (da/dN) as a function of ΔK for HASTELLOY C-2000 are shown in Figure 3.2. In Fig. 3.2(a), during a constant-amplitude fatigue-crack growth (*Case 1*), the crack-propagation rate increases linearly with increasing ΔK. After a single tensile overload (*Case 2*) was applied, there was an instantaneous acceleration of the crack-growth rate followed by a large retardation period, resulting in a temporary decrease in the crack-propagation rates. On the other hand, after a single compressive underload (*Case 3*) was introduced, a brief acceleration of the crack-growth rate was observed. However, the subsequent crack-propagation rate was very comparable to that of *Case 1*. In Fig. 3.2(b), when a compressive underload was imposed immediately after a tensile overload, a retardation period was still found but had a significantly reduced extent (*Case 4*). Finally, when a tensile overload was imposed immediately after a

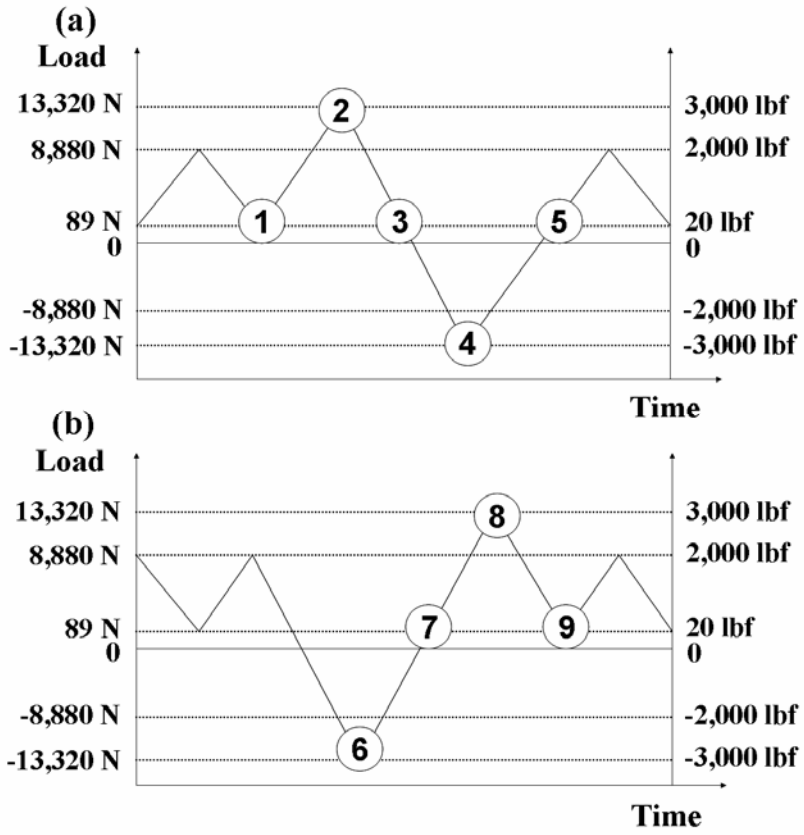

Figure 3.1: Neutron-diffraction strain mapping was performed at each load point (LP) from LP1 to LP9. (a) LP1: unloading (P_{min}) during fatigue, LP2: at tensile overloading, LP3: unloading from tensile overloading, LP4: at compressive underloading after tensile overloading, and LP5: unloading from tensile overloading and then compressive underloading; (b) LP6: at compressive underloading, LP7: unloading from compressive underloading, LP8: at tensile overloading after compressive underloading, and LP9: unloading from compressive underloading and then tensile overloading.

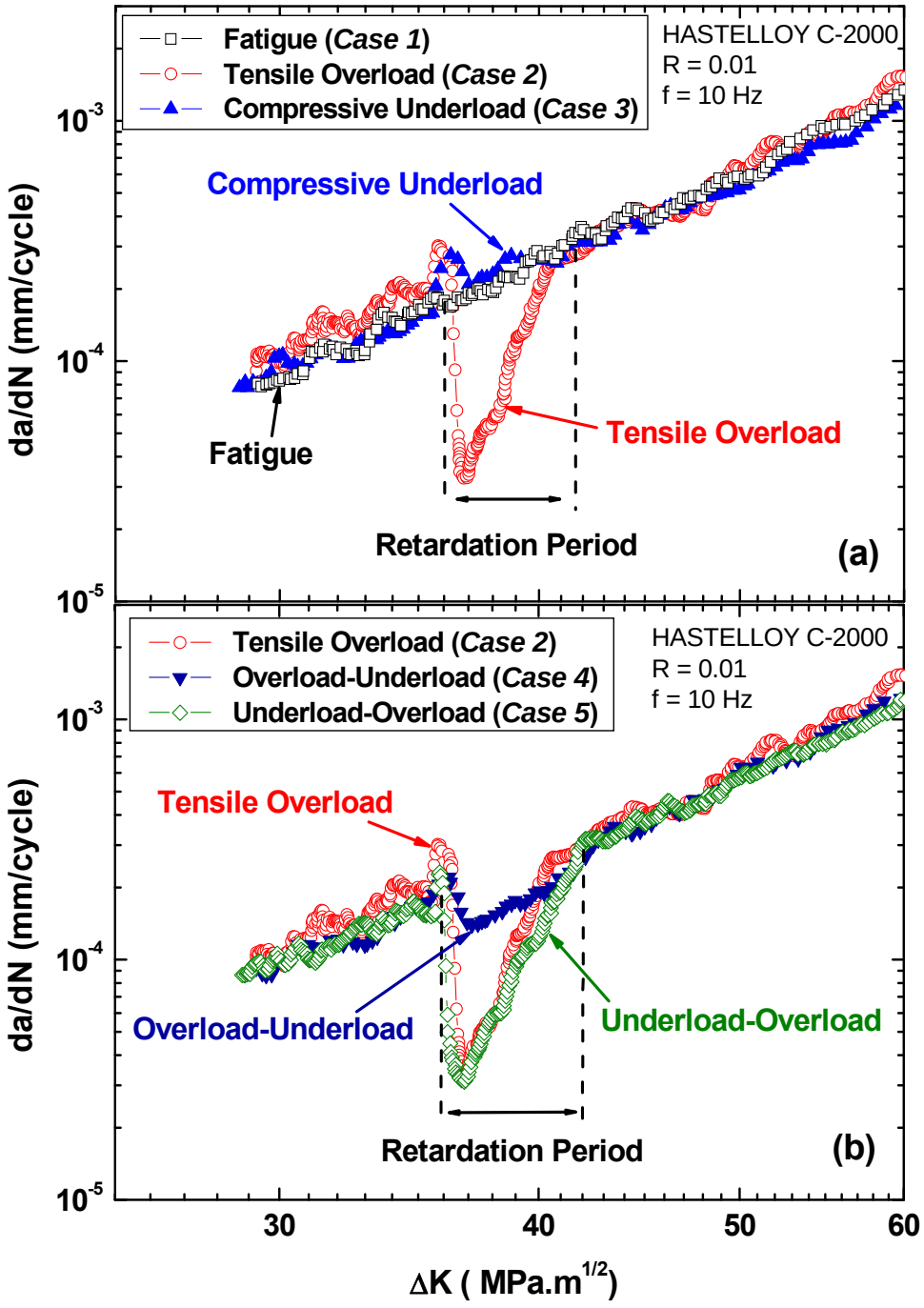

Figure 3.2: The changes in the crack-growth rate (d*a*/d*N*) as a function of the stress-intensity-factor range (ΔK) for five different loading cases.

compressive underload (*Case 5*), the crack-growth rates were similar to those of a single tensile overload (*Case 2*).

Figure 3.3 shows the in-plane (IP) lattice-strain evolutions measured at various applied loads [load points (LP) 1, 2, 3, 4, and 5 shown in Fig. 3.1(a)] during tensile overloading and subsequent compressive underloading cycles. It should be noted that the "*residual*" strain profiles of as-fatigued (*Case 1*), tensile overloaded (*Case 2*), and overloaded-underloaded (*Case 4*) specimens correspond to load points (LP) 1, 3, and 5, respectively. At LP1 (89 N), the compressive strain field with the maximum of about –400 με (microstrain, 10^{-6}) was observed from behind the crack tip to 0.7 mm in front of the crack tip. The tensile strains were examined from 0.7 mm to 11 mm ahead of the crack tip with the maximum tensile strain of about 305 με at 3.5 mm. As the applied load increases from LP1 to LP2 (13,320N, an overload point), the strain profile, especially ahead of the crack tip, significantly increases. At 0.5 mm in front of the crack tip, the largest tensile strain of about 1,480 με was observed. Another maximum strain of 1,000 με was measured at about 4.5 mm from the crack tip. After a tensile overload (LP2), the load was decreased to LP3 (89 N). After a single tensile overload was imposed and then unloaded, the large compressive strains with a maximum of –640 με were observed within ± 3.5 mm near the crack tip due to the overload-induced large plastic deformation. As the distance from the crack tip increases, the strains changed from compressive to tensile, showing the maximum tensile strain at about 6 mm ahead of the crack tip. It is thought that a large compressive residual strain should reduce the crack-tip driving force for crack propagation, because a higher crack-opening load is

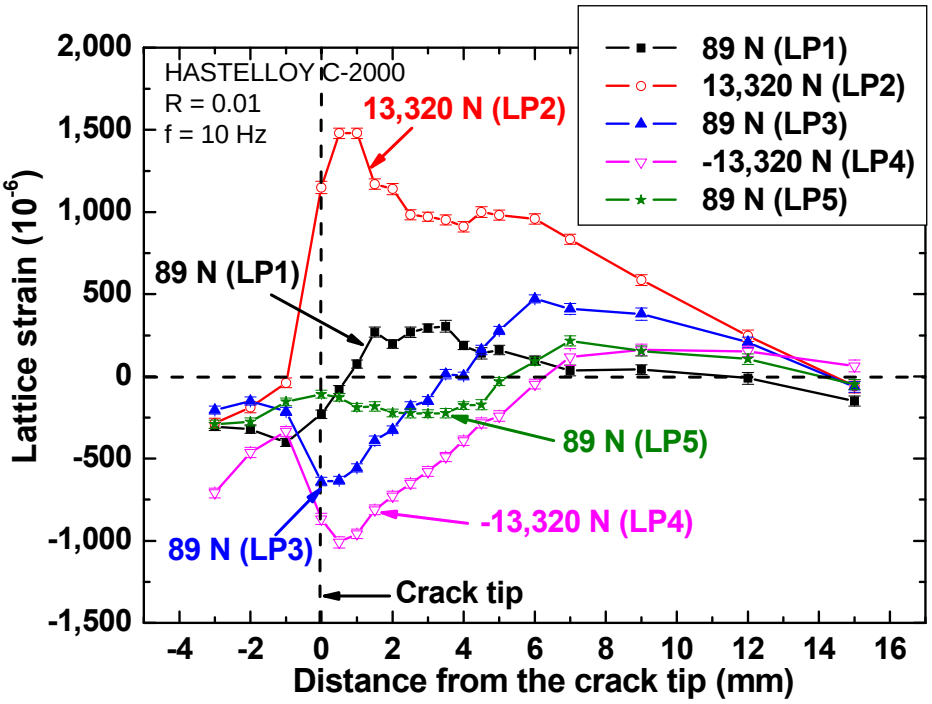

Figure 3.3: In-plane lattice-strain profiles around the crack tip at various load points shown in Fig. 3.1(a), overloading-underloading cycles.

required to overcome the compressive residual strains around the crack tip. Thus, a tensile overload could result in a large retardation period, as presented in Fig. 3.2.

The compressive underload of –13,320 N (LP4) was applied immediately after the tensile overloading. At LP4, the lattice strains were more compressive compared to the overloaded condition (LP3) due to the compressive underloading. The load was then released from LP4 to LP5 (89 N). After the compressive underload was introduced and then unloaded immediately after a tensile overloading, the large compressive residual strains around the crack tip disappeared and small compressive residual strains of about –200 με were found within 5 mm ahead of the crack tip owing to the reversed plastic deformation. It is believed that such a reduced compressive residual strain is responsible for the reduced retardation period, as compared to the tensile overloading (*Case 2*) shown in Fig. 3.2(b). Figure 3.4 shows the in-plane (IP) lattice-strain distributions measured at various applied loads [LP 6, 7, 8, and 9 shown in Fig. 3.1(b)] during compressive underloading and tensile overloading cycles. Note that the "*residual*" strain profiles of compressive underloaded (*Case 3*) and underloaded-overloaded (*Case 5*) specimens correspond to load points (LP) 7 and 9, respectively. When the compressive load of –13,320 N (LP6) was applied during fatigue, the largest compressive lattice strain of –1,090 με was observed at 3 mm behind the crack tip and compressive strains were found up to 3 mm ahead of the crack tip. At LP7 (89 N), the small compressive residual strains (with a maximum of about –340 με) were measured up to 1.5 mm ahead of the crack tip and tensile strains appeared with increasing distance

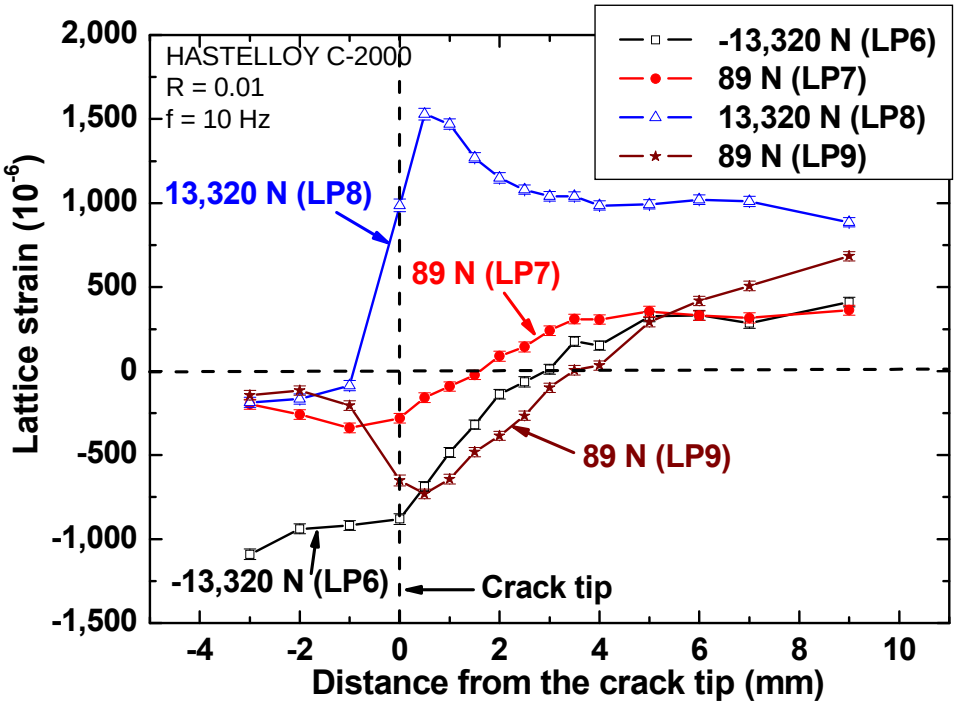

Figure 3.4: In-plane lattice-strain profiles around the crack tip at various load points shown in Fig. 3.1(b), underloading-overloading cycles.

from the crack tip. It is noted that the residual strain distributions at LP7 were very comparable to those at LP1 but had smaller compressive strains behind the crack tip. This reduced compressive strain will result in a decrease in the crack-opening load, and, thus, higher crack-tip driving force for crack growth. Therefore, immediately after a single compressive underloading, an instantaneous acceleration of crack growth was observed but the effect was not as significant as in the overload-underload case (*Case 4*), as shown in Fig. 3.2. As the applied load increases to LP8 (an overload point), it can be noted that strains behind the crack tip did not change much, while strains in front of the crack tip increased significantly with increasing applied load. Finally, the applied load was decreased from LP8 to LP9 (89 N). Note that LP9 provides the "*residual*" strain profiles for underloaded-overloaded sample (*Case 5*). Large compressive residual strains with a maximum of about –730 με were found within 3.5 mm in front of the crack tip. It was found that these lattice-strain profiles were very similar to those at LP3 (an unloading point after a single tensile overloading). As a result, the crack-growth behavior after underloaded-overloaded condition (*Case 5*) would be very similar to that after a single tensile overload (*Case 2*) due to the large compressive residual strains near the crack tip as presented in Fig. 3.2.

3.4 Summary

The internal-strain evolutions were investigated in five different loading conditions (i.e., fatigued, tensile overloaded, compressive underloaded, tensile overloaded-compressive underloaded, and compressive underloaded-tensile overloaded)

using *in-situ* neutron-diffraction strain scanning under an applied load. After a single tensile overload (*Case 2*) or underload-overload (*Case 5*) was introduced and then unloaded, large compressive strains were observed around a crack tip, resulting in the large crack-growth retardation. When a single compressive underload was applied and then unloaded immediately after the tensile overloading (*Case 4*), the large compressive strains with a maximum of –640 με disappeared and small compressive strains of about –200 με were found within 5 mm from the crack tip, supporting the reduced extent of the crack-growth retardation. On the other hand, after a single compressive underloading (*Case 3*), an instantaneous acceleration of the crack-growth rate was observed, but the effect was not as significant as in the overload-underload case (*Case 4*). The current results show that distinct residual-strain profiles around a crack tip are closely related to the different crack-growth behaviors under the various loading conditions.

Chapter 4

Neutron-Diffraction Measurements of Residual Stresses around a Crack Tip Developed under Variable-Amplitude Fatigue Loadings

4.1 Introduction

In the case of numerous fatigue-critical structure components, fatigue-crack propagation under service conditions generally involves random or variable-amplitude loadings rather than constant-amplitude loading (Ward-Close et al., 1989). Sudden variations, e.g., overload and/or underload, in the constant-amplitude cyclic-loading sequence could influence the distributions of stress states near a fatigue crack, and, ultimately, result in a significant crack-growth acceleration and/or retardation, making it difficult to predict the crack-growth behavior (Skorupa, 1998). Hence, the accurate understanding and control for the crack resistance of materials subjected to the load-interaction phenomena, i.e., overload and/or underload, are crucial to develop the damage-tolerance design and lifetime-prediction methodology.

Residual stresses are one of the contributory factors to failure in structural components. Withers (2007) demonstrated that when unexpected failure occurs it is often because residual stresses have combined critically with the applied stresses, or because they, together with the presence of unknown defects or poor microstructures, have dangerously lowered the applied stresses at which failure will occur. Residual

stresses also play a significant role on the fatigue-crack-growth behavior. It is generally known that compressive-residual stresses are found to decrease the crack-propagation rates, while tensile-residual stresses yield the opposite effect (Almer et al., 1998). In terms of the crack-growth retardation phenomena following a single tensile overload, many researchers reported that the enlarged compressive residual stresses after a tensile overload are one of the possible retardation mechanisms, slowing down the crack-growth rates in the retardation period (Carlson et al., 1991; Damri & Knott, 1993; Shin & Hsu, 1993; Wheatley et al., 1999). Makabe et al. (2004) demonstrated that the tensile-residual stresses developed by a compressive underload are an important consequence of the reversed plastic flow, leading to the reduction of crack-opening level and acceleration of crack-growth rate. Various models depending on the residual stresses have also been developed to predict the fatigue-crack-propagation behavior under constant-amplitude or variable-amplitude loadings (Su et al., 1986; Willenborg et al., 1971). However, Lam & Lian (1989) pointed out that the models predicting the residual-stress effect on fatigue- crack growth have not been completely quantified, due to a task of difficulty to measure the residual-stress distribution accurately. Thus, the accurate residual-stress measurements near the crack tip influenced by the prior plastic deformation will be of importance to the improvement of a fatigue-lifetime prediction model, as well as a better understanding of the crack-propagation behavior.

Neutron diffraction is a powerful technique in the direct measurement of internal strains/stresses in the bulk sample (Allen et al., 1992; Pang et al., 1998). Previously, the development of internal strains around a crack tip was clearly observed during tensile

overloading, compressive underloading, and their combinations using neutron diffraction (Lee et al., 2009). In this investigation, the direct measurements of residual-stress distribution were carried out as a function of the distance from the crack tip using neutron diffraction, immediately after applying a tensile overload, a compressive underload, and their mixed loads during fatigue-crack growth. The results provide the relationship between the residual-stress distribution and fatigue-crack-growth behavior following overload, underload, and their mixed loads.

4.2 Experimental Details

The fatigue-crack-growth experiments were conducted on a nickel-based Hastelloy C-2000 (Haynes) compact-tension specimen [Fig. 4.1(a)] prepared according to the American Society for Testing and Materials (ASTM) Standards E647-99 (ASTM, 2000). The crack length was measured by crack-opening-displacement gauge using the compliance method. During the constant-amplitude fatigue-crack growth [i.e., P_{max} = 8,880 N, P_{min} = 89 N, a load ratio, R (P_{min} / P_{max}) = 0.01, and frequency = 10 Hz], one of the following loading conditions was applied at ΔK = 35.89 MPa·m$^{1/2}$. *Case 1*: continuous fatigue loading under the same baseline condition; *Case 2*: a single tensile overload (13,320 N, 150% of P_{max}); *Case 3*: a single compressive underload (–13,320 N); *Case 4*: overload-underload; and *Case 5*: underload-overload. After various loading conditions were applied, the constant-amplitude fatigue-crack-growth test was resumed for all cases.

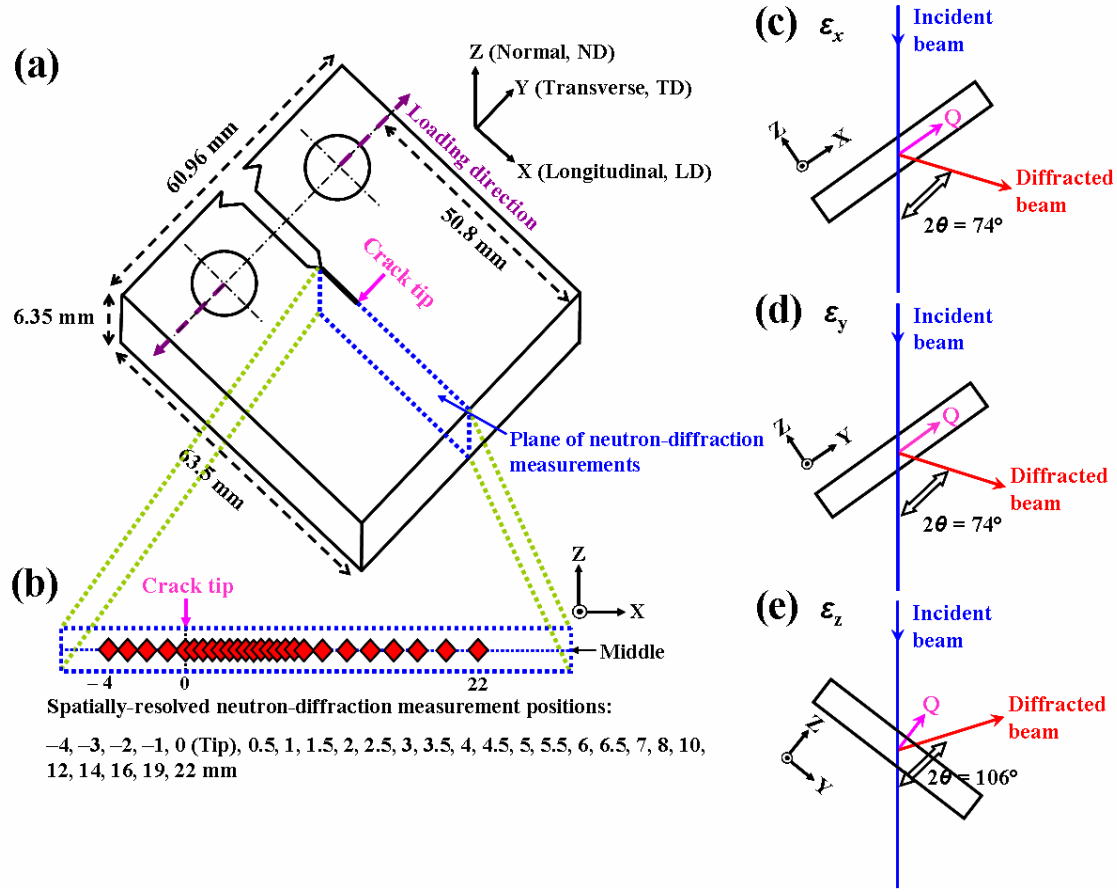

Figure 4.1: (a) The geometry of a Hastelloy C-2000 compact-tension specimen; (b) spatially resolved neutron-diffraction measurement positions along the direction of crack propagation (*x*); Schematic of diffraction geometry for the residual-stress mapping showing the scattering vector (Q) parallel to the coordinate (c) *x*: longitudinal strain (ε_x) component; (d) *y*: transverse strain (ε_y) component; and (e) *z*: normal strain (ε_z) component.

A neutron-diffraction residual-stress mapping was performed on L3 spectrometer at Chalk River Laboratories, Canada. The five compact-tension (CT) specimens processed by the different loading conditions [i.e., constant-amplitude fatigued (*Case 1*), tensile overloaded (*Case 2*), compressive underloaded (*Case 3*), tensile overloaded-compressive underloaded (*Case 4*), and compressive underloaded-tensile overloaded (*Case 5*)] were prepared to study the influence of residual stresses on the crack-growth rate, as shown in Fig. 4.2. Three principal residual-strain components [i.e., longitudinal (ε_x), transverse (ε_y), and normal (ε_z) strains, Fig. 4.1(a)] were measured as a function of the distance from the crack tip along the crack-growth direction [*x*-direction, Fig. 4.1(b)]. A total of 26 points were measured as a function of the distance from the crack tip. To provide the required spatial resolution, the scanning intervals of 1 mm from –4 to 0 mm (crack tip), 0.5 mm from 0 to 8 mm where sharp strain gradients are expected, 2 mm from 8 to 16 mm, and 3 mm from 16 to 22 mm were employed.

A schematic view of the diffraction geometry is shown in Figs. 4.1(c)-(e). For the longitudinal (ε_x) and transverse (ε_y) strain components [Figs. 4.1(c) and (d), respectively], the wavelengths of 1.308499Å and 1.308773Å, respectively, were selected from the Ge115 monochromator. The specimen was aligned 53° (clockwise) from the incident neutron beam and the (311) diffraction pattern was measured in a stationary detector centered on a diffraction angle of $2\theta = 74°$. The longitudinal (ε_x) strain component was measured using 1-mm wide and 2-mm tall (parallel to *y*) incident beam slits, and 1-mm wide diffracted beam slit. The transverse (ε_y) strain component

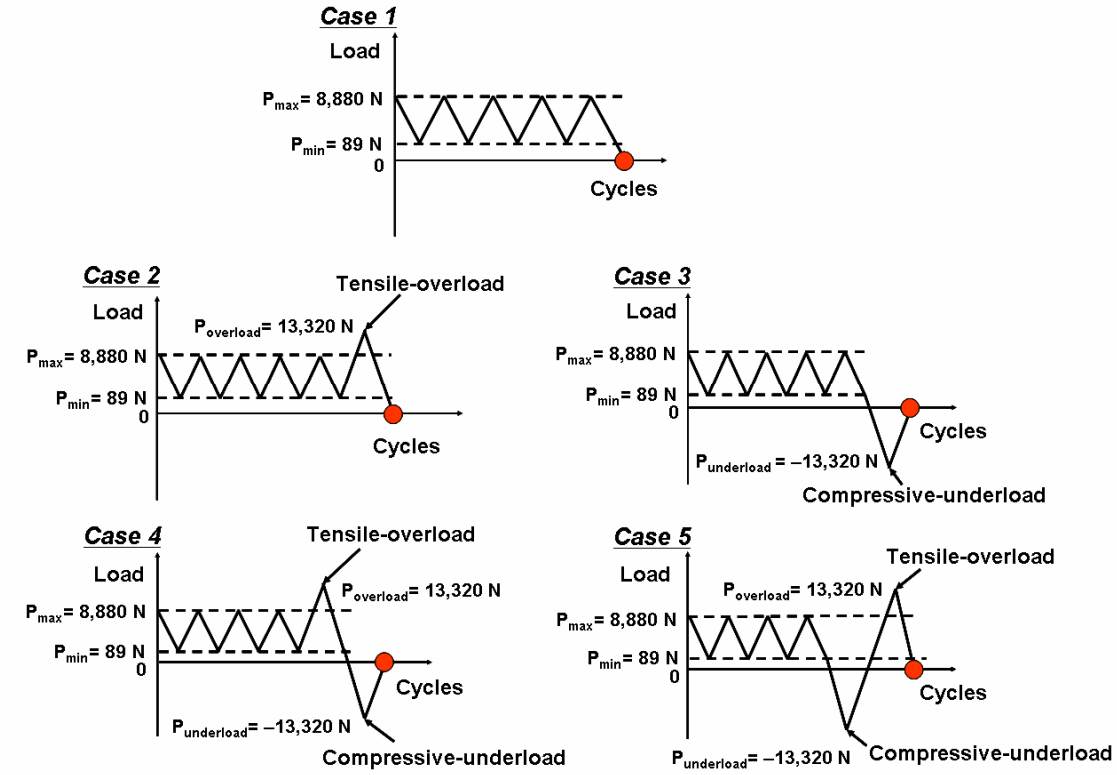

Figure 4.2: Neutron residual-stress mappings shown in Fig. 4.1 were performed on the five compact-tension specimens subjected to various variable-amplitude fatigue-loading conditions (i.e., *Case 1*: constant-amplitude fatigued, *Case 2*: tensile overloaded, *Case 3*: compressive underloaded, *Case 4*: tensile overloaded-compressive underloaded, and *Case 5*: compressive underloaded-tensile overloaded). Note that red marked circles indicate the neutron measurement points.

was measured using 2-mm wide and 1-mm tall (parallel to x) incident beam slits, and 2-mm wide diffracted beam slit. For the normal (ε_z) strain component [Fig. 4.1(e)], the wavelength of 1.738462Å was chosen from the Ge115 monochromator. The specimen was aligned 127° (clockwise) from the incident neutron beam and the (311) diffraction pattern was recorded in a stationary detector centered on a diffraction angle of 2θ = 106°. Thus, the diffraction vectors were parallel to the normal direction (parallel to z) of the specimen. The incident beam was defined by 2-mm wide and 1-mm tall (parallel to x) slits, and the diffracted beams were collimated by 2-mm wide slit.

The interplanar spacings (d-spacings) along the longitudinal, transverse, and normal directions were determined from the Gaussian fitting of the (311) diffraction peak, and the lattice strains were obtained from

$$\varepsilon = (d\text{-}d_0)/d_0 \tag{4.1}$$

where d_0 is the stress-free reference d-spacing, which was measured away from the crack tip. Three residual stress components, σ_i (i = x, y, and z, corresponding to longitudinal, transverse, and normal directions, respectively), are calculated from the three strain components using the following equation:

$$\sigma_i = \frac{E}{1+\nu}\left[\varepsilon_i + \frac{\nu}{1-2\nu}\left(\varepsilon_x + \varepsilon_y + \varepsilon_z\right)\right] \tag{4.2}$$

where E is the Young's modulus and ν is the Poisson's ratio.

4.3 Results and Discussion

Figure 4.3 presents the crack-growth rate (da/dN) vs. stress-intensity-factor range (ΔK) for five different loading cases. *Case 1* showed a linear increase of the crack-growth rate with increasing ΔK. After *Case 2* (a single tensile overload) was introduced, the crack-propagation rate was instantaneously accelerated, and then a large crack-growth retardation period was observed. *Case 4* (an overload-underload sequence) showed the significantly reduced crack-growth retardation, as compared to that of *Case 2*. On the other hand, after *Case 3* (a single compressive underload) was introduced, the crack-growth rate was initially accelerated, but the subsequent crack-propagation rate was similar to that of *Case 1*. When *Case 5* (an underload-overload sequence) was imposed, the crack-growth rates were similar to those of *Case 2*, indicating a large retardation period. To obtain a better understanding of the transient crack-growth behavior following the overload and/or underload, the residual-stress fields near a fatigue-crack tip were measured using neutron diffraction, immediately after applying the five different loading conditions, as shown in the marked point, Fig. 4.2.

Figure 4.4 shows the longitudinal (σ_x), transverse (σ_y), and normal (σ_z) residual-stress profiles in the vicinity of the crack tip. In the case of *Case 1* (constant-amplitude fatigued), the tensile longitudinal residual stresses were examined behind the crack tip and the stresses were varied from tensile to compressive at about 0.5 mm ahead of the crack tip [Fig. 4.4(a)]. The normal residual-stress fields also showed similar stress distributions around the crack tip, as exhibited in Fig. 4.4(e). The relatively large tensile

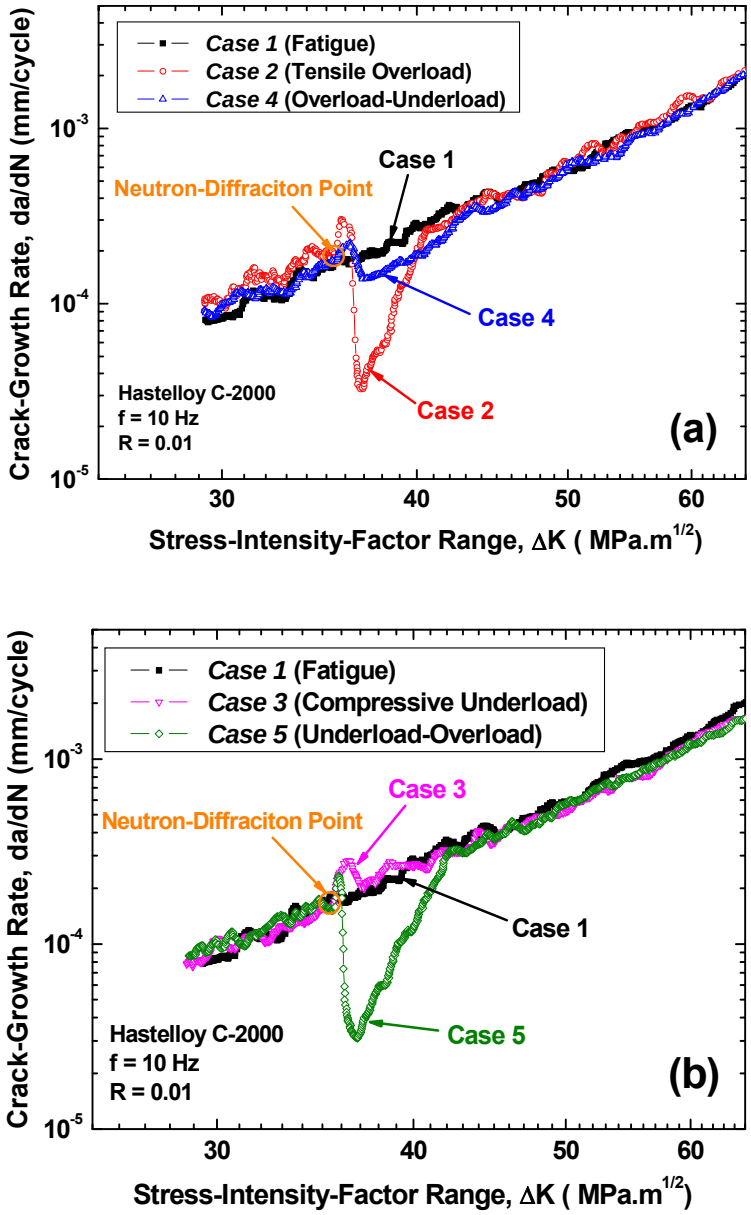

Figure 4.3: The crack-growth rate (d*a*/d*N*) vs. stress-intensity-factor range (ΔK) for the tests with different loading cases. (a) *Case 1, Case 2, and Case 4*, (b) *Case 1, Case 3,* and *Case 5*. Note that the neutron residual-stress measurements were carried out at the marked circle points, which corresponds to those indicated in Fig. 4.2.

Figure 4.4: Longitudinal residual-stress (σ_x) distributions as a function of the distance from the crack tip for the tests with (a) *Case 1, Case 2,* and *Case 4*, (b) *Case 1, Case 3,* and *Case 5*; transverse residual-stress (σ_y) distributions as a function of the distance from the crack tip for the tests with (c) *Case 1, Case 2,* and *Case 4*, (d) *Case 1, Case 3,* and *Case 5*; normal residual-stress (σ_z) distributions as a function of the distance from the crack tip for the tests with (e) *Case 1, Case 2,* and *Case 4*, (f) *Case 1, Case 3,* and *Case 5*.

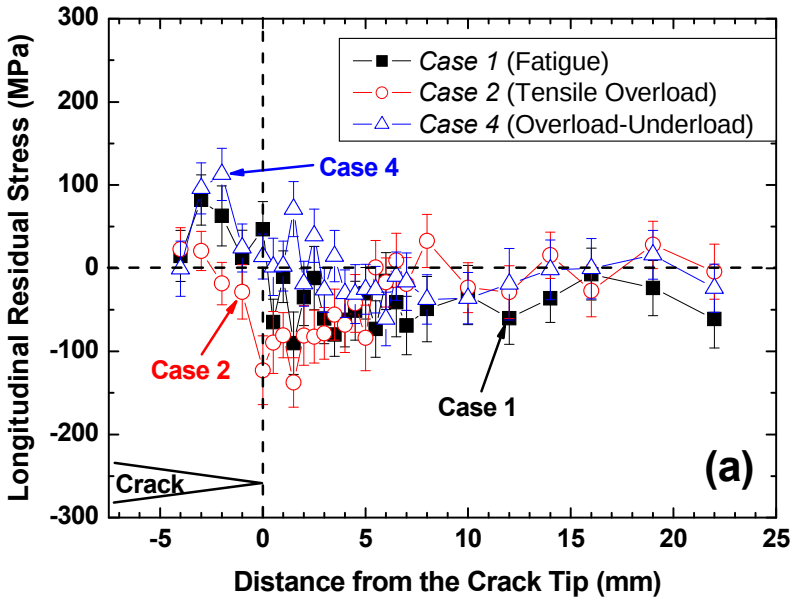
Case 1 (Fatigue)
Case 2 (Tensile Overload)
Case 4 (Overload-Underload)
Case 4
Case 2
Case 1
Crack
(a)
Longitudinal Residual Stress (MPa)
Distance from the Crack Tip (mm)
300
200
100
0
-100
-200
-300
-5
0
5
10
15
20
25

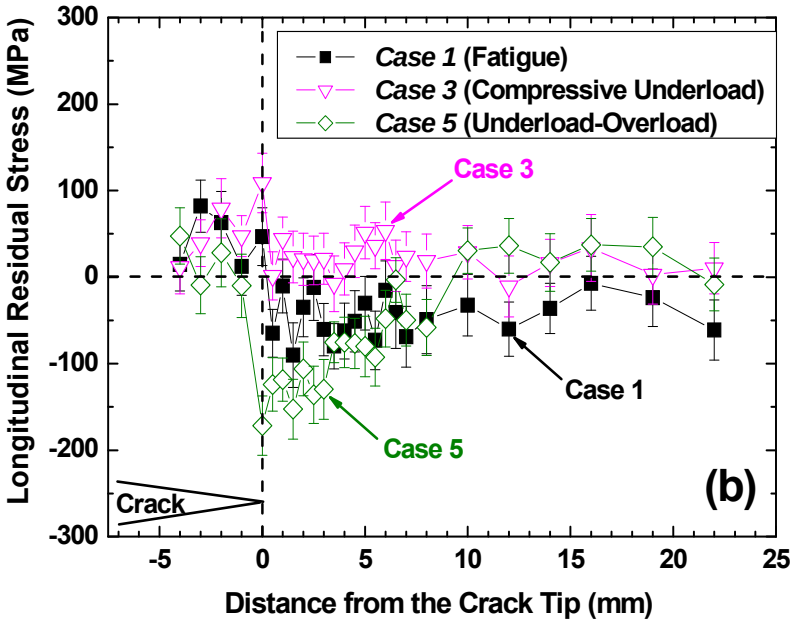
Case 1 (Fatigue)
Case 3 (Compressive Underload)
Case 5 (Underload-Overload)
Case 3
Case 1
Case 5
Crack
(b)
Longitudinal Residual Stress (MPa)
Distance from the Crack Tip (mm)
300
200
100
0
-100
-200
-300
-5
0
5
10
15
20
25

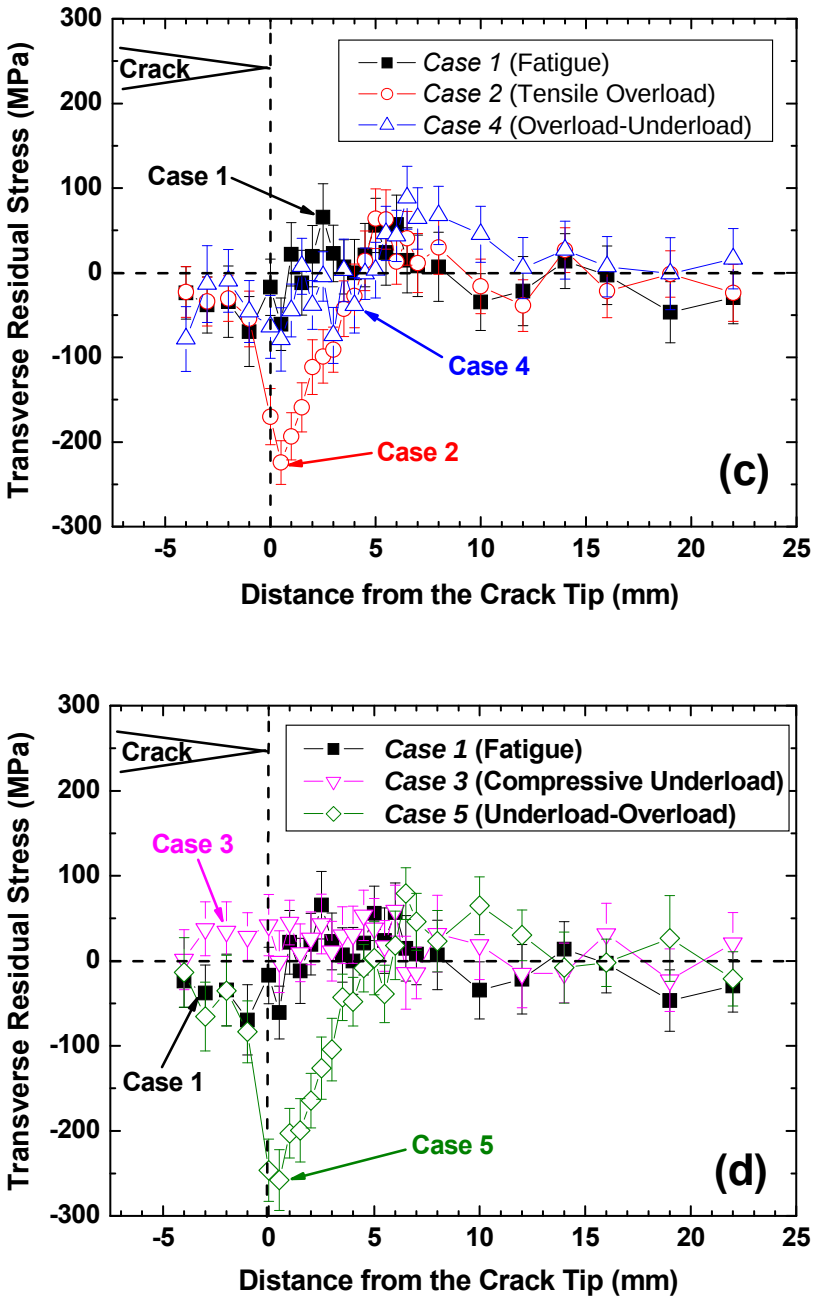

Figure 4.4: Continued.

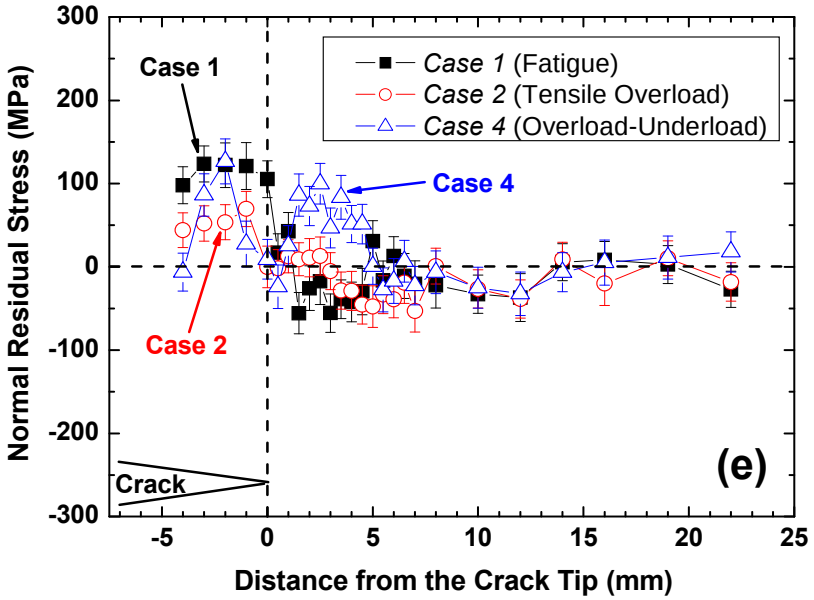

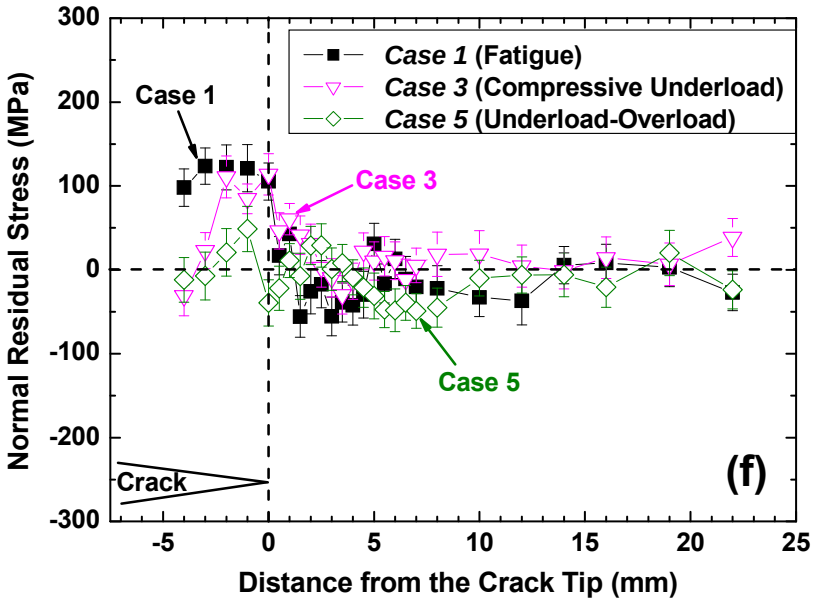

Figure 4.4: Continued.

residual stresses with a maximum of about 125 MPa were observed in a fatigue-wake region, and the sharp transition from tensile to compressive residual stresses was examined about 1 mm ahead of the crack tip. On the other hand, the transverse residual stresses showed an opposite trend. The compressive residual-stress fields with the maximum of about –70 MPa were observed behind the crack tip and the tensile residual stresses were examined from about 1 to 8 mm in front of the crack tip. Interestingly, the transition of residual stresses occurred right ahead of the crack tip for the three stress components.

After *Case 2* (a single tensile overload) was applied, the residual-stress fields near the crack tip were shown in Figs. 4.4(a), (c), and (e). It is noted that the application of tensile overload yielded large compressive residual stresses near the crack tip for the longitudinal component (Fig. 4.4a). For example, the tensile longitudinal residual stresses behind the crack tip observed in *Case 1* changed the compressive residual stresses at –2.5 ~ 0 mm, and the larger compressive residual stresses were developed at 0 (crack tip, –123 MPa) ~ 3 mm. The effect of tensile overload on the transverse residual stresses was more significant. The large compressive residual stresses with a maximum of –225 MPa (at 0.5 mm) were developed within ± 4 mm from the crack tip. It is expected that these enlarged compressive residual-stress fields would affect the determinations of crack-opening level and crack-tip-driving force within the retardation period, and, finally, they would result in the transient crack-propagation behavior, as exhibited in the large retardation period, Fig. 4.3(a). A tensile overload also influenced the normal residual-stress distributions, as shown in Fig. 4.4(e). It was found that the

tensile residual stresses examined in a fatigue-wake region of *Case 1* were significantly reduced. Especially, the tensile residual stresses of 105 MPa (*Case 1*) measured at the crack tip completely disappeared and became zero residual stress (*Case 2*), leading to a double-peak shape near the crack tip.

A compressive underload was imposed right after a tensile overload (*Case 4*) and the corresponding residual-stress profiles were shown in Figs. 4.4(a), (c), and (e). In Fig. 4.4(a), the longitudinal residual-stress distributions showed a similar profile with those of *Case 1*. The large compressive residual stresses near the crack tip generated by the tensile overload changed into the tensile residual-stress fields by the compressive underload. A compressive underload also led to the relatively small compressive residual stresses within 4.5 mm in front of the crack tip for the transverse direction. The maximum compressive transverse residual stress of about –80 MPa was measured at 0.5 mm from the crack tip. It is thought that these reduced compressive-residual stresses ahead of the crack tip are related to the reduced retardation period shown in Fig. 4.3(a). Interestingly, the normal residual stress exhibited the distinct distributions with a wider double-peak shape. It was found that the first tensile maximum was at about 2 mm behind the crack tip, and the second one was at approximately 2.5 mm ahead of the crack tip. It might be due to the results of interaction between newly-developed residual stress fields by the nonuniform reverse plastic deformation and existing residual-stress fields. Based on the changes of residual-stress distribution, it can be thought that the zone of reverse plastic deformation by the compressive underloading influences up to about 5 mm ahead of the crack tip.

After *Case 3* (a single compressive underload) was introduced, the longitudinal, transverse, and normal residual-stress profiles were presented in Figs. 4.4(b), (d), and (f), respectively. It was found that a single compressive underload resulted in the small tensile residual stresses around the crack tip for the longitudinal direction [Fig. 4.4(b)]. It should be noted that the slight tensile transverse residual stresses of about 35 MPa were measured behind the crack tip. It is expected that these tensile stresses in a fatigue wake would result in a smaller crack-opening level, and, thus, higher crack-tip-driving force, which accounts for the initial acceleration immediately after a single compressive underload. A single compressive underload also led to the significant decrease of normal residual stresses at the closer locations (e.g., –4 mm) from the initial notch.

A tensile overload was imposed immediately after a compressive underload (*Case 5*). For the longitudinal direction, the large compressive residual stresses were observed at –1 ~ 8 mm from the crack tip. The maximum compressive residual stress of –170 MPa was measured at the crack tip. Figure 4.4(d) shows the huge compressive transverse residual stresses around the crack tip immediately after applying underload-overload sequence. The largest compressive stress of about –260 MPa was examined at 0.5 mm in front of the crack tip. For the normal direction, the tensile residual stresses behind the crack tip was decreased and a sharp drop of residual stress at the crack tip was also observed right after the tensile overloading, which was consistent with that of *Case 2* [Fig. 4.4(e)]. Overall, the residual-stress distributions of *Case 5* were very similar to those of *Case 2*, likewise, resulting in a large crack-growth retardation period, as shown in Fig. 4.3.

4.4 Summary

In order to obtain a better understanding for the distinct crack-growth characteristics of Hastelloy C-2000 compact-tension specimens subjected to tensile overload, compressive underload, and their mixed loads during fatigue-crack growth, the spatially-resolved neutron-diffraction measurements were performed to directly determine residual-stress distributions in the vicinity of the crack tip, immediately after applying five different variable-amplitude fatigue loadings (i.e., fatigued, tensile overloaded, compressive underloaded, tensile overloaded-compressive underloaded, and compressive underloaded-tensile overloaded). For the longitudinal direction, residual-stress profiles showed the distinguishable difference under various loading conditions except Case 4. The residual-stress distribution of Case 4 did not show much difference with that of Case 1, which fails to explain the reduced retardation period. The normal residual-stress distributions seem to be irrelevant to directly connect the relationship between the residual stress and crack-growth behavior. Among three principal residual-stress components, the transverse residual-stress distributions near the crack tip revealed the most distinct profiles, which can be closely associated with the experimentally-measured different crack-growth behaviors under the five different loading cases.

Chapter 5

Neutron and X-ray Microbeam Diffraction Studies around a Fatigue-Crack Tip after Overload

5.1 Introduction

The accurate understanding of micromechanism for the load-interaction effects during fatigue-crack growth is essential for the damage tolerance design and the development of lifetime-prediction model. One aspect that is still not fully understood is the overload effect and crack closure behavior in the structural materials subjected to cyclic loading. A variety of crack-closure measurements have been utilized to investigate the crack growth retardation mechanisms for structural materials (Elber, 1971; Gan & Weertman, 1981; Davidson, 1991; Guvenilir et al., 1997; Wallhead et al., 1998; Wong et al., 2000; Sarma et al., 2001; Andersson et al., 2006; Okayasu et al., 2006). However, the various closure measurements between surface and bulk resulted in the different closure levels (Clarke & Cassatt, 1977). In addition, due to a lack of experimental capabilities to measure strain/stress fields within the bulk under the applied load, the relationship between overload and retardation has not been quantitatively established.

Recently, a neutron-diffraction measurement was performed to probe the crack closure phenomena after an overload during fatigue crack growth (Sun et al., 2005). The

deep penetration capability of neutrons enables the nondestructive studies of the bulk crack-closure behavior, as compared to the surface crack closure phenomena observed using strain gauge (Gan & Weertman, 1981). Furthermore, the changes in internal strains can be measured *in situ* under the applied load using the load frame as a function of the distance from the crack tip. At the same time, the dislocation density can be carried out from the diffraction peak profile analyses (Mughrabi, 1983; Ungar et al.1999; Barabash 2001). On the other hand, polychromatic X-ray microdiffraction (PXM) is an emerging tool for studying mesoscale structure and dynamics in materials. From the polychromatic methods combined with differential aperture X-ray microscopy (Larson et al, 2002), the local crystal phase, orientation (texture), and local defect distribution including elastic and plastic strain can be determined (Ice et al., 2005; Ice et al., 2006).

In this study, the evolutions of elastic-lattice strains around a crack tip were investigated as a function of the applied load during tensile loading cycles immediately after overload using *in-situ* neutron diffraction. The crack opening load was determined by neutron diffraction. The dislocation density distributions around a crack tip were estimated from the diffraction peak broadening. Moreover, the local lattice orientation variations near a crack tip were examined using polychromatic X-ray microdiffraction.

5.2 Experimental Details

A compact-tension (CT) specimen of a Type 316 nitrogen-added stainless steel was used for the fatigue crack propagation experiment, as shown in Figure 5.1. The

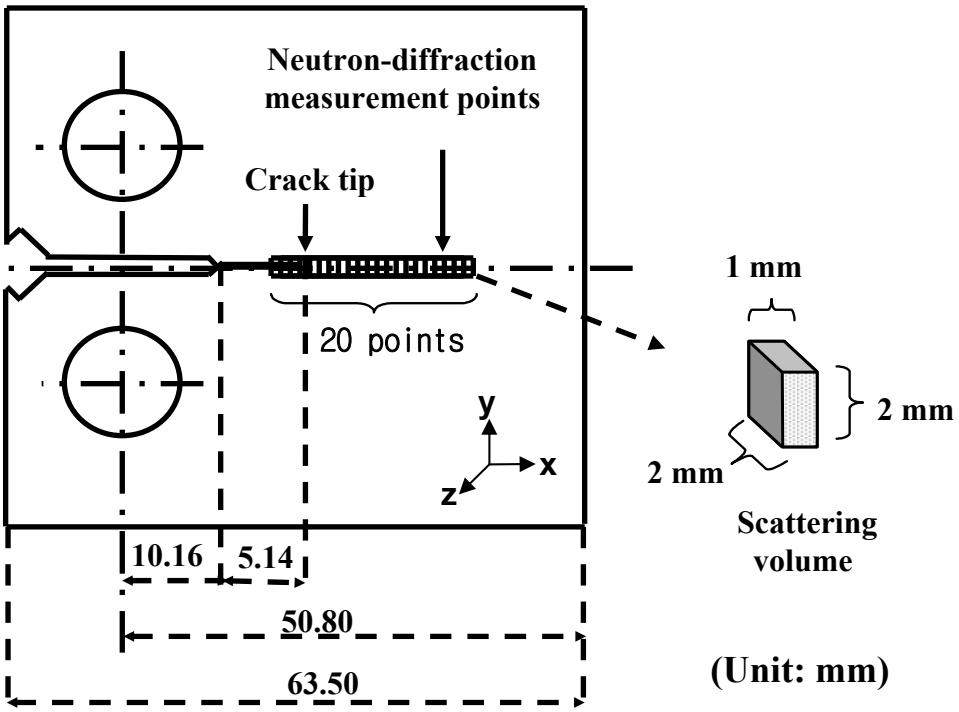

Figure 5.1: Geometry of a compact-tension specimen. Diffraction patterns were measured along the cracking path with a scattering volume of 4 mm^3.

specimens were prepared according to the American Society for Testing and Materials (ASTM) Standard E647-99 (ASTM, 2000). The crack-growth experiments were performed under a constant-load-range-control mode with a frequency of 10 Hz and a load ratio, R, of 0.1 [$R = P_{min}/P_{max}$, P_{min} and P_{max} are the applied minimum (988 N) and maximum (9,880 N) loads, respectively]. The crack length was measured by compliance method using crack-opening-displacement (COD) gauge. The stress-intensity factor, K, was obtained (Liaw et al., 1982),

$$K = \frac{P(2+\alpha)}{B\sqrt{W}(1-\alpha)^{3/2}}(0.886 + 4.64\alpha - 13.32\alpha^2 + 14.72\alpha^3 - 5.6\alpha^4) \qquad (5.1)$$

where P = applied load, B = thickness, W = width, $\alpha = a/W$; a = crack length for a CT specimen, and $\Delta K = K_{max} - K_{min}$ (K_{max} and K_{min} are the maximum and minimum stress-intensity factors, respectively). When the crack length reaches 15.3 mm, a single tensile overload, 13,189 N, which is 133% of P_{max}, is applied. After the overload was imposed, the fatigue crack retardation period was observed, as presented in Figure 5.2.

In-situ neutron-diffraction measurements were conducted on the Spectrometer for MAterials Research at Temperature and Stress (SMARTS) (Bourke et al., 2002) at the Los Alamos Neutron Science Center (LANSCE). The specimens were aligned 45° from the incident neutron beam, which is the continuous energy spectrum. The entire diffraction pattern was recorded in two stationary detector banks with diffraction angle $2\theta = \pm 90°$. Thus, the diffraction vectors were parallel to the in-plane (IP) and through-

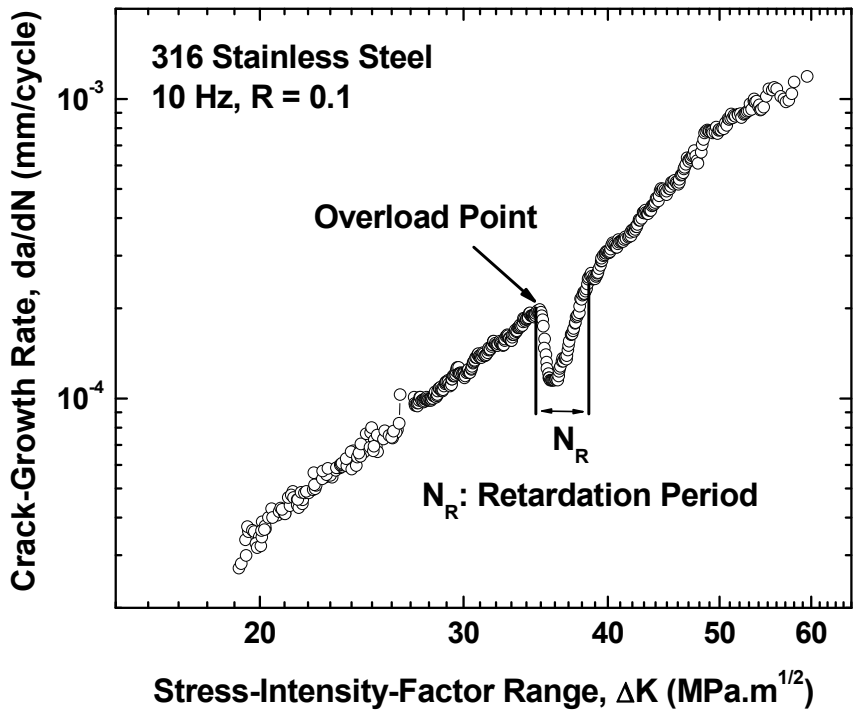

Figure 5.2: Fatigue-crack-growth rate as a function of the stress-intensity-factor range.

thickness (TT) directions of the specimen. The incident beam was defined by 2-mm horizontal and 1-mm vertical slits, and the diffracted beams were collimated by 2-mm radial collimators, resulting in a 4-mm^3 gauge volume. The lattice parameters were obtained using the Rietveld refinement (Rietveld, 1969) in General Structure Analysis System (GSAS) (Larson & Von Dreele, 2004), and the lattice strains were calculated by the changes in the lattice parameter, a, at the different applied loads during tensile loading and unloading cycles with respect to stress-free reference lattice parameter, a_0, measured away from the crack tip, as shown in the following equation:

$$\varepsilon = \frac{a - a_0}{a_0} \tag{5.2}$$

Spatially-resolved strain mapping was performed during the tensile loading cycle immediately after overload, as shown in Figure 5.3. At each load, the twenty diffraction patterns in both IP and TT directions were measured as a function of the distance from the crack tip.

The pseudo-voigt function is employed to decompose Gaussian and Lorentzian peak broadening component from the single peak fitting in GSAS. The full-width-half-maximum of Gaussian ($FWHM_G$) and Lorentzian ($FWHM_L$) can be used as an input to calculate the randomly-distributed dislocation density and the distance between dislocation walls, respectively (Huang et al., 2007). As a first approximation, the dislocation density is calculated, assuming that dislocation activities for all primary slip systems are equal. The randomly-distributed dislocation density (n) is calculated as follows (Barabash, 2001; Huang et al., 2007):

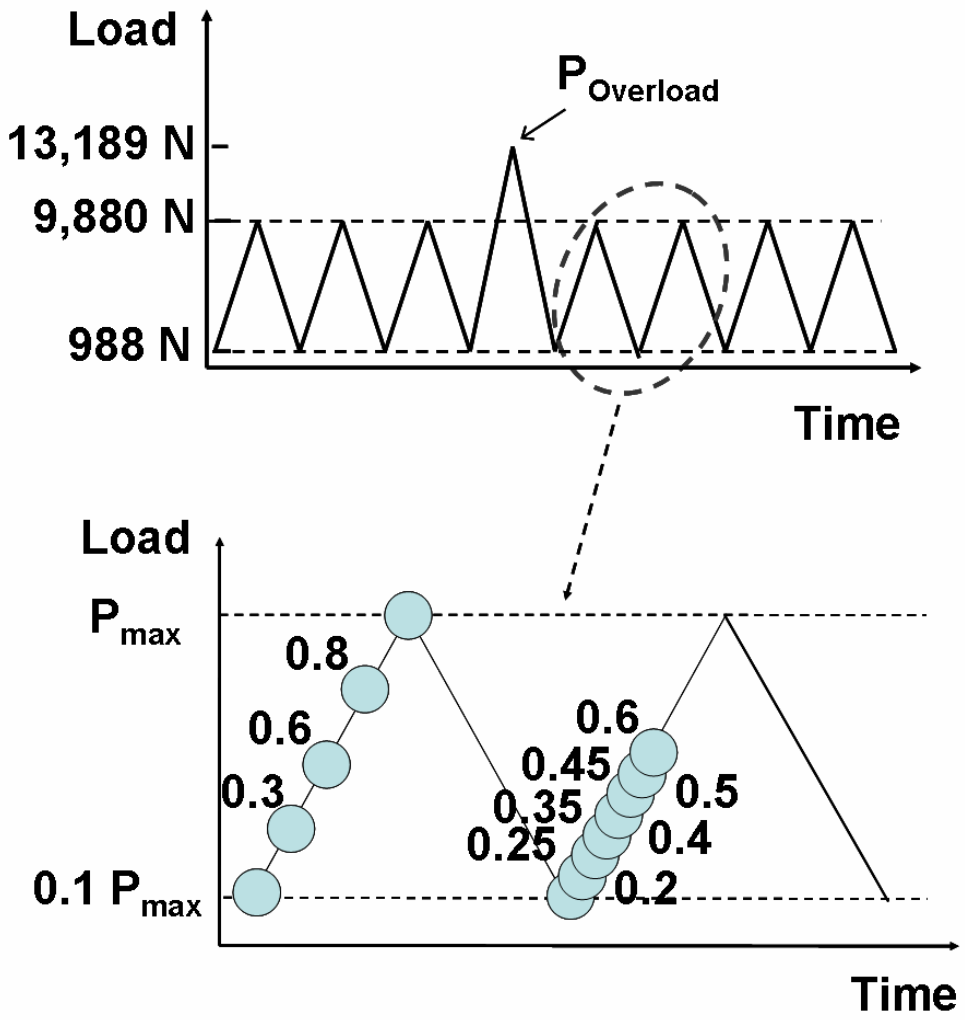

Figure 5.3: Tensile loading and unloading sequence applied immediately after an overload. At each load point, neutron strain mapping was performed as a function of the distance from the crack tip. Note that number in the lower graph is a load ratio (e.g., 0.6 means that 60% of P_{max} is applied).

$$n \sim \left(\frac{FWHM_G \times d_{hkl}}{C \times |b|} \right)^2 \tag{5.3}$$

where $FWHM_G$ is the full-width-half-maximum of Gaussian, d_{hkl} is d-spacing for each hkl plane, and C is the contrast factor, and b is the Burgers vector.

Polychromatic X-ray microdiffraction combined with differential aperture microscopy was used to study the local plastic deformation around a crack tip on the beamline ID-34-E at the Advanced Photon Source. A focused 0.5 μm diameter polychromatic synchrotron beam penetrates a specimen and the beam produces a Laue pattern from each subgrain that it intercepts. With a differential aperture microscopy technique, the depth-resolved three-dimensional crystal orientation distributions were investigated. The surface of specimen is inclined at 45° from the incident beam, and a charge coupled device (CCD) area detector is placed at 90° relative to the incident beam (Barabash et al., 2005). The crystallographic orientation distributions are examined as a function of depth at two locations near a crack tip after the overload, as indicated in Figure 5.4. Note that z is the through-thickness direction of the specimen.

5.3 Results and Discussion

5.3.1 Lattice-Strain Evolution

The internal strain evolutions were investigated with increasing the applied load near a crack tip after an overload. The in-plane lattice-strain profiles were measured as a function of the applied load, as shown in Figure 5.5. After a single tensile overload was

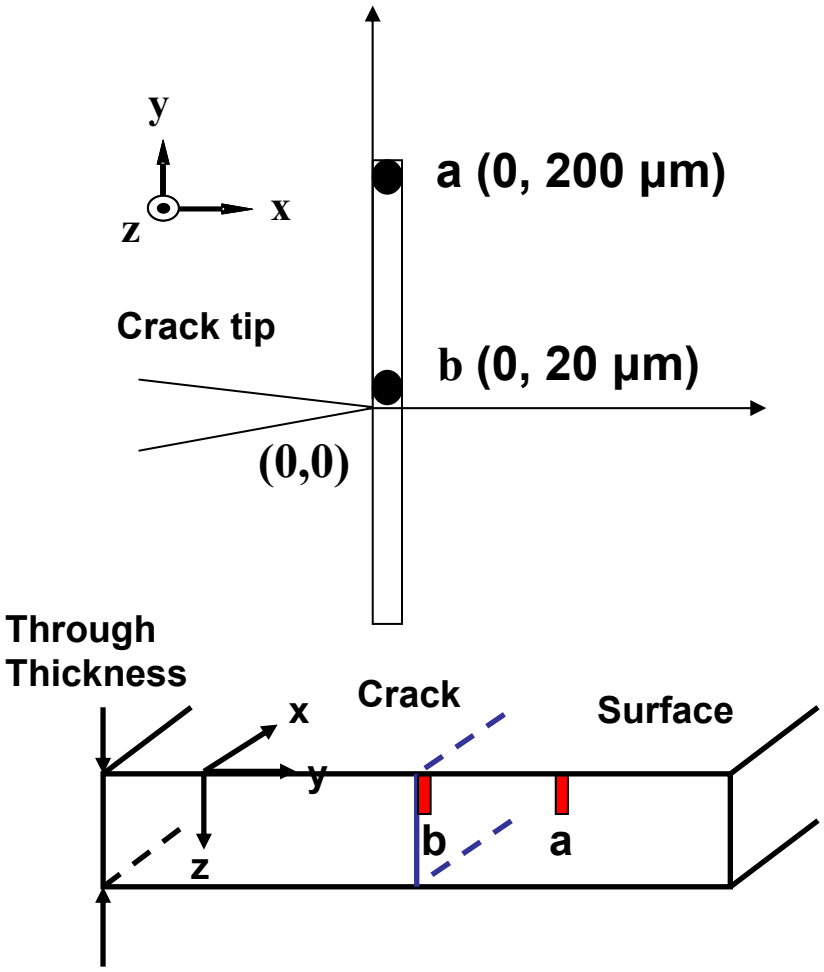

Figure 5.4: Locations from the crack tip measured by polychromatic X-ray microdiffraction combined with differential aperture microscopy.

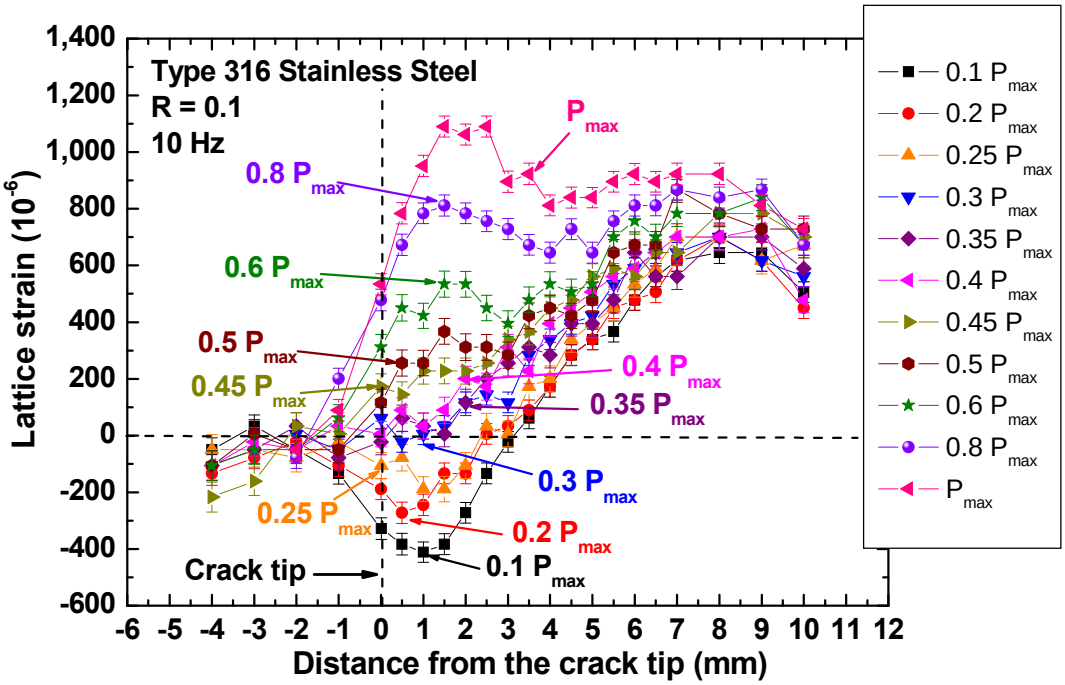

Figure 5.5: Lattice-strain evolutions around a crack tip with increasing the applied load.

imposed, the large compressive strains were observed within ± 3 mm near a crack tip. At 1 mm in front of the crack tip, the largest compressive strain of –410 με (micro strain) was examined. As the distance from the crack tip increases, strain changes from compressive to tensile. The maximum tensile strain was observed at about 8 mm ahead of the crack tip. As the applied load increases, it can be noted that strains behind the crack tip do not change much, while strains in front of the crack tip evolve with increasing the applied load. When about 0.3 P_{max} (30% of maximum load) was applied, all compressive strains around a crack tip disappeared and became zero. This load value corresponds to the crack-opening load. As the load increases from 0.3 P_{max} to P_{max}, strain gradually increases, especially, at the region in front of the crack tip. At P_{max}, the maximum tensile strain of 1,100 με was observed at 1.5 mm ahead of the crack tip.

Figure 5.6 presents the lattice strain variations as a function of the applied load at the specific locations from the crack tip. It should be noted that the load response of lattice strain was dependent on the location from the crack tip. Strains do not change much with increasing the applied load at the region behind the crack tip, while strains increase linearly with increasing the applied load at locations in front of the crack tip. Especially, at 1 mm ahead of the crack tip, the lattice-strain change is the largest and strain changes are diminished, as the distance from the crack tip increases. Note that the lattice-strain change is corresponding to the slope of load ratio versus lattice strain. A slope is steep at the region behind the crack tip and it is the lowest at 1 mm in front of the crack tip, and then it become higher, as the distance from the crack tip increases. A high slope indicates that the lattice strains do not change much with increasing the

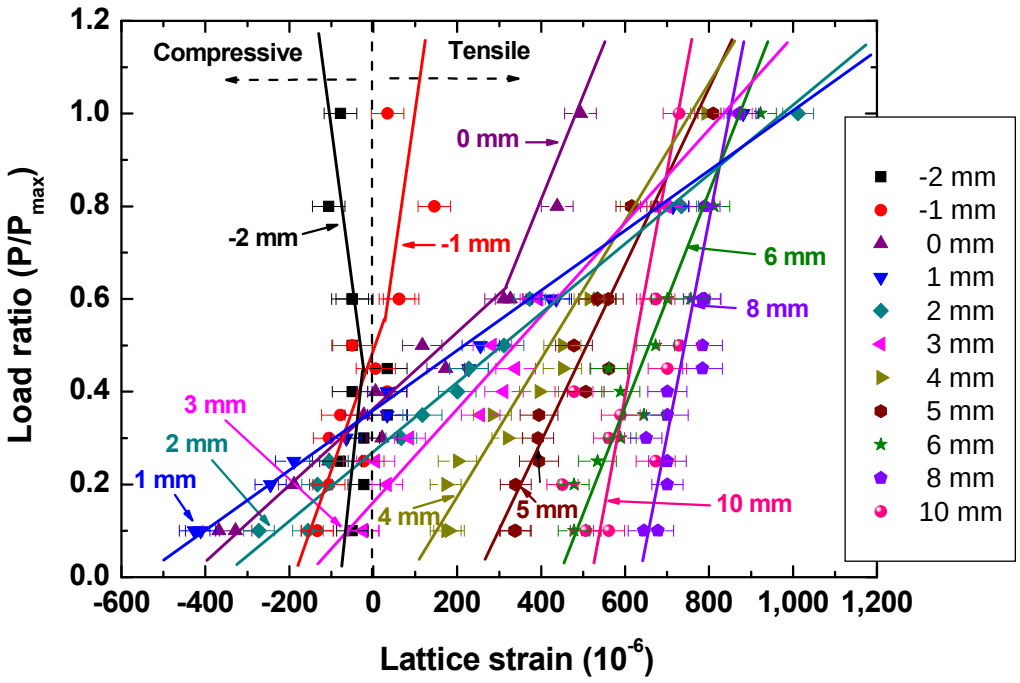

Figure 5.6: Lattice-strain change as a function of the applied load at specific locations from the crack tip.

applied load. In other words, as the applied load increases, stress is not effectively applied at the region behind of the crack tip and far away from the crack tip. On the other hand, a low slope means that the lattice strain changes greatly, as the applied load increases. Thus, it could be thought that stress is systematically imposed with increasing the applied load at near location in front of the crack tip, resulting in larger lattice-strain change and lower slope. As a result, it should be emphasized that the changes of slope at specific locations from the crack tip are exactly corresponding to the stress distributions in front of the crack tip.

Various crack closure measurements have been empolyed to investigate the crack opening load precisely (Elber, 1971; Clarke & Cassatt, 1977; Gan & Weertman, 1981; Davidson, 1991; Guvenilir et al., 1997; Wallhead et al., 1998; Wong et al., 2000; Sarma et al., 2001; Andersson et al., 2006; Okayasu et al., 2006). Neutron diffraction can be used as an unique tool for the bulk crack closure measurement, which facilitates the measurements of bulk strain/stress fields around a crack tip under the applied loads. There are several approaches to determine the crack opening load. The common way is to measure the deviation point from the linearity in the plot of load (or stress) versus strain. The other we proposed is to examine the load value to remove the compressive lattice strain presented in Figure 5.6. The fatigue crack should overcome the compressive residual strain/stress near a crack tip for the crack propagation. The load ratio values to remove the compressive residual strains at various locations from the crack tip are indicated in Figure 5.7. It was found that the compressive residual strains

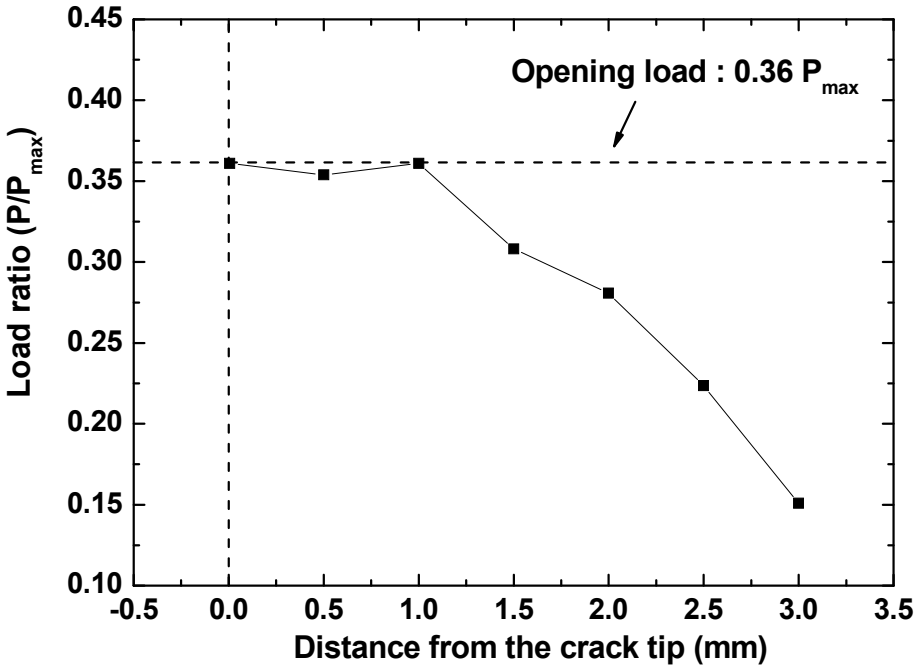

Figure 5.7: Crack opening load at specific locations from the crack tip.

were removed with a load value of 0.36 P_{max} at the crack tip and 0.15 P_{max} at 3 mm ahead of the crack tip. As a result, 0.36 P_{max} is determined as the crack opening load right after overload, which enables all compressive residual strains at regions in front of the crack tip as well as the crack-tip position to disappear and become zero.

5.3.2 Dislocation Density and Crystallographic Tilt

The dislocation density was measured from Gaussian peak broadening deconvoluted by pseudo-voigt function in GSAS. Figure 5.8 shows the dislocation density distributions along IP direction as a function of the distance from the crack tip right after an overload. For the grains of (111) orientation, high dislocation densities of 10 x 10^{10} cm^{-2} are observed within ± 3 mm from a crack tip. As the distance from the crack tip increases, the dislocation density decreases tremendously. Note that the average dislocation density obtained from the broadening of several *hkl* diffractions means the randomly distributed dislocation density in the gauge volume investigated. The high dislocation densities of approximately 8.5 x 10^{10} cm^{-2} are examined near a crack tip, supporting that the overload induced the severely large plastic deformation at the crack tip. From the dislocation density distributions, the plastic zone size resulted from an overload seems to be approximately 5 mm in front of the crack tip.

In order to study the localized plastic deformation on the submicron scale, polychromatic X-ray microdiffraction was applied to investigate the lattice distortions beneath the specimen surface around a crack tip. Figure 5.9 presents the relative

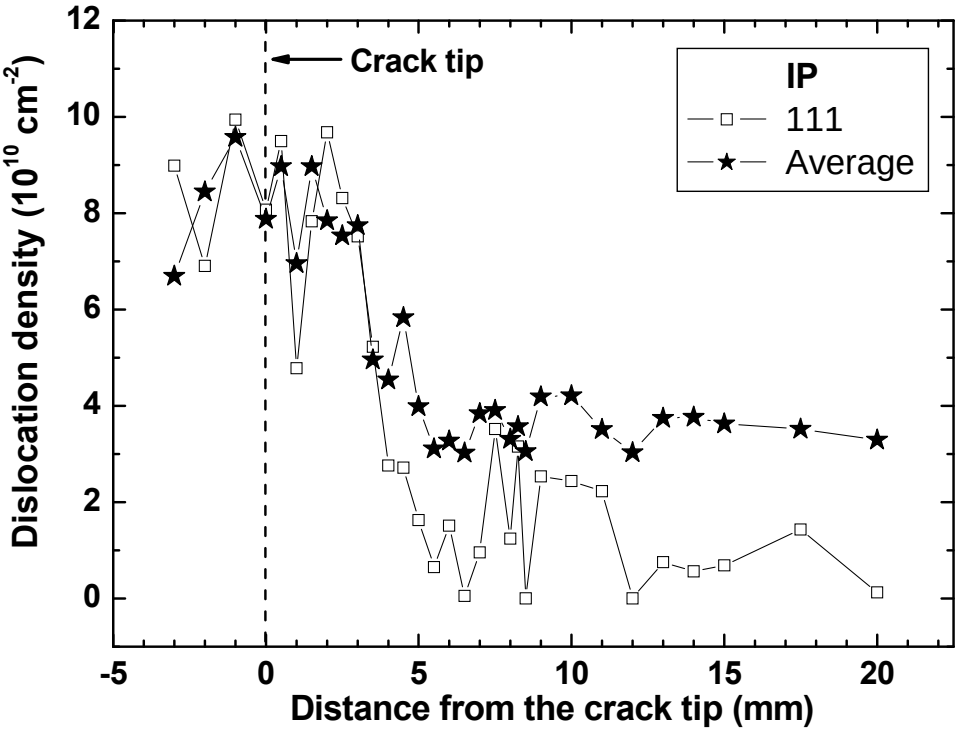

Figure 5.8: Dislocation density distributions around a crack tip in IP direction.

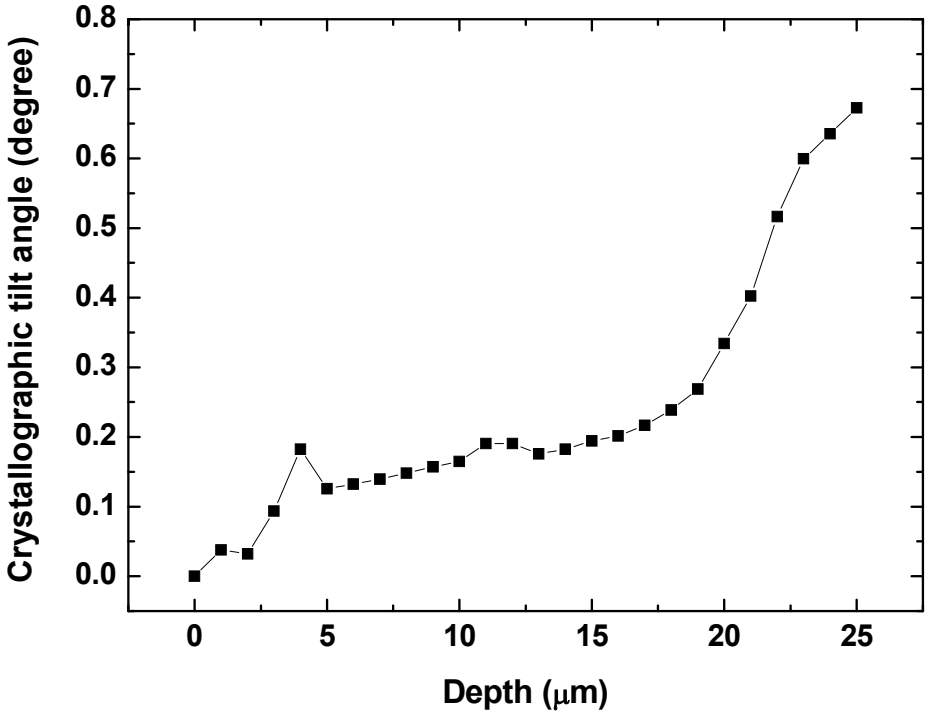

Figure 5.9: Change of misorientation at location “a” shown in Fig. 5.4.

orientation change of C-axes, as compared to the starting point, which is the specimen surface. The location examined is 200 μm far away from the crack tip along y direction (a location in Figure 5.4). As the depth increases, the lattice distortions are obviously measured. The crystallographic tilt angle of 0.67° was observed at 25 μm beneath surface. Figure 5.10(a) shows the rotation angle changes with increasing the depth at the close location from the crack tip (b location in Figure 5.4). As the depth increases, two distinct groups of rotation angles are examined, revealing that another grain appears at 11 μm below the surface. The rotation angle between two grains was 32°. The rotation angles of grains 1 and 2 were shown in Figures 5.10(b) and (c), respectively. The maximum tilt angles of 0.58° and 0.57° were observed in the grain 1 and grain 2, respectively. As a result, the crystallographic tilts were significantly observed around a crack tip immediately after overload using a differential aperture X-ray microscopy technique. It should be noted that severe lattice distortions measured from X-ray microdiffraction are consistent with the high dislocation densities near a crack tip calculated from neutron peak broadening.

5.4 Conclusions

A retardation period in the fatigue-crack-growth rate was observed after overload. From an *in-situ* neutron-diffraction measurement, the bulk elastic-lattice strains near a crack tip were measured as a function of the applied load. The large compressive residual strains were observed within ± 3 mm near a crack tip right after the overload. As the applied load increases, strains gradually increase at the region in

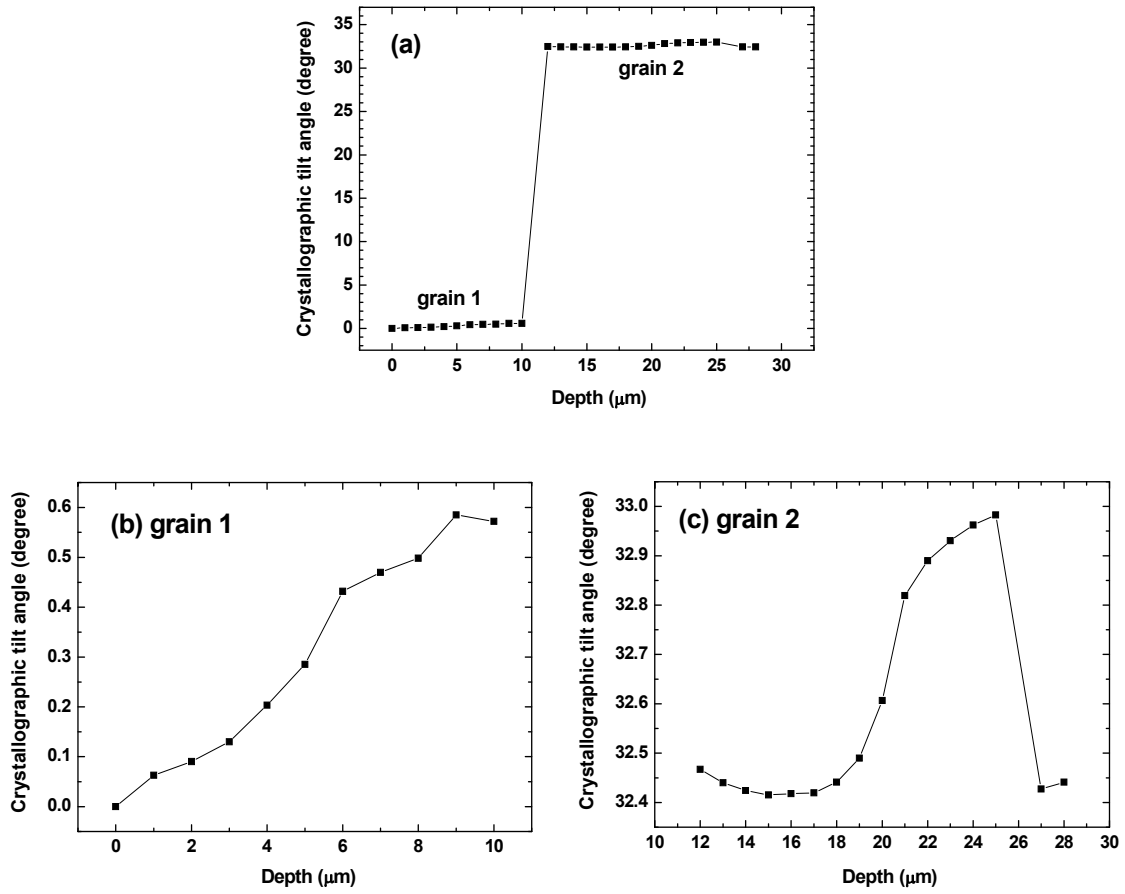

Figure 5.10: (a) Change of misorientation at location "b" shown in Fig. 5.4; (b) change of misorientation in grain 1; and (c) change of misorientation in grain 2.

front of the crack tip. However, strains behind the crack tip do not change much with increasing the applied load. From neutron peak profile analyses, the high dislocation densities were measured near a crack tip and sharply decreased with increasing the distance from the crack tip. Moreover, the local orientation variations were examined near a crack tip using polychromatic X-ray microdiffraction combined with differential aperture microscopy. This reveals that crystallographic tilts are considerably observed beneath surface around a crack tip, which is in good agreement with high dislocation densities near a crack tip measured by peak profile analyses using neutron diffraction.

Chapter 6

Evolution of Residual-Strain Distribution through an Overload-Induced Retardation Period during Fatigue-Crack Growth

6.1 Introduction

Since Paris and co-workers first proposed a relationship between the fatigue-crack-growth rate and the stress-intensity-factor range (i.e., the driving force for fatigue-crack growth) during constant-amplitude cyclic loading in 1961, their approach has been widely used for characterizing fatigue-crack propagation (Paris et al., 1961). More recently, many researchers have drawn much attention to interpret and predict crack-growth behavior under 'variable-amplitude' fatigue loading, in particular with respect to a single tensile overload case. A single tensile overload (i.e., the load greater than the maximum load in constant-amplitude cyclic loading) applied during constant-amplitude cyclic loading leads to a large crack-growth-retardation period, which, consequently, increases the fatigue lifetime (Gan & Weertman, 1981; Fleck et al., 1983; Brahma et al., 1989; Shin & Hsu, 1993; Hou & Charng, 1996; Dougherty et al., 1997; Wallhead & Edwards, 1998; Borrego et al., 2001; Ellyin & Ozah, 2007; Lee et al., 2008). Various models have been suggested to account for the crack-growth-retardation behavior following the overload. In general, these retardation models can be classified into two methods: the crack-closure approach and the crack-tip plasticity approach.

The fatigue-crack closure, even at far-field tensile loads, was first discovered experimentally by Elber (1971). He observed the changes in compliance during the loading cycle and interpreted it as a gradual crack opening from a closed crack in the region of a crack wake. Elber postulated that crack growth would not occur if the crack tip was closed, and he introduced the "effective" stress-intensity-factor range (ΔK_{eff}) as a crack-tip driving force:

$$\Delta K_{eff} = K_{max} - K_{op} \tag{6.1}$$

where K_{max} and K_{op} denote the stress-intensity factors at the maximum load and crack opening, respectively. Yuen and Taheri reported that the crack-opening load (or stress) depends on the residual stresses developed by the prior loading history (Yuen & Taheri, 2006). For example, as the crack propagates through an overload-induced plastic zone, the residual stresses in the zone increase the crack-opening load and cause the crack-growth retardation. Makabe et al. (2004) also pointed out the significance of the residual stress on the crack closure and ΔK_{eff}.

A crack-tip plasticity model is based on the assumption that crack-growth retardation occurs due to a large overload-induced plastic zone. Willenborg et al. (1971) proposed that the degree of retardation was governed by compressive residual stresses acting on the crack tip, which were developed due to the large plastic deformation caused by an overload. The Willenborg model computes the effective stress-intensity factor being reduced by the compressive residual stress. The Wheeler (1972) model is one of the most widely used models for the fatigue-crack-growth prediction under variable-amplitude loading. Wheeler presented how to improve the accuracy of crack-

growth predictions in metals subjected to variable-amplitude cyclic loading. His model introduced a retardation parameter, determined by the current plastic-zone size, overload plastic-zone size, and crack increment from the overload point, to calculate the crack-propagation rate within the perturbed plastic zone after a single tensile overload. Using Wheeler's assumptions and models, the crack-growth retardation can be computed with a reasonable accuracy. However, if the multiple overloads or underloads following an overload are applied, or the materials experience the initial acceleration of crack growth, the model cannot be used in the current form and a new retardation parameter should be determined (Yuen & Taheri, 2006; Goel & Chand, 1994; Kim & Shim, 2003; Rushton & Taheri, 2003).

To summarize, the accurate measurement of residual stresses near the crack tip and the investigation of interactions between the overload plastic zone and current plastic zone with the crack advance in the perturbed plastic zone are the key for successful crack-growth predictions in both approaches. However, there are only a few direct quantitative investigations on describing complete crack-tip stress/strain fields accompanying fatigue-crack growth (James et al., 2004; Steuwer et al., 2006; Sun et al, 2006; Croft et al., 2007; Daymond et al., 2007; Barabash et al., 2008; Lee et al., 2009). Especially, experimentally-determined residual stresses around a crack tip in the perturbed plastic zone after a tensile overload are limited.

In this investigation, the effects of a single tensile overload on the plastic-zone size, residual strains/stresses, and the crack-growth rate were studied. The residual strains and stresses in the perturbed plastic zone were investigated using neutron

diffraction, which is a useful method of probing the bulk-averaged elastic-lattice strain and stress in the polycrystalline material from the shift of the diffraction peaks. The residual strains and stresses were measured as a function of the distance from the crack tip along the direction of crack propagation. At some crack-growth stages, two-dimensional neutron-strain mapping was conducted to observe the crack-tip strain fields in detail. More importantly, the relationship between the overload-induced plastic zone and subsequent fatigue-induced plastic zone; and its influence on the residual strain/stress profiles in the perturbed plastic zone will be discussed.

6.2 Experimental Details

6.2.1 Material and Fatigue-Crack-Growth Experiments

A type 316-low-carbon nitrogen-added stainless steel was used in this study. This material has a single-phase face-centered-cubic (FCC) structure, no preferred texture, yield strength of 288 MPa, Young's modulus of 210 GPa, and the average grain size of 50 μm. The compact-tension (CT) specimen [Figure 6.1(a)] was prepared according to the American Society for Testing and Materials (ASTM) Standards E647-99 (ASTM, 2000). The CT specimens are pre-cracked under a fatigue-loading condition using a Material Test System (MTS) servohydraulic machine. Fatigue loading was performed under a constant load-range-control mode with a frequency of 10 Hz and a load ratio, R, of 0.1 [$R = P_{min}/P_{max}$, P_{min} and P_{max} are the applied minimum (988 N) and maximum (9,880 N) loads, respectively]. The stress-intensity-factor, K, value was obtained, using the following equation (Liaw et al., 1982):

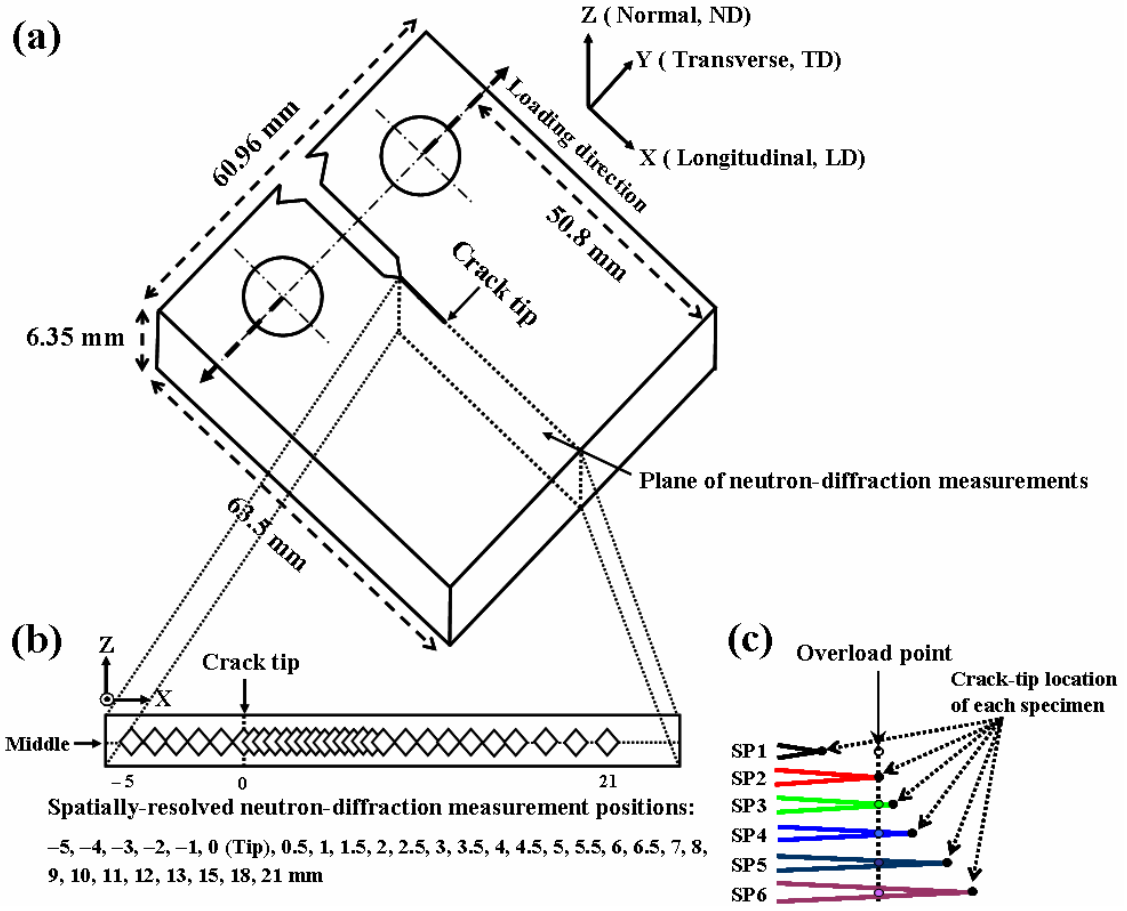

Figure 6.1: Schematic of (a) a 316-LN-stainless steel compact-tension specimen, (b) spatially-resolved neutron-diffraction measurement positions along the direction of the crack propagation (x), and (c) the crack-tip position for each specimen relative to the overload point. Note that an overload point is the same as the crack-tip position of the SP2.

$$K = \frac{P(2+\alpha)}{B\sqrt{W}(1-\alpha)^{3/2}}(0.886 + 4.64\alpha - 13.32\alpha^2 + 14.72\alpha^3 - 5.6\alpha^4) \qquad (6.2)$$

where P = applied load, $\alpha = a/W$, a = crack length, W = specimen width, and B = specimen thickness. The crack length was measured by the crack-opening-displacement (COD) gauge using the compliance technique (Liaw et al., 1983; Logsdon & Liaw, 1986; Liaw et al., 1991).

The sizes of the overload plastic zone, $R_{y(o)}$, and current plastic zone, $R_{y(c)}$, were defined following Irwin's estimation (Irwin, 1957):

$$R_{y(o)} = \frac{1}{\beta\pi}\left(\frac{K_o}{\sigma_y}\right)^2 \qquad (6.3)$$

$$R_{y(c)} = \frac{1}{\beta\pi}\left(\frac{K_{\max}}{\sigma_y}\right)^2 \qquad (6.4)$$

where K_o and K_{max} are the stress-intensity factors at the overload point and the maximum load in the constant amplitude, respectively; and β = 1 or 3 for the plane stress and strain conditions, respectively; and σ_y is the yield strength of the material.

When the crack length reached 15.3 mm, a single tensile overload (13,189 N, which is 1.33 P_{max}) was applied during the constant-amplitude fatigue loading. Figure 6.2 shows the experimental fatigue-crack-growth results. In Figure 6.2(a), the crack length, a, was plotted as a function of the number of fatigue cycles, N, with a sketch of the fatigue-loading pattern following a single tensile overload. After the tensile overload was applied, the crack-growth-retardation period was clearly observed. The total post-

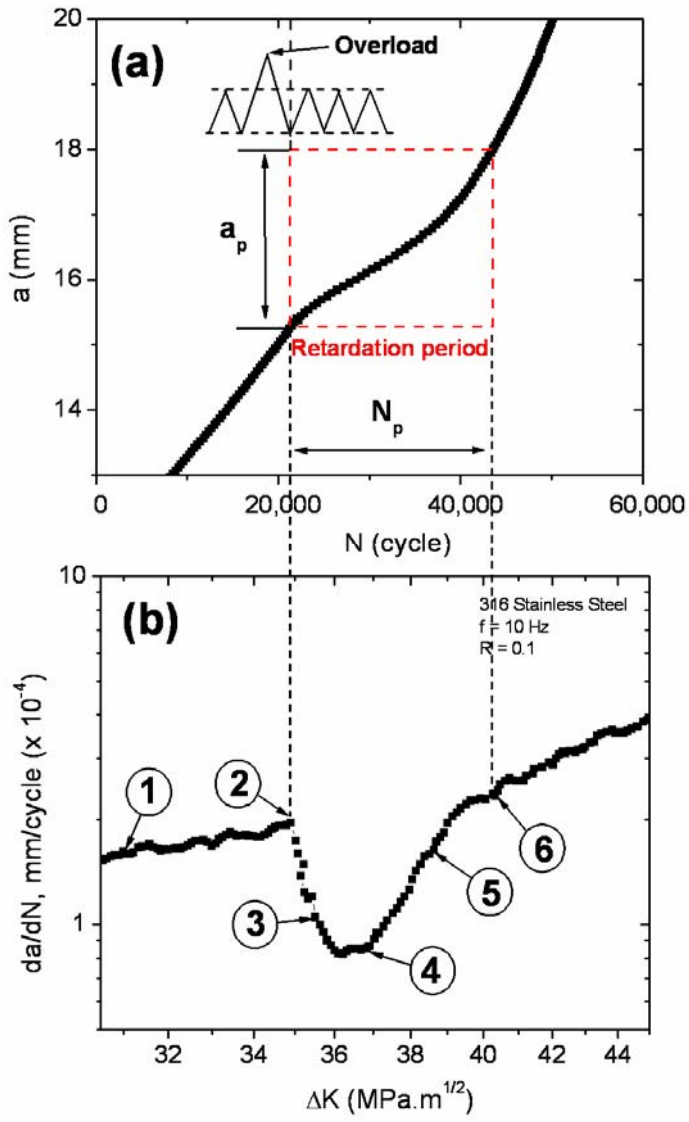

Figure 6.2: The fatigue-crack-growth results following a single tensile overload: (a) crack length, *a*, vs. number of fatigue cycles, *N*, and (b) crack-growth rate, d*a*/d*N*, vs. stress-intensity-factor range, Δ*K*. Six specimens prepared at different crack-growth stages through the retardation period were used for neutron residual strain/stress mapping.

overload crack growth, a_p, was about 2.7 mm, and the number of post-overload cycles, N_p, was approximately 22,000 cycles. Figure 6.2(b) shows the crack-growth rate, da/dN, versus the stress-intensity-factor range, ΔK (= K_{max} – K_{min}, K_{max} and K_{min} are themaximum and minimum stress-intensity factors, respectively). The crack-growth rate, da/dN, was obtained by a seven-point incremental polynomial technique (ASTM, 2000).

A total of six compact-tension (CT) specimens were prepared to represent different crack-growth stages through the da/dN versus ΔK curve. Details of the specimen preparation are summarized in Table 6.1. The specimen 1 (SP1) was subjected only to the fatigue deformation and did not experience the overload. The specimen 2 (SP2) was stopped immediately after a single tensile overload at the crack length of 15.3 mm. After the tensile overload was applied, the crack-growth rate was sharply reduced. The specimen 3 (SP3) was prepared within this reduced period at the crack length of 15.6 mm. After the minimum crack-growth velocity, the crack-growth rate began to increase. The specimen 4 (SP4) was prepared near the minimum point at the crack length of 16.3 mm, and the specimen 5 (SP5) was prepared during this gradual increase of the crack-growth rate when the crack length reached 17.2 mm. Eventually, the crack-growth rate was recovered to pre-overload slope of the da/dN versus ΔK curve at the crack length of 18 mm where the specimen 6 (SP6) was prepared.

Table 6.1: Details on the sample preparation for the neutron-diffraction strain-mapping experiments.

Specimens	**1**	**2**	**3**	**4**	**5**	**6**
Crack length (mm)	13.0	15.3	15.6	16.3	17.2	18.0
Number of cycles (N)	8,404	21,527	23,801	32,200	39,579	43,610
d*a*/d*N* (mm/cycle)	1.62×10^{-4}	1.96×10^{-4}	1.05×10^{-4}	8.65×10^{-5}	1.64×10^{-4}	2.36×10^{-4}
Δ*K* (MPa.m$^{1/2}$)	30.98	35.03	35.52	36.90	38.63	40.28
Description	Fatigue	Fatigue + overload	Fatigue + overload + fatigue			
	Before retardation		During retardation			End of retardation

6.2.2 Neutron-Diffraction Strain Measurements

Neutron-diffraction strain mappings were performed using the Neutron Residual Stress mapping Facility (NRSF2) at the High Flux Isotope Reactor of the Oak Ridge National Laboratory. The wavelength of 1.729567 Å was selected from the Si331 doubly-focusing monochromator. The experimental setup for the neutron strain mapping is shown in Figure 6.3. The (311) diffraction peak was recorded in a stationary detector centered on a diffraction angle of $2\theta = 106°$. The longitudinal (ε_x) and normal (ε_z) strains were measured using 1-mm wide and 2-mm tall (y-direction) incident beam slits and 1-mm wide diffracted beam slit. The transverse (ε_y) strain component was measured using 2-mm wide and 1-mm tall (x-direction) incident beam slits and 2-mm wide diffracted beam slit.

For one-dimensional (1-D) strain measurements, about thirty diffraction patterns were recorded for each specimen along the crack-propagation direction (x) as a function of the distance from the crack tip (Figure 6.1b). The crack-tip location identified on the surface of the sample by a scanning-electron microscope was used for spatially-resolved neutron-strain mapping. The scattering volume was positioned in the middle of the specimen thickness for all strain orientations. To observe the evolution of residual strain/stress distributions during crack growth, strain/stress profiles were plotted as a function of the distance from the overload point (see Figures 6.5-6.9). Note that an overload point corresponds to the crack-tip location of the SP2 (Figure 6.1c). For example, the diffraction patterns of the SP4 (overloaded at the crack length of 15.3 mm and further fatigued up to the crack length of 16.3 mm) were measured at – 4 ~ 22 mm

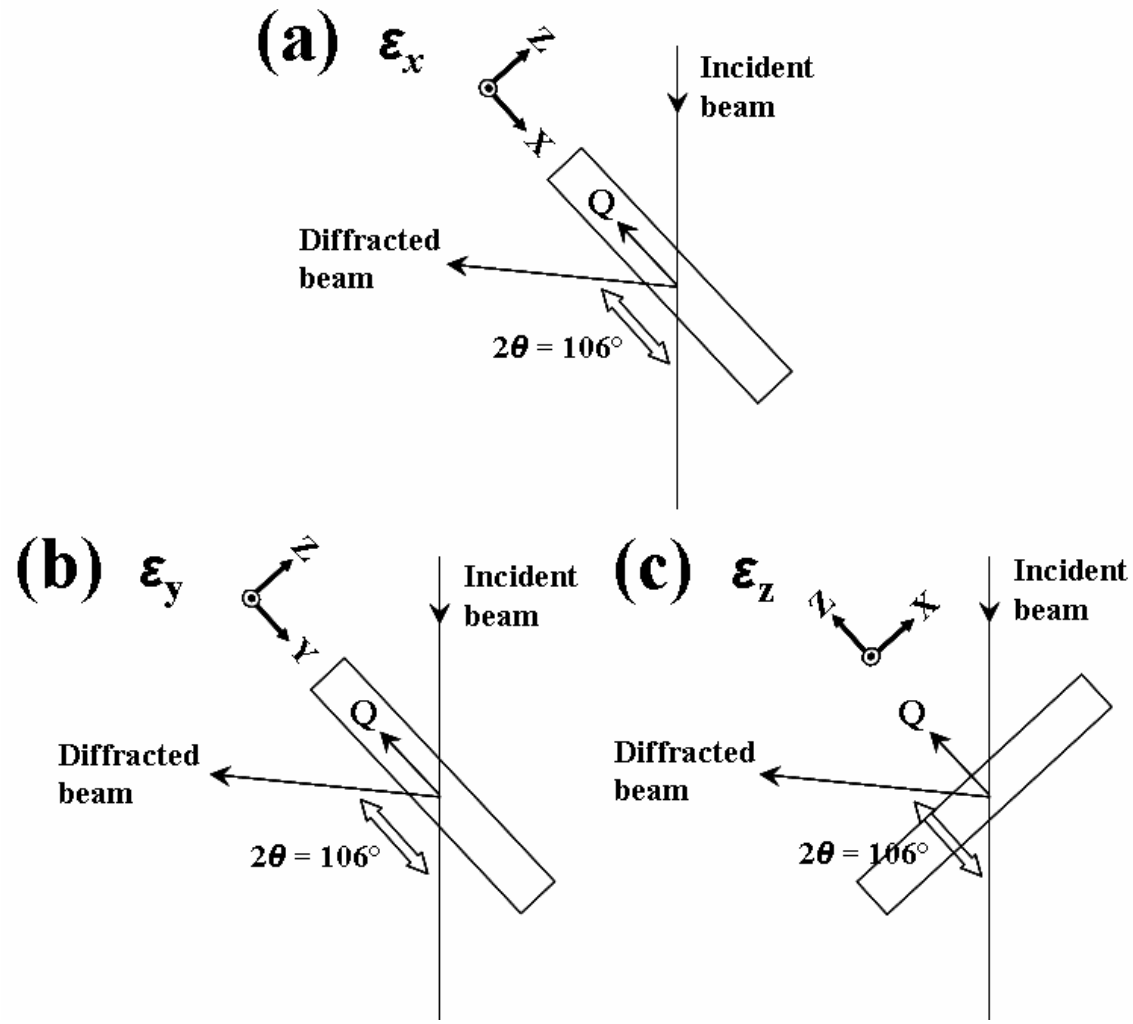

Figure 6.3: Schematic of diffraction geometry showing the scattering vector (Q) parallel to the coordinate (a) *x*: longitudinal (ε_x) strain component; (b) *y*: transverse strain (ε_y) component; and (c) *z*: normal (ε_z) strain component.

from the overload point (= the location corresponds to the crack length of 15.3 mm) that covers from 5 mm behind the crack tip to 21 mm in front of the crack tip. The *d*-spacings along the longitudinal, transverse, and normal directions were determined by the Pseudo-Voigt fitting of the (311) diffraction peak, and, then, the lattice strains were calculated using:

$$\varepsilon = (d - d_0) / d_0 \tag{6.5}$$

where d_0 is the stress-free lattice spacing, which was measured at a corner of each CT specimen. Three residual stress components, σ_i (i = x, y, and z, corresponding to longitudinal, transverse, and normal directions, respectively), were calculated from three strain components using the following equation:

$$\sigma_i = \frac{E}{1+\nu}\left[\varepsilon_i + \frac{\nu}{1-2\nu}\left(\varepsilon_x + \varepsilon_y + \varepsilon_z\right)\right] \tag{6.6}$$

where E is the Young's modulus, and v is the Poisson's ratio.

Moreover, two-dimensional (2-D) strain mapping was performed for the SP 1, 2, and 6, and the measurement positions are shown in Figure 6.4. The (x = 0, y = 0) position corresponds to the crack-tip location for each specimen. The mappings were conducted from –5 to 25 mm along the x direction (parallel to the crack-growth direction), and from –5 to 20 mm along the y direction (perpendicular to the crack-growth direction, i.e., parallel to the applied load, see Figure 6.1), resulting in a 30 mm x 25 mm mapping area. Over 400 locations were measured in each specimen with a finer interval around the crack tip. Only the *d*-spacings along the transverse direction

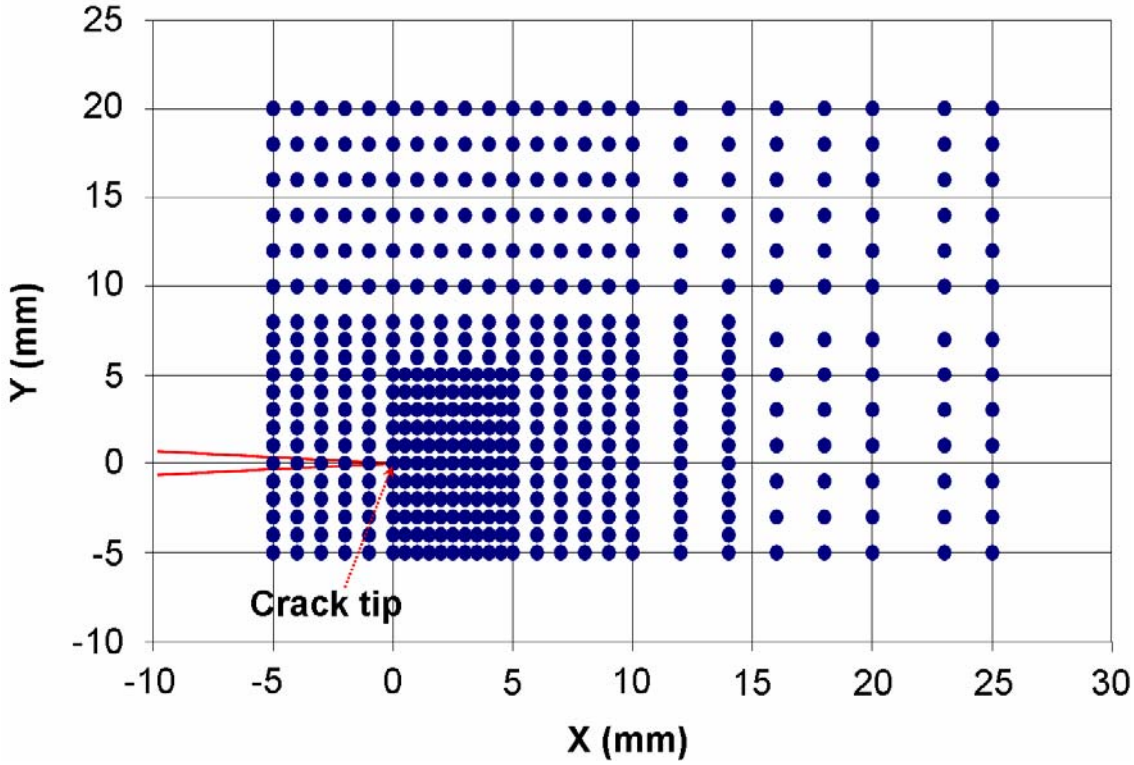

Figure 6.4: Measurement positions for the two-dimensional (2-D) strain mapping (transverse strain component, ε_y, only) of the SP1, 2, and 6.

(parallel to the fatigue-loading direction, Figure 6.1) were measured to obtain the transverse (ε_y) strain component.

6.3 Results

6.3.1 Residual Strain/Stress Evolutions during Crack Propagation

Figure 6.5 shows the transverse residual-strain distributions around the crack tip at six different crack-growth stages marked in Figure 6.2(b) and Table 6.1. Residual-strain profiles were plotted as a function of the distance from the overload point for comparison. Note that the overload point is the same as the crack-tip position of the SP2, which has a crack length of 15.3 mm. The arrows on the top *x*-axis indicate the actual crack-tip locations of each specimen. In Figure 6.5(a), the profile of the SP1 (the as-fatigued specimen without an overload) showed small compressive (negative) strains near its crack-tip position (–5 ~ 0 mm from the overload point) and tensile (positive) residual strains at 0 ~ 8 mm. The SP2 (the overloaded specimen) revealed large compressive strains with a maximum of about –910 με (microstrain, 10^{-6}) near its crack tip and tensile strains were measured at 4 ~ 17 mm in front of the crack tip. The SP3 and SP4, fatigue deformed further after the tensile overloading, showed that compressive strains ahead of their respective crack tips were gradually reduced, as compared to that of the SP2. Interestingly, SP5 and SP6 [in Figure 6.5(b)] exhibited significantly distinct strain profiles with a wider double-valley shape. It was found that the first compressive minimum was at about 2.4 mm, and the second one was at approximately 4.3 mm from the overload point.

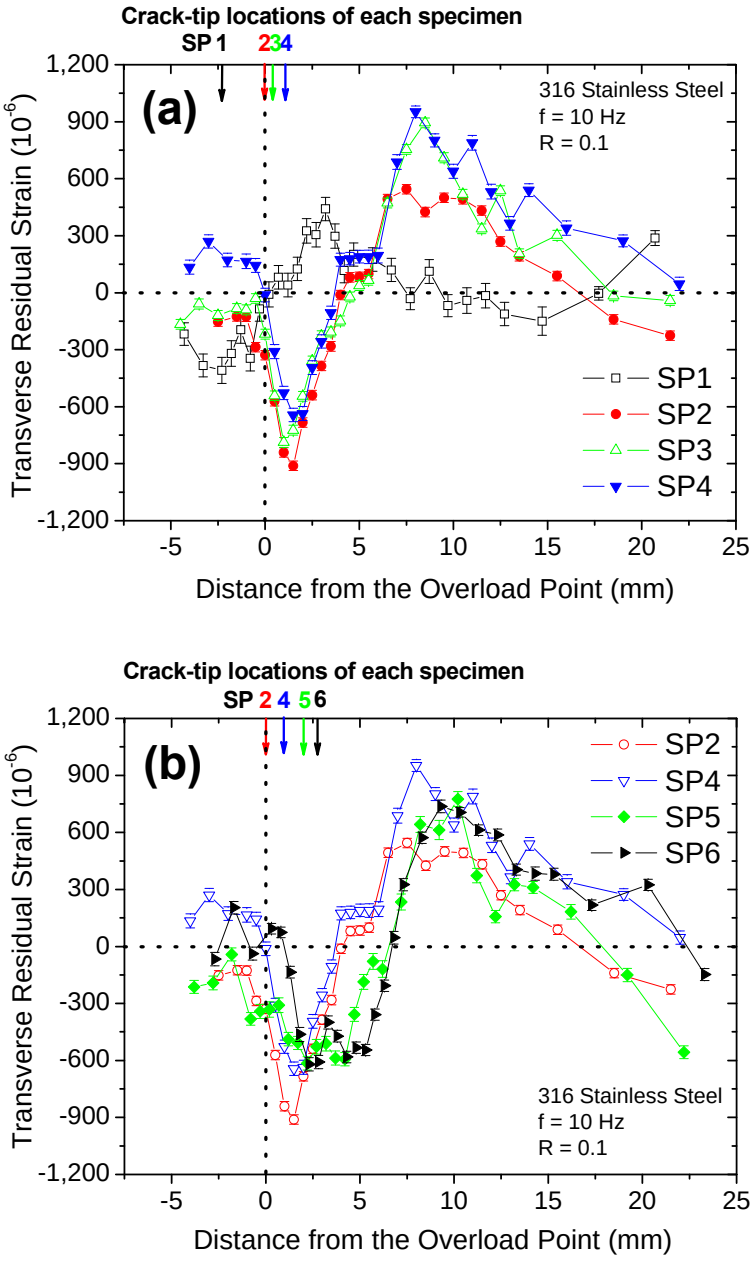

Figure 6.5: Transverse residual-strain profiles for (a) SP1, SP2, SP3, and SP4; (b) SP2, SP4, SP5, and SP6 measured along the crack-growth direction (x).

Figure 6.6 shows the residual-strain profiles along the longitudinal, transverse, and normal directions for the SP2. Residual strains were measured as a function of the distance from the overload point, which is essentially the same as the crack-tip position for the case of SP2. The strains along the normal direction reached a maximum at the crack tip and minimum at about 7 mm from the crack tip, which were approximately opposite to those along the transverse direction. The strains along the longitudinal direction exhibited small compressive strains in the vicinity of the crack tip (1 ~ 7 mm).

Residual stresses were calculated from three principal residual-strain components using Equation 6.6. Transverse residual-stress distributions for the SP1, SP2, SP4, and SP6 are presented in Figure 6.7. The SP1 subjected only to fatigue deformation showed compressive residual stresses at about –4 ~ 0 mm from the overload point (–2 ~ 2 mm from the crack tip). The stress profile of the SP2, which experienced the overload, exhibited a large compressive stress zone (with a maximum of –230 MPa) at about –3 ~ 5 mm from the overload point and tensile stresses from 5 to 17 mm [Figure 6.7(a)]. For the SP4, fatigue deformed further after the overload, it was found that compressive stresses became somewhat smaller than those of the SP2 [Figure 6.7(b)]. The stress profile of the SP4 showed the minimum compressive stresss of –200 MPa at about 2 mm from the overload point and a smaller distinct second valley (compressive stress of –40 MPa) at approximately 6 mm. The stress profile of the SP6 was similar to that of the SP4, indicating two compressive troughs near its crack tip [Figure 6.7(c)]. The first trough of –135 MPa was observed at about 2.8 mm from the overload point (0.1 mm from its crack tip), and a second trough of –190 MPa appeared

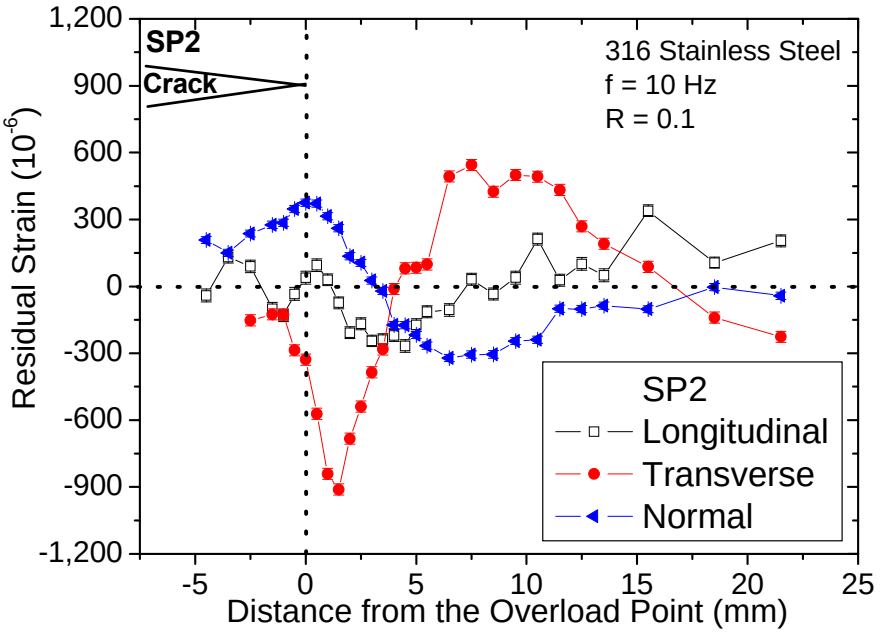

Figure 6.6: Longitudinal, transverse, and normal residual-strain profiles for the SP2 measured along the crack-growth direction (x).

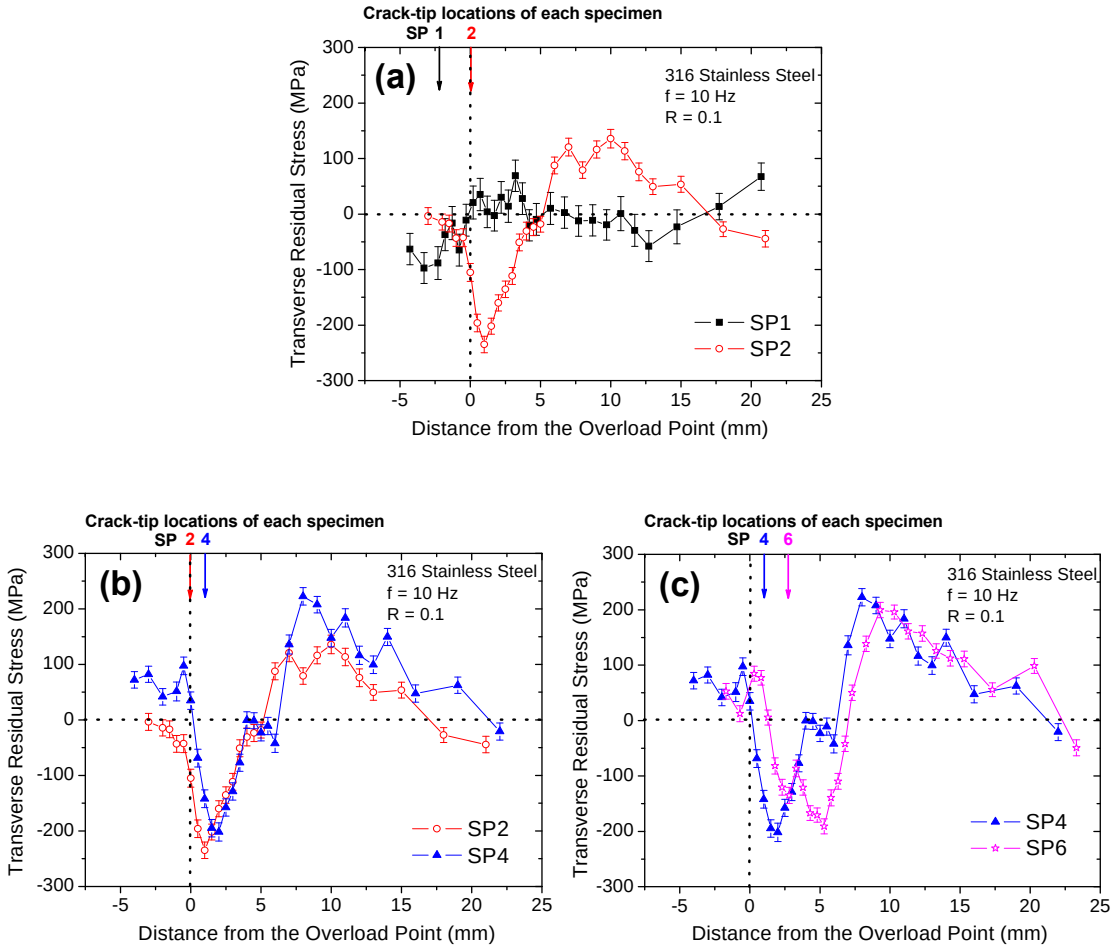

Figure 6.7: Transverse residual-stress distributions as a function of the distance from the overload point for (a) SP1 and SP2; (b) SP2 and SP4; and (c) SP4 and SP6.

at approximately 5.3 mm (2.6 mm from its crack tip). The tensile stresses exhibited from 7 to 22 mm.

6.3.2 Two-Dimensional (2-D) Strain Contours

Figures 6.8(a), (b), and (c) show the transverse-strain contour maps for the SP1, SP2, and SP6, respectively. The actual crack-tip positions for each sample were indicated in the figure. In the contour map of the SP1, a compressive strain region (x = –5 ~ 0 mm, y = –5 ~ 20 mm) was observed around the crack tip (x = –2.3 mm, y = 0 mm). The maximum compressive strain of –480 με was measured at (x = –2.8 mm, y = 0 mm). As the distance from the crack tip increases along the y direction, the compressive strains formed near the crack tip are gradually reduced. It is noted that the sharp strain gradient was found near x = 0. As the distance from the crack tip increases along y = 0 (the x direction), the residual strain values change from compressive (x = –2.3 ~ 0 mm) to tensile (x > 0) strains. The maximum tensile strain of about 345 με exhibited at (x = 3.7 mm, y = 0 mm). At x > 3.7 mm, tensile residual strains decreased gradually. For the SP2 (overloaded), a relatively large compressive zone was examined near the crack tip, as compared to that of the SP1. The maximum compressive strain reached –790 με at (x = 1 mm, y = 0 mm) and the maximum tensile strain of 510 με was measured at (x = 8, y = 0).

Overall, the compressive-strain zone shown in the SP2 was much larger than that of the SP1, while the size of tensile-strain zone was comparable between two specimens. For the SP6 (further fatigue tested after the tensile overloading), it was

Figure 6.8: Two-dimensional contours of transverse residual-strain (ε_y) distributions for (a) SP1, (b) SP2, and (c) SP6.

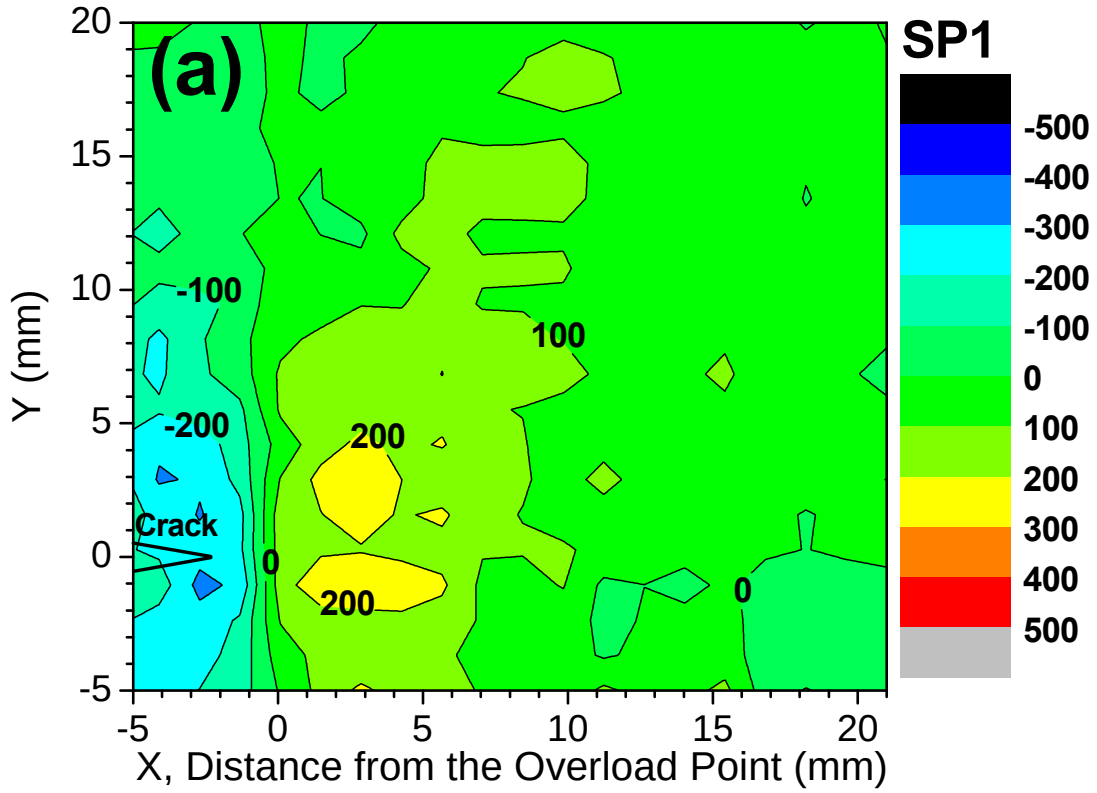
(a)
SP1
-500
-400
-300
-200
-100
0
100
200
300
400
500
-100
100
-200
200
Crack
0
200
0
Y (mm)
X, Distance from the Overload Point (mm)
20
15
10
5
0
-5
-5
0
5
10
15
20

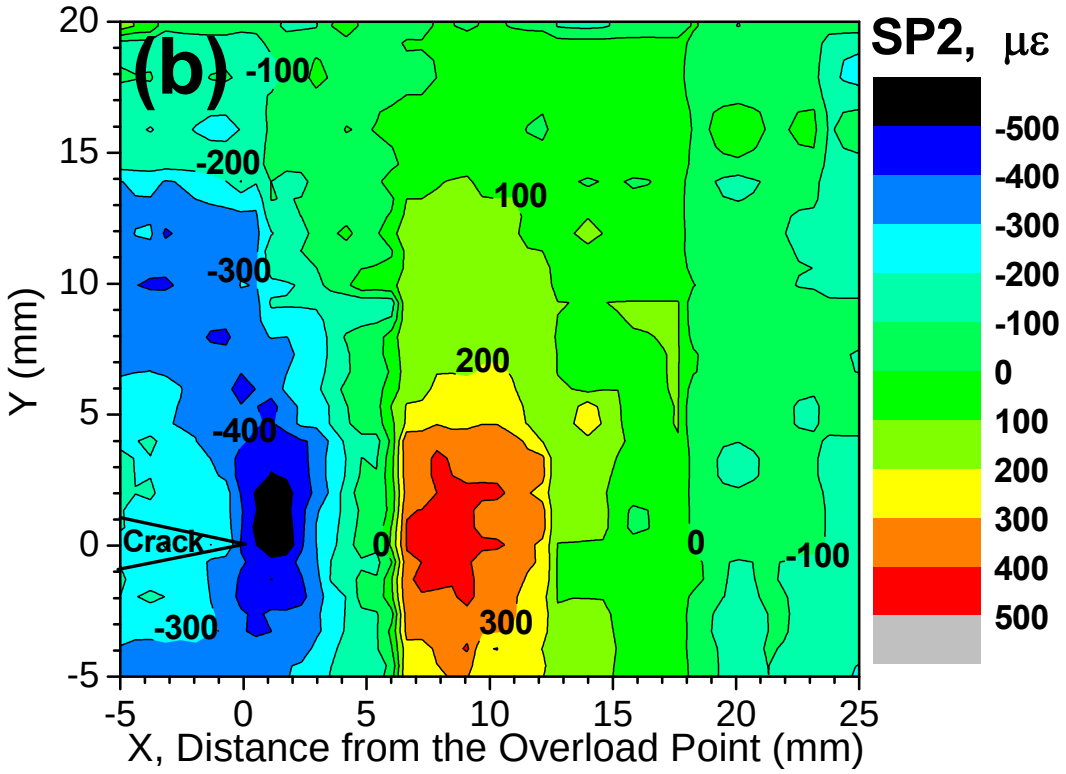

Figure 6.8: Continued.

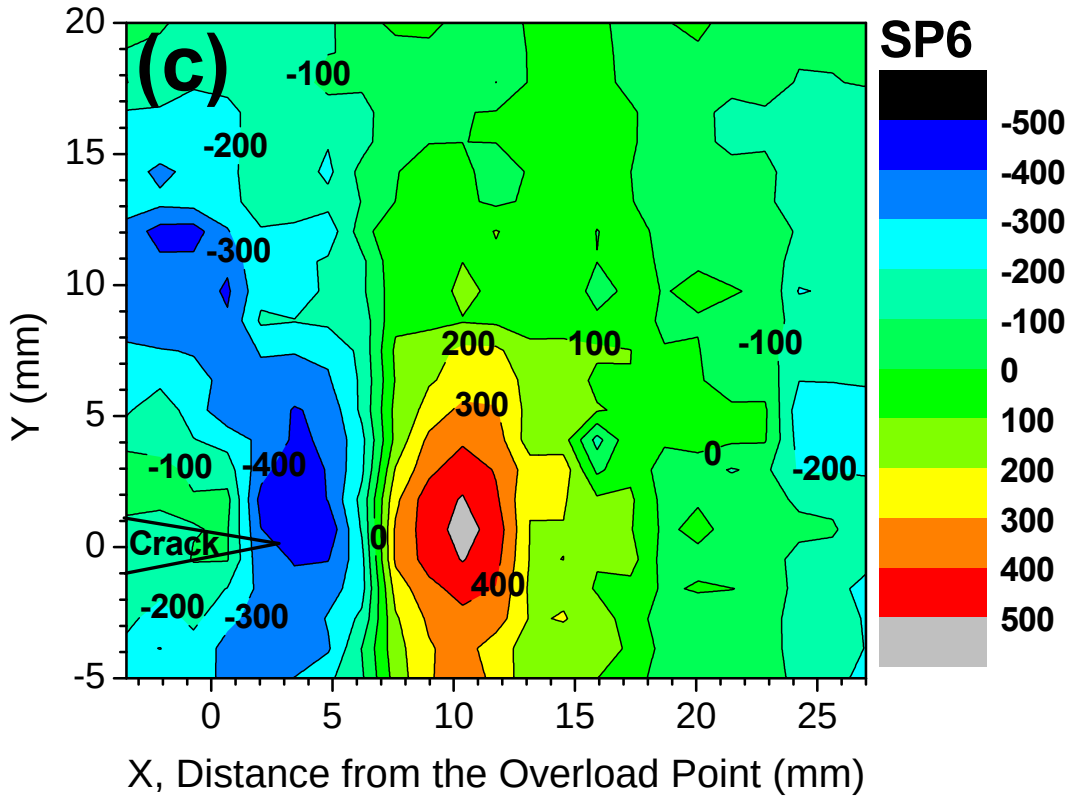

Figure 6.8: Continued.

found that compressive residual strains near the crack tip became relaxed, and somewhat smaller compressive residual strains were measured, as compared to those of the SP2. Two compressive troughs [similar to those shown in Figures 6.5(b) and 6.7(c)] were also observed near its crack tip in 2-D mapping. The first trough was examined at about 2.8 mm from the overload point (0.1 mm from its crack tip), and a second trough was observed at approximately 4.9 mm (2.2 mm from its crack tip). The magnitude of both troughs was about –500 με. The residual strain changed from compressive to tensile values at about 7 mm, and the tensile strain with a maxium of 590 με was observed from 7 to 18 mm. In summary, all 2-D strain contours for three specimens revealed a symmetric deformation along $y = 0$, and showed a similar trend with 1-D strain profiles presented in Figure 6.5.

6.4 Discussion

During constant-amplitude fatigue-crack growth, the monotonic-plastic zone generated by loading is compressed by the surrounding elastic regime, as the load is released from K_{max}. This trend gives rise to the compressive residual stress at the crack tip, producing a reverse plastic zone. Dias et al. (1999) reported that the local plastic deformation occurring at the crack tip during fatigue-crack propagation leaves the residual stress and strain in the wake of the fracture surface. In the current study, the as-fatigued specimen (SP1) clearly showed small compressive residual stresses/strains near the crack tip produced by the reverse plastic deformation. When a tensile overload is applied, the overload produces a relatively large plastic deformation in front of the

crack tip, resulting in the large compressive residual-stress value and zone size, as compared to the constant-amplitude fatigue loading (Wheatley et al., 1999; Ramos et al., 2003; Sun et al., 2005). Figures 6.7 and 6.8 provide the direct experimental evidence of the large compressive residual stress/strain zone near the crack tip (–3 ~ 5 mm from the overload point) caused by the application of the overload. In addition, the current neutron-diffraction measurements (Figures 6.5 and 6.7) showed that the compressive residual stresses/strains are developed near the fatigue-crack tip, and the tensile stresses/strains are observed away in front of the crack tip. The strain distributions in the current study are consistent with those suggested by Saxena (1998). He suggested that the compressive stress near the tip decays gradually outside the reversed plastic zone, and a residual-tensile-stress field is established in the remainder of the uncracked ligament to maintain an equilibrium.

The residual stress/strain distributions in the vicinity of the crack tip can be explained by the interaction between the overload-induced plastic zone and subsequent fatigue-induced plastic zone. To understand the evolution of residual strains in the perturbed plastic zone, the residual-strain profiles for the SP2, SP4, and SP6 were plotted as a function of the distance from the overload point with a schematic of the plastic-zone size in front of the crack tip (Figure 6.9). The application of the overload gives rise to a large plastic deformation in front of the crack tip, resulting in the large compressive residual strain near the crack tip, as shown in Figure 6.9. As previously reported by Rice (1967), the residual-stress distributions near the fatigue-crack tip are influenced by the monotonic plastic-zone size and cyclic plastic-zone size occurring

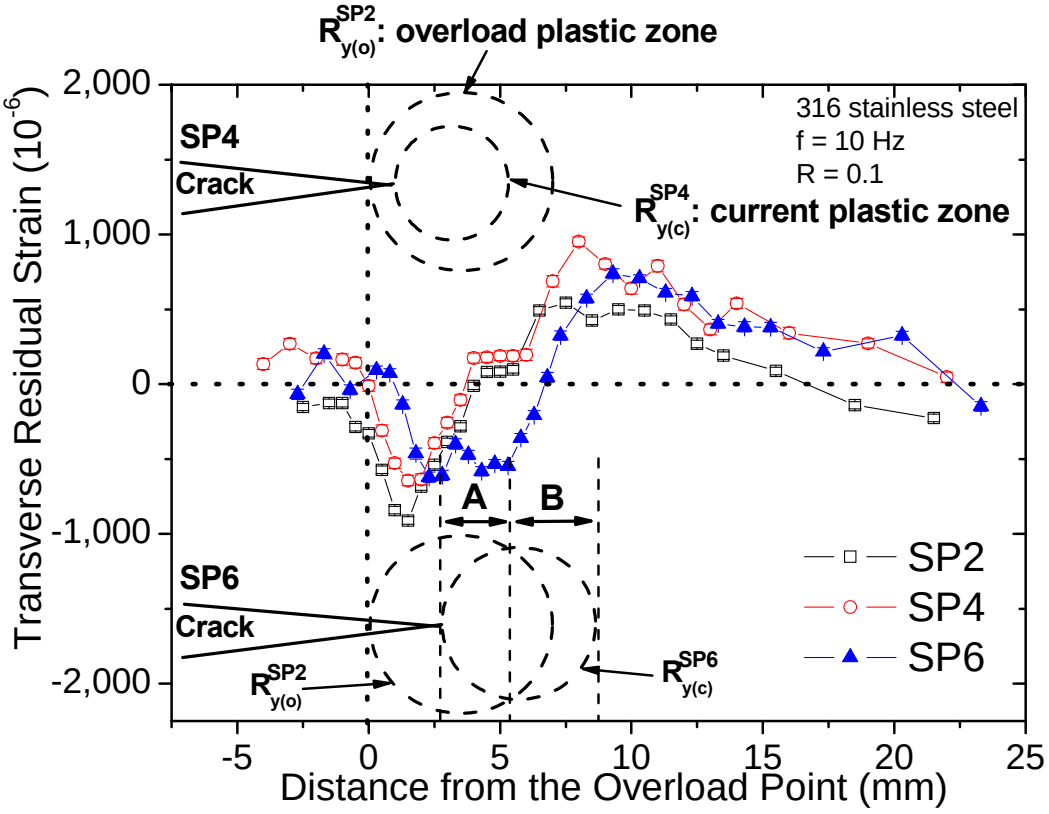

Figure 6.9: Relationship between the plastic-zone size and residual-strain distribution around a fatigue-crack tip within the perturbed plastic zone after the tensile overloading.

during cyclic loading. Likewise, the overload-induced plastic-zone size of about 7 mm (an approximately point at which the maximum tensile strain is observed) was estimated from the residual-strain profiles around the crack tip. The overload plastic-zone size was somewhat larger than the thickness (6.35 mm) of the CT specimen. Using the estimated plastic-zone size and Equation 6.3, the parameter, β, related to the stress state was determined with a value of 1.5, indicating that the current stress state existed between the plane-stress ($\beta = 1$) and plane-strain ($\beta = 3$) conditions.

The crack of SP4 increased 1 mm from the subsequent fatigue loading after the tensile overloading, and the plastic-zone size was found to be 4.3 mm with $\beta = 1.5$. The current plastic zone began to move through the existing large plastic zone created by the tensile overloading, but still stayed within the overload plastic zone. It was found that the residual-strain profile of the SP4 was very similar to that of the SP2 (Figure 6.9). More specifically, the residual strain of the SP4 is still under compression but had a reduced extent, as compared to that of the SP2. Figure 6.7 also showed a reduced residual stress for the SP4, compared to that of the SP2. Almer et al. (1998) reported that the redistribution of the residual stress occurs during crack growth due to the plastic deformation generated by the crack tip. If the current plastic zone is within the overload plastic zone, the redistribution of the residual strain/stress is not significant, because there is no considerably additional plastic deformation. Thus, the strain profiles for the SP4 and likewise SP3 will be similar to those formed by the introduction of the overload (SP2).

The SP6 with a longer crack length (about 1.7 mm longer than the SP4 and 2.7 mm away from the overload point) exhibits quite different strain profiles with a wider double-valley shape, which is also found in Figure 6.7. The estimated current plastic zone for the SP6 was about 5.9 mm, as similarly measured from the residual-strain profiles around the crack tip for the SP2, resulting in $\beta = 1.3$. It means that a part of the current plastic zone already propagated out of the overload-induced plastic zone, and the stress state became a more plane-stress condition, as exhibited in Figure 6.9. These double peaks in the residual-strain profile show clear evidence that the current fatigue-induced plastic zone grew out of the overload-induced plastic zone. The first small increment of the residual strain in the regime A (Figure 6.9) is due to the dominant influence of the overload-induced large compressive strain field, and the second small reduction of the residual strain results from the combined effect between the overload-induced existing strain field and the current fatigue-induced newly-developed strain field. On the other hand, the gradual increment of the residual strain in the regime B (Figure 6.9) is caused by the dominant effect of the emerging current plastic zone out of the overload plastic zone.

In summary, the strain distributions for the SP6 indicate that the fatigue-induced plastic zone grows out of the large overload-induced plastic zone, making the residual strain within the overload plastic zone more relaxed, and the fatigue-induced deformation begins to dominate the residual-strain distribution near the crack tip. Therefore, the crack-growth rate will be recovered to the pre-overload slope of the da/dN versus ΔK curve, as shown in Figure 6.2.

6.5 Conclusions

Residual stresses and strains in the overload-induced perturbed plastic zone were studied to help understand the crack-growth retardation phenomena after a single tensile overload. One-dimensional and two-dimensional maps of the bulk-averaged residual strains around a crack tip in a 316 stainless steel were performed using neutron-diffraction measurements. The main results are summarized as follows:

(1) After the application of the tensile overload during fatigue-crack growth, the large crack-growth retardation was observed. The crack-growth rate instantly decreased down to a certain minimum point, and, then, the propagation rate gradually increased until it is recovered to the pre-overload slope.

(2) One-dimensional stress/strain and two-dimensional strain-mapping results clearly show that a tensile overload significantly increases both the size and magnitude of the compressive residual stress/strain fields near the crack tip.

(3) When the crack-growth rate decreased from the SP2 (right after tensile overloading) to SP4 (an approximately minimum point in the crack-growth rate within the retardation period), it was found that the current plastic zone stayed within the overload-induced plastic zone, resulting in a gradual reduction in the magnitude of the compressive residual stresses/strains.

(4) As the subsequent fatigue-induced plastic zone propagates beyond the overload-induced plastic zone (SP5 and SP6), the residual strain/stress profiles showed a wider double-trough shape, indicating that the current plastic zone grows out of the large overload-induced plastic zone. The double peaks are due to the

combined effect between the overload-induced existing strain field and the current fatigue-induced newly-developed strain field.

The current results clearly showed the interactions between the overload-induced large plastic zone and subsequent fatigue-induced developing plastic zone, and their influences on the evolution of residual-strain distribution around a growing crack tip through an overload-induced retardation period during fatigue-crack growth.

Chapter 7

Overload-Induced Transient Crack-Growth Micromechanism

7.1 Introduction

To predict quantitatively the load-interaction effect under variable-amplitude loading is highly complicate. As the simplest case, the effects of a single tensile overload have been extensively studied since its discovery in the 1960s, because this sort of loading condition gives rise to the beneficial effects on the improvement in the fatigue lifetime (Gan & Weertman, 1981; Shin & Hsu, 1993; Dougherty et al., 1997; Borrego et al., 2003; Singh et al., 2006). More specifically, after a single tensile overload is applied, there is an instantaneous acceleration of the crack-growth rate, followed by a large retardation period, i.e., delay cycles, which can increase the fatigue lifetime significantly. A number of possible mechanisms have been proposed to account for the crack-growth-retardation phenomena, which include the plasticity-induced crack closure (Elber, 1971), crack-tip blunting (Christensen, 1959), compressive residual stress (Schijve, 1960), crack-tip strain hardening (Jones, 1973), and crack branching (Suresh, 1983). Among them, the plasticity-induced crack-closure concept suggested by Elber has been supported by many investigations. Elber introduced the effective-stress-intensity-factor range as a fatigue-crack-tip-driving force, emphasizing the significance of a crack-closure phenomenon in the wake of a crack. However, other investigators

have found that the plasticity-induced crack closure fails to account for fully the observed post-overload transient growth behavior. For instance, Sadananda et al. (1999) demonstrated that the perturbation of the stresses ahead of the crack tip is the major cause for the overload retardation, not due to the crack closure behind the crack tip, and suggested a new "unified approach" in which the maximum stress intensity factor, $K_{max,}$ and the stress-intensity-factor range, ΔK (= $K_{max} - K_{min}$), are considered as the two parameters that provide the two driving forces required for fatigue-crack growth. Louat et al. (1993) pointed out that plasticity originating from the crack tip does not induce the crack closure, and Vasudevan et al. (1992) also suggested that the crack closure by the crack-tip plasticity does not occur without an oxide or an asperity. In summary, the exact retardation micromechanism, fatigue-crack-tip-driving force, and the crack-closure phenomenon in a fatigue wake still remain questionable in the literature. It might be due to an experimental lack to measure quantitative strain/stress fields near a fatigue-crack tip under applied loads and to observe *in-situ* crack-tip deformation and failure phenomena during real-time fatigue experiments.

A crack-closure approach has played an important role in explaining many load-interaction effects on the fatigue-crack-growth behavior under variable-amplitude loading (Schijve, 1988). The exact determination of crack opening and closing loads (or stresses) is important to predict the accurate crack-tip-driving force. Most of the experimental crack-closure measurements are based on the analysis of the specimen compliance, i.e., displacement/load (Elber, 1971; Liaw et al., 1982; Brahma et al., 1989; Yisheng & Schijve, 1995). An alternative method to measure the crack closure is to use

the direct-current-potential-drop (DCPD) technique. When a constant current is passed through the test specimen, the crack-mouth potential is measured. The higher potential means the longer crack length due to an increased resistivity of the material. If a crack closes and yields an electric contact between the fracture surfaces, a crack-closing (or opening) point should be determined from the curve of the applied load vs. potential during a single fatigue cycle. Recently, Andersson et al. (2006) investigated the possibility of using DCPD for crack-closure measurements by comparing closure results from *in-situ* observations of crack closure using a scanning-electron microscope (SEM). They have found that the results of crack-closure measurements made by the potential drop were similar to those determined from in-situ SEM observations, and concluded that a crack-opening point is reliable if the crack closure is detected by potential measurements.

A variety of nondestructive-diffraction techniques, e.g., the high-energy synchrotron X-ray diffraction and tomography (Haase et al., 1998; Withers et al., 2006; Steuwer et al., 2006; Khor et al., 2006; Croft et al., 2007; Daymond et al., 2007; Robertson et al., 2007; Hung et al., 2009), and neutron diffraction (Smith et al., 1995; Sun et al., 2005; Lee et al., 2008; Barabash et al., 2008; Lee et al., 2009), have been employed to study the imaging of the crack, texture, crack-tip strain/stress fields, plastic-zone size, crystallographic lattice distortion, and dislocation-density distribution in the vicinity of the crack tip. Among them, neutron diffraction is well suited for the determination of the bulk-averaged strain, stress, and texture on even larger length scales than synchrotron X-ray diffraction, owing to the high penetration capabilities of

neutrons. Furthermore, a neutron-diffraction technique provides the spatially-resolved *in-situ* internal stresses/strains mappings around the crack tip under applied loads, allowing us to examine the stress distributions at various locations from the crack tip as a function of the applied load.

In summary, direct measurements of the internal strains/stresses near the crack tip and precise observation of the crack-tip deformation characteristics under applied loads will be an important matter on solving the above arguments shown in the literature. In this aspect, the neutron-diffraction and electric-potential techniques will play a significant role in (1) probing the crack-tip deformation and failure phenomena *in situ* under an applied load; (2) investigating the crack-growth mechanism of the cyclic deformation subjected to a tensile overload; (3) validating the effective-stress-intensity-factor range based on the crack-closure approach as a fatigue-crack-tip-driving force; and (4) establishing a quantitative relationship between the crack-tip-driving force and crack-propagation behavior. More specifically, this work will provide the effects of residual stress, crack closure, and crack-tip blunting on the internal-strain evolution and stress distribution under applied loads; and their influences on the crack-opening load, fatigue-crack-tip-driving force, and the crack-growth behavior. Moreover, the mechanisms concerning the overload effects are suggested, and bulk-averaged crack-opening loads between the electric potential and in-situ neutron-diffraction technique are compared.

7.2 Experimental Details

7.2.1 Fatigue-Crack-Growth Experiments

The fatigue-crack-growth experiments were performed on a compact-tension (CT) specimen of HASTELLOY C-2000 alloy (56%Ni-23%Cr-16%Mo, in weight percent) using a computer-controlled Material Test System (MTS) servohydraulic machine. This material has a single-phase face-centered-cubic (FCC) structure, yield strength of 393 MPa, ultimate tensile strength of 731 MPa, Young's modulus of 207 GPa, no preferred texture, and the average grain size of about 90 μm. The CT specimen geometry was prepared according to the American Society for Testing and Materials (ASTM) Standards E647-99 (ASTM, 2000). Before the crack-growth tests, the CT specimens were precracked to approximately 1.27 mm. A constant-load-range-control (ΔP) mode was used for the crack-growth tests with a frequency of 10 Hz and a load ratio, R, of 0.01 ($R = P_{\min} / P_{\max,}$ $P_{\min}$ and $P_{\max}$ are the applied minimum and maximum loads, respectively). The crack length was measured by a direct-current-potential drop (DCPD) method (Johnson, 1965; Schwalbe & Hellman, 1981). The stress-intensity factor, K, was obtained using the following equation (ASTM, 2000):

$$K = \frac{P(2+\alpha)}{B\sqrt{W}(1-\alpha)^{3/2}}(0.886 + 4.64\alpha - 13.32\alpha^2 + 14.72\alpha^3 - 5.6\alpha^4) \qquad (7.1)$$

where P = applied load, B = thickness, $\alpha = a/W$, a = crack length, and W = width for a CT specimen.

When the crack length reached 20 mm during a constant-amplitude fatigue-crack growth (i.e., P_{max} = 7,250 N, P_{min} = 72.5 N), a single tensile overload (i.e., $P_{overload}$ = 10,875 N, which is 150% of P_{max}) was introduced, and, then, the constant-amplitude fatigue-crack-growth test was resumed to monitor the crack-propagation behavior. Figure 1 shows the crack-growth rate (da/dN) vs. the stress-intensity-factor range, ΔK (= $K_{max} - K_{min}$, K_{max} and K_{min} are the maximum and minimum stress-intensity factors, respectively). The crack-growth rate, da/dN, was obtained by a seven-point incremental polynomial technique (ASTM, 2000). After an application of a tensile overload, there was an initial acceleration of the crack-growth rate followed by the large crack-growth-retardation period. A total of eleven different crack-growth stages were chosen to investigate such transient crack-growth behaviors following a single tensile overload. Experimental details are summarized in Table 7.1. The stage 1 (ΔK = 32.41 MPa.m$^{1/2}$) was subjected to only cyclic deformation. When a fatigue crack reached at ΔK = 35.90 MPa.m$^{1/2}$, three fatigue cycles were continuously introduced: 2a – fatigue cycle right before overloading; 2b – overloading cycle; 2c – fatigue cycle right after overloading. After a single tensile overload was imposed, an initial acceleration of the crack-growth rate was observed, and, then, the crack-growth rate sharply decreased. The stages 3, 4, and 5 was prepared during a sharp reduction of the crack-growth rate when a fatigue crack reached at ΔK = 36.26, 36.52, and 37.04 MPa.m$^{1/2}$, respectively. After the minimum crack-growth rate (stage 5) was observed, the crack-growth rate gradually increased. The stages 6 and 7 were prepared during this increased period at ΔK = 38.64 and 40.56 MPa.m$^{1/2}$, respectively.

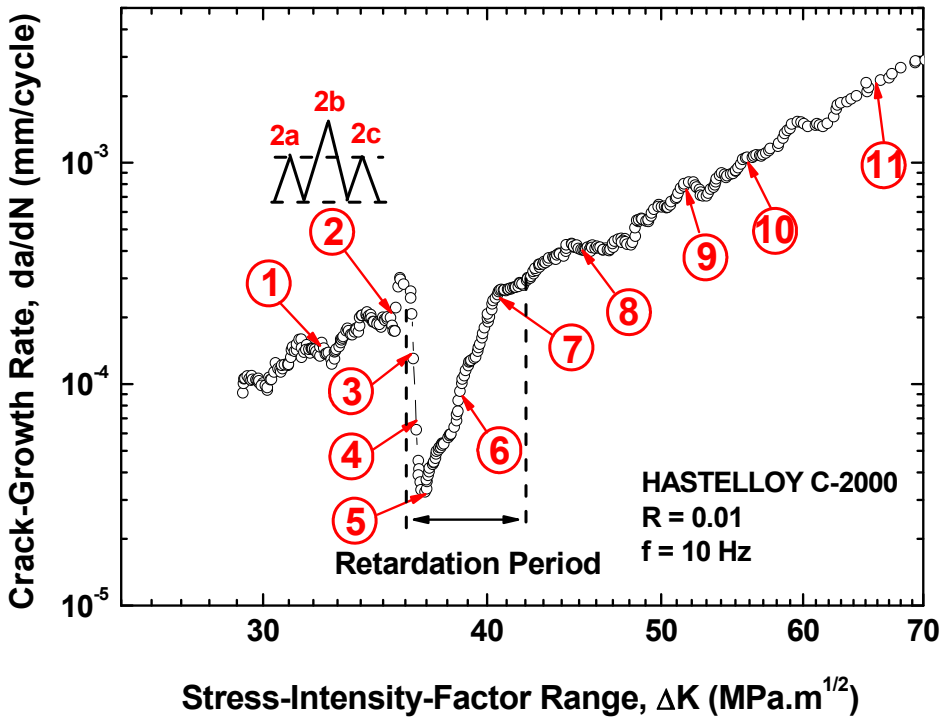

Figure 7.1: The change in the crack-growth rates (d*a*/d*N*) as a function of the stress intensity-factor range (ΔK).

Table 7.1: Details on eleven crack-growth stages marked in Fig. 7.1 (F: fatigue, OL: overload, EP: electric potential, ND-RS: neutron-diffraction residual stress, ND-IL: neutron-diffraction *in-situ* loading). Each experiment were carried out at the marked stage with "O".

Growth stages	Crack length (mm)	ΔK (MPa.m$^{1/2}$)	Description	Various measurements		
				EP	ND – RS	ND – IL
1	18	32.41	F	O	–	–
2	20	35.90	2a (right before OL): F	O	O	O
			2b (during OL): F+OL	O	–	–
			2c (right after OL): F+OL+F	O	O	O
3	20.19	36.26	F+OL+F	O	–	–
4	20.33	36.52		O	–	–
5	20.6	37.04		O	O	O
6	21.4	38.64		O	O	O
7	22.3	40.56		O	O	O
8	24.2	45.12		O	–	–
9	26.5	51.86		O	–	O
10	27.6	55.70		O	–	–
11	30	66.02		O	–	–

Finally, the crack-growth rate was recovered following the pre-overload slope in the da/dN vs. ΔK curve, and the crack-growth rate increased linearly with increasing the ΔK. The stages 8–11 were prepared in this linear region at ΔK = 45.12, 51.86, 55.70, and 66.02 MPa.m$^{1/2}$, respectively.

Three different experimental approaches (see Table 7.1) were employed in this study: 1) Electric Potential (EP); 2) Neutron-Diffraction Residual-Stress mapping (ND-RS); and 3) Neutron-Diffraction In-situ Loading (ND-IL). Note that respective measurements have been performed at the crack-growth stages with marked circle (O). For example, only EP experiment was conducted at the stage 1 and all three measurements (i.e., EP, ND-RS, and ND-IL) were carried out at the stage 5.

7.2.2 Electric-Potential Experiments

In terms of an electric-potential method, the measured dc electric potential at any crack length was normalized and converted into the corresponding crack length using Johnson's equation (Johnson, 1965),

$$a/W = 2/\pi\left[\frac{\pi}{2} - \arctan\left(\frac{Z}{\sqrt{\left(1-Z^2\right)}}\right)\right] \tag{7.2}$$

where

$$Z = \frac{e^{\left(\frac{h\pi}{W4}\right)} + e^{-\left(\frac{h\pi}{W4}\right)}}{e^{(U+X)} + e^{-(U+X)}} \tag{7.3}$$

and

$$X = \ln\left[\left(\frac{\left(e^{\left(\frac{h\pi}{W4}\right)} + e^{-\left(\frac{h\pi}{W4}\right)}\right)}{2\cos\left(\frac{A_0}{W}\frac{\pi}{2}\right)}\right) + \sqrt{\left(\frac{\left(e^{\left(\frac{h\pi}{W4}\right)} + e^{-\left(\frac{h\pi}{W4}\right)}\right)}{2\cos\left(\frac{A_0}{W}\frac{\pi}{2}\right)}\right)^2 - 1}\right] \tag{7.4}$$

and

a is the crack length, W is the specimen width, h is the distance between the two points at which the crack-mouth potential is measured, and U (= normalized potential) is defined as follows:

$$U = \frac{PD_{acttempcorrectedave} / PD_{initial}}{PD_{reftempcorrectedave} / PD_{refinitial}} \tag{7.5}$$

PD_{initial} is the thermally corrected potential at some known initial crack length and $PD_{\text{refinitial}}$ is the thermally corrected initial potential of the reference probes.

When the reversing current is applied,

$$PD_{acttempcorrectedave} = \left(PD_{ave+} - PD_{ave-}\right)/2 \tag{7.6}$$

$$PD_{reftempcorrectedave} = \left(PD_{refave+} - PD_{refave-}\right)/2 \tag{7.7}$$

$PD_{\text{ave+}}$ and $PD_{\text{refave+}}$ are the sum of all PD readings from crack-mouth and reference probes, respectively, when the current is in one direction. $PD_{\text{ave–}}$ and $PD_{\text{refave–}}$ are the

sum of all PD readings from crack-mouth and reference probes, respectively, when the current is in the other direction.

Using this method, an understanding of crack-tip deformation and fracture behaviors during a single loading-unloading cycle can be enhanced from the observation of changes in the electric potential. More specifically, this technique enables the investigation of crack-closure phenomenon, as well as the elastic and plastic deformation behaviors at the crack tip under an applied load during a single cycle. In addition, respective crack-opening loads at various crack-growth stages can be determined from the curve of the normalized potential vs. applied load, as shown similarly in the previous work (Clarke & Cassatt, 1977).

In this study, the changes in the electric potential during a single loading-unloading cycle were measured at eleven crack-growth stages (see Fig. 7.1 and Table 7.1) through the da/dN vs. ΔK curve. From the plot of normalized potential vs. applied load, the bulk-averaged crack-opening loads were determined at various stages through the retardation period. Based on the measured crack-opening loads, the stress-intensity factor at the crack-tip opening, K_{op}, was calculated using Equation 7.1. Thus, the effective-stress-intensity-factor range, ΔK_{eff}, was obtained using the following equation,

$$\Delta K_{eff} = K_{max} - K_{op} \tag{7.8}$$

where K_{max} and K_{op} denote the stress-intensity factors at the maximum load and crack opening, respectively. Finally, da/dN vs. ΔK_{eff} was plotted to investigate the applicability of ΔK_{eff} as a fatigue-crack-tip-driving force.

7.2.3 Neutron-Diffraction Experiments

7.2.3.1 Residual-Stress Measurements

The spatially-resolved neutron residual-stress mapping was carried out on L3 spectrometer at Chalk River Laboratories, Canada. Three principal residual-strain components [i.e., longitudinal (ε_x), transverse (ε_y), and normal (ε_z) strains, Figure 7.2(a)] were measured as a function of the position from the crack tip along the crack-growth direction [*x*-direction, Fig. 7.2(b)]. A total of 26 points were measured as a function of the distance from the crack tip. Note that the crack tip identified on the surface of the sample using a scanning-electron microscope was used for this measurement. To provide the required spatial resolution, the scanning intervals of 1 mm from –4 to 0 mm (crack tip), 0.5 mm from 0 to 8 mm where sharp strain gradients are expected, 2 mm from 8 to 16 mm, and 3 mm from 16 to 22 mm were used. The scattering volume was positioned in the middle of the sample thickness for all strain components [Fig. 7.2(b)].

A schematic of a CT specimen and the diffraction geometry is shown in Figs. 7.3(a)-(c). For the longitudinal (ε_x) and transverse (ε_y) strain components [Figs. 7.3(a) and (b), respectively], the wavelength of 1.308499Å and 1.308773Å, respectively, was selected from the Ge115 monochromator. The specimen was aligned 53° (clockwise) from the incident neutron beam and the (311) diffraction pattern was measured in a stationary detector centered on a diffraction angle of $2\theta = 74°$. The longitudinal (ε_x) strain component was measured using 1-mm wide and 2-mm tall (parallel to *y*) incident beam slits, and 1-mm wide diffracted beam slit. The transverse (ε_y) strain component

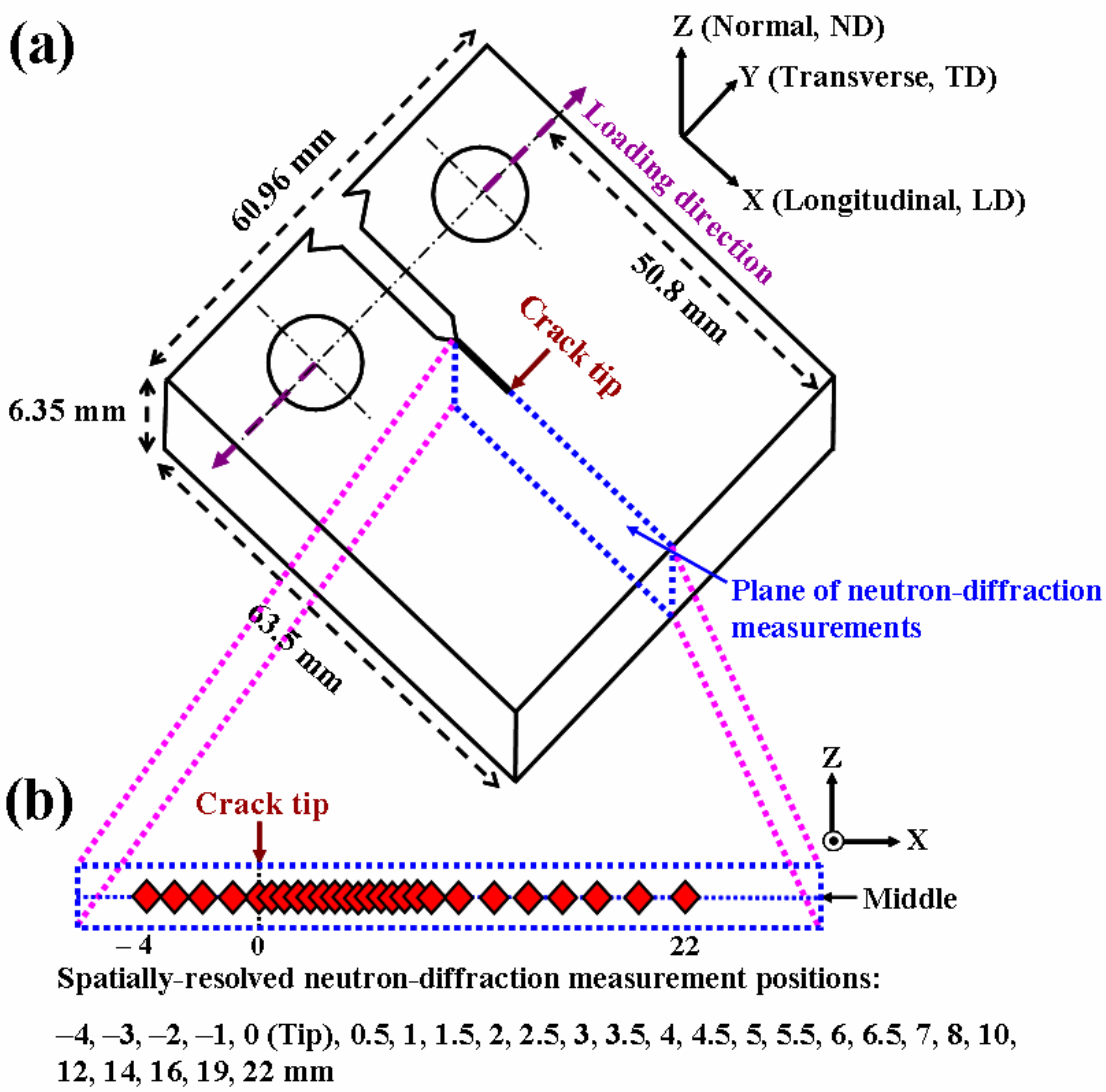

Figure 7.2: Schematic of (a) a Haystelloy C-2000 compact-tension specimen, (b) spatially-resolved neutron-diffraction measurement positions along the direction of the crack propagation (x).

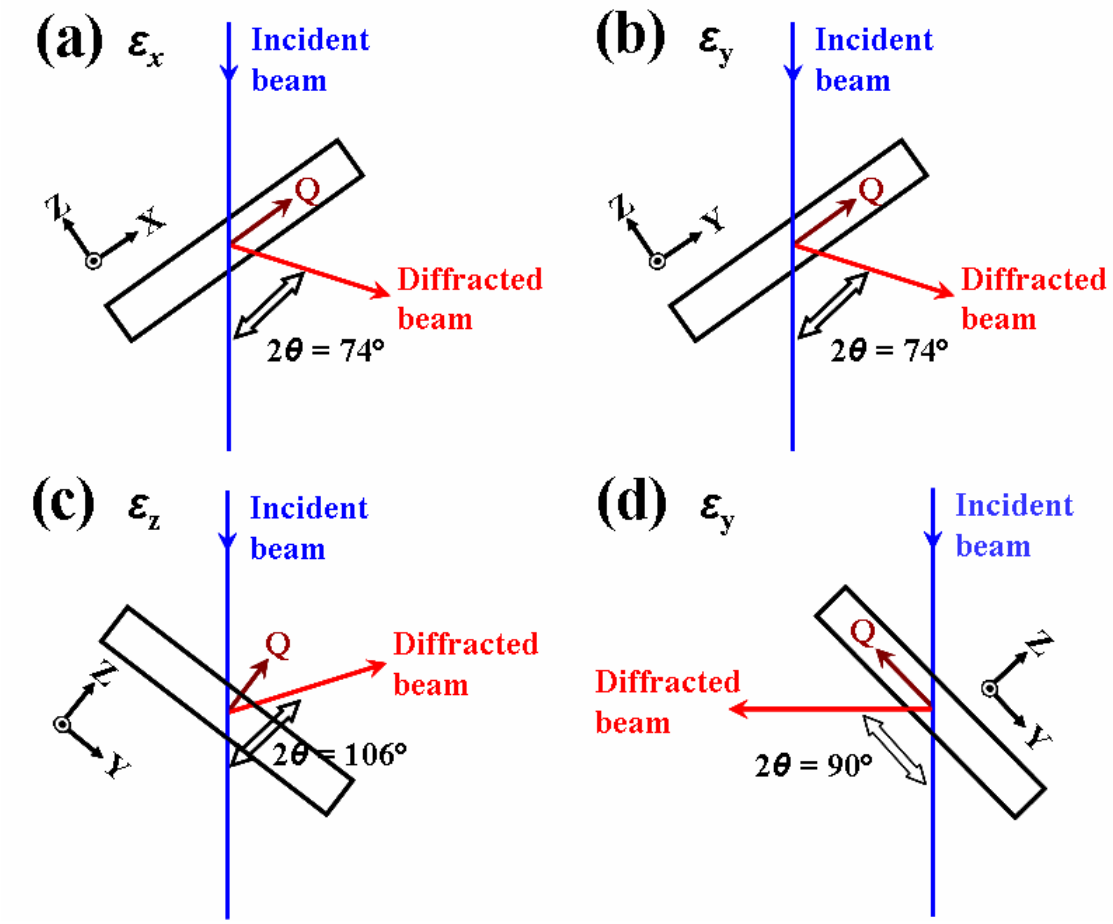

Figure 7.3: Schematic of diffraction geometry for the residual-stress mapping showing the scattering vector (Q) parallel to the coordinate (a) *x*: longitudinal (ε_x) strain component; (b) *y*: transverse strain (ε_y) component; (c) *z*: normal (ε_z) strain component; and (d) for in-situ internal-strain mapping showing the scattering vector (Q) parallel to the coordinate *y*: transverse strain (ε_y) component.

was measured using 2-mm wide and 1-mm tall (parallel to *x*) incident beam slits, and 2-mm wide diffracted beam slit.

For the normal (ε_z) strain component [Fig. 7.3(c)], the wavelength of 1.738462Å was chosen from the Ge115 monochromator. The specimen was aligned 127° (clockwise) from the incident neutron beam and the (311) diffraction pattern was recorded in a stationary detector centered on a diffraction angle of $2\theta = 106°$. Thus, the diffraction vectors were parallel to the normal direction (parallel to *z*) of the specimen. The incident beam was defined by 2-mm wide and 1-mm tall (parallel to *x*) slits, and the diffracted beams were collimated by 2-mm wide slit.

The *d*-spacings along the longitudinal, transverse, and normal directions were determined by the Gaussian fitting of the (311) diffraction peak, and, then, the lattice strains were calculated as follows:

$$\varepsilon = (d\text{-}d_0)/d_0 \tag{7.9}$$

where d_0 is the stress-free reference lattice spacing measured at 10 mm away from the corner of the specimen. Three residual-stress components, σ_i (i = *x, y,* and *z*, corresponding to longitudinal, transverse, and normal directions, respectively), were calculated from three residual-strain components using the following equation:

$$\sigma_i = \frac{E}{1+\nu}\left[\varepsilon_i + \frac{\nu}{1-2\nu}\left(\varepsilon_x + \varepsilon_y + \varepsilon_z\right)\right] \tag{7.10}$$

where E is the Young's modulus and v is the Poisson's ratio. In this study, the transverse residual-stress distributions near the crack tip will be presented at various crack-growth stages (i.e., 2a, 2c, and 5–7, see Table 7.1).

7.2.3.2 Internal-Strain Measurements under Applied Loads

The *in-situ* neutron-strain mapping was conducted on the Neutron Residual Stress mapping Facility (NSRF2) at the High Flux Isotope Reactor of the Oak Ridge National Laboratory. In this study, the investigation of lattice-strain response on the applied load at various locations from the crack tip will be emphasized. The wavelength of 1.536833Å was chosen from the Si422 monochromator. The (311) diffraction peak was recorded in a stationary detector centered on a diffraction angle of $2\theta = 90°$ [see Fig. 7.3(d)]. The specimen was aligned at a 45° from the incident neutron beam [see Fig. 7.3(d)], and, thus, the diffraction vector was parallel to the transverse direction [i.e., parallel to the fatigue-loading direction, Fig. 7.2(a)] of the CT specimen. The incident beam was defined by 2-mm wide and 1-mm tall [x-direction, Fig. 7.2(a)] slits, and the diffracted beams were collimated by 2-mm wide slit, resulting in a 4-mm^3 gauge volume. Only the d-spacings, determined from the Gaussian fitting of the (311) diffraction peak, along the transverse direction were measured to obtain the transverse strain (ε_y) component.

A total of six CT specimens representing various crack-growth stages (i.e., 2a, 2c, 5–7, and 9, see Table 7.1) were prepared to observe the internal-strain evolutions in the vicinity of the crack tip under applied loads. For each specimen, the transverse

elastic-lattice strains were measured as a function of the distance from the crack tip along the crack-propagation direction [x-direction, Fig. 7.2(a)] at varying 13 loading levels from P_{min} to P_{max} (i.e., 0.01, 0.1, 0.15, 0.2, 0.25, 0.3, 0.35, 0.4, 0.45, 0.5, 0.6, 0.8, and 1 P_{max}). To obtain the information of stress distribution in the vicinity of the crack tip under applied loads, several positions from the crack tip were selected. For example, the elastic-lattice strain was plotted as a function of the applied load at a few positions behind the crack tip (e.g., –2 mm and –1 mm) and ahead of the crack tip (e.g., 2 mm and 6 mm), and at the crack tip (0 mm) [see Figs 7.6(a)-(e)]. From the observation of internal-strain evolution at the different locations, bulk-averaged crack-opening loads were determined using an *in-situ* neutron-diffraction technique. These results will be compared to those measured from the electric potential.

7.3 Results

7.3.1. Overload-Induced Fatigue-Crack-Growth Behavior

Figure 7.1 shows the fatigue-crack-growth behavior following a single tensile overload as a function of the stress-intensity-factor range. Before the overload was applied at ΔK = 35.90 MPa.m$^{1/2}$, the fatigue-crack-growth rate increased linearly with increasing ΔK, following the Paris law. After a single tensile overload was introduced, four notable phenomena were observed: (1) an initial short acceleration of the crack-growth rate immediately after an overload, (2) the sharp decrease in the crack-growth rate down to the minimum point, (3) the gradual increase in the crack-growth rate after

passing the minimum point, and (4) the recovery to the pre-overload slope in the crack-growth rate.

7.3.2 Electric-Potential Measurements

Figure 7.4(a) shows the electric-potential changes during a single loading-unloading cycle at the crack-growth stage 2a (a cycle just before overloading), Fig. 7.1. Three distinct linear regions were observed from the plot of the normalized potential vs. applied load. First, as the applied load increases up to 0.25 P_{max}, the electric potential increased linearly. After a transition region was examined at the applied load from 0.25 P_{max} to 0.54 P_{max}, the second linear region was observed as the applied load increases from 0.54 P_{max} to 0.83 P_{max}. In this linear region, the potential was slightly increased with the applied load. The third linear region was examined as a higher load is applied from 0.83 P_{max} to P_{max}. During unloading process, the electric potential was reduced following a reverse step.

Figure 7.4(b) presents the potential change during a single tensile loading-unloading cycle at the stage 2b (an overloading cycle) and stage 5 (a maximum retardation point). As the applied load increases up to $P_{overload}$ (= 1.5 P_{max}, a maximum overloading point, the stage 2b), the potential curve showed three distinct linear region as similarly examined at the stage 2a. However, large normalized potential change of 0.04 was observed as the load was applied from P_{max} to $P_{overload}$. During unloading after an application of the tensile overload, the electric potential revealed the irreversible

`

Figure 7.4: Electric-potential change during a single loading-unloading cycle (a) at the stage 2a, a cycle right before the tensile overloading, (b) at the stages 2b (a cycle during overloading) and 5 (a maximum retardation point); SEM micrographs (c) before, (d) after the overloading, and (e) at the stage 5; and (f) Electric-potential change during a single loading-unloading cycle at various crack-growth stages marked in Fig. 7.1.

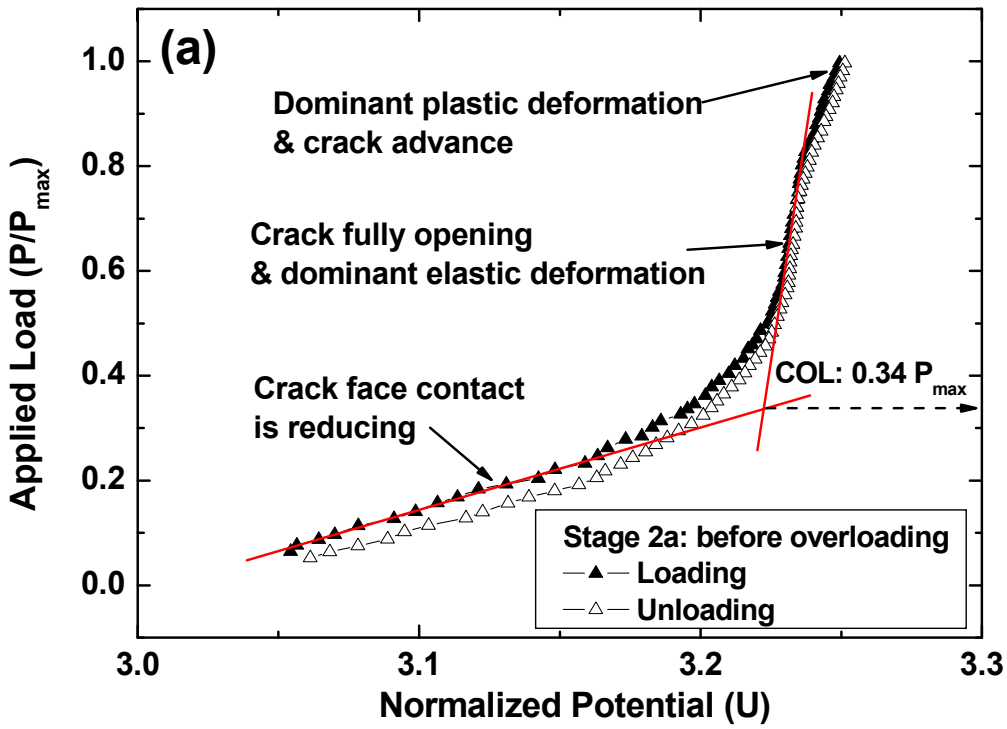
(a)
Dominant plastic deformation
& crack advance
Crack fully opening
& dominant elastic deformation
Crack face contact
is reducing
COL: 0.34 P max
Stage 2a: before overloading
Loading
Unloading
Applied Load (P/P max)
Normalized Potential (U)
1.0
0.8
0.6
0.4
0.2
0.0
3.0
3.1
3.2
3.3

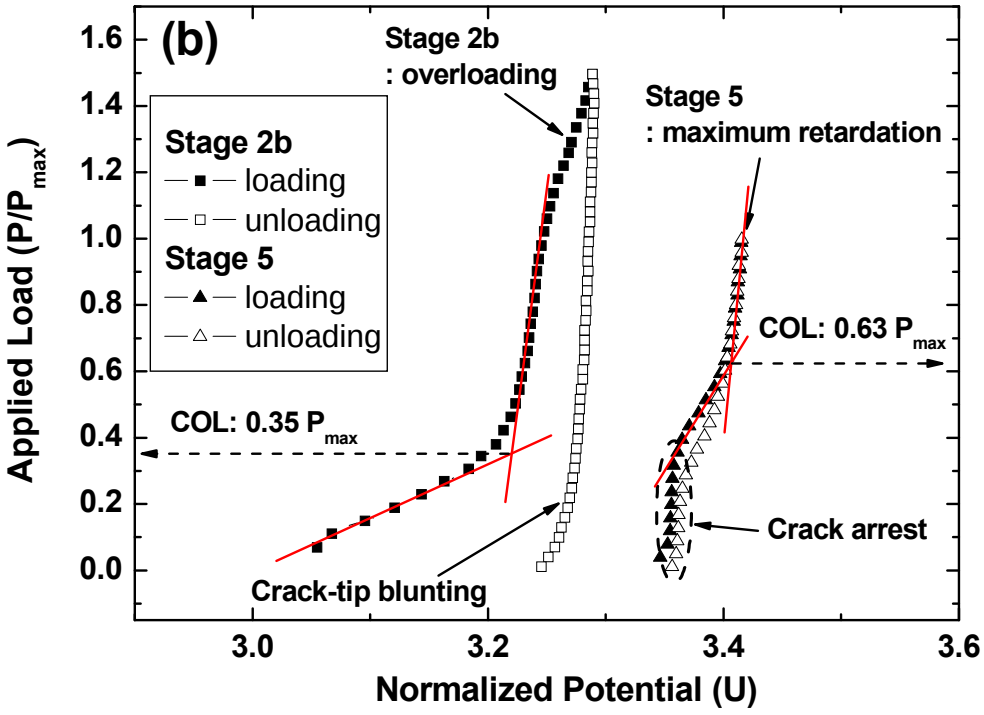

Figure 7.4: Continued.

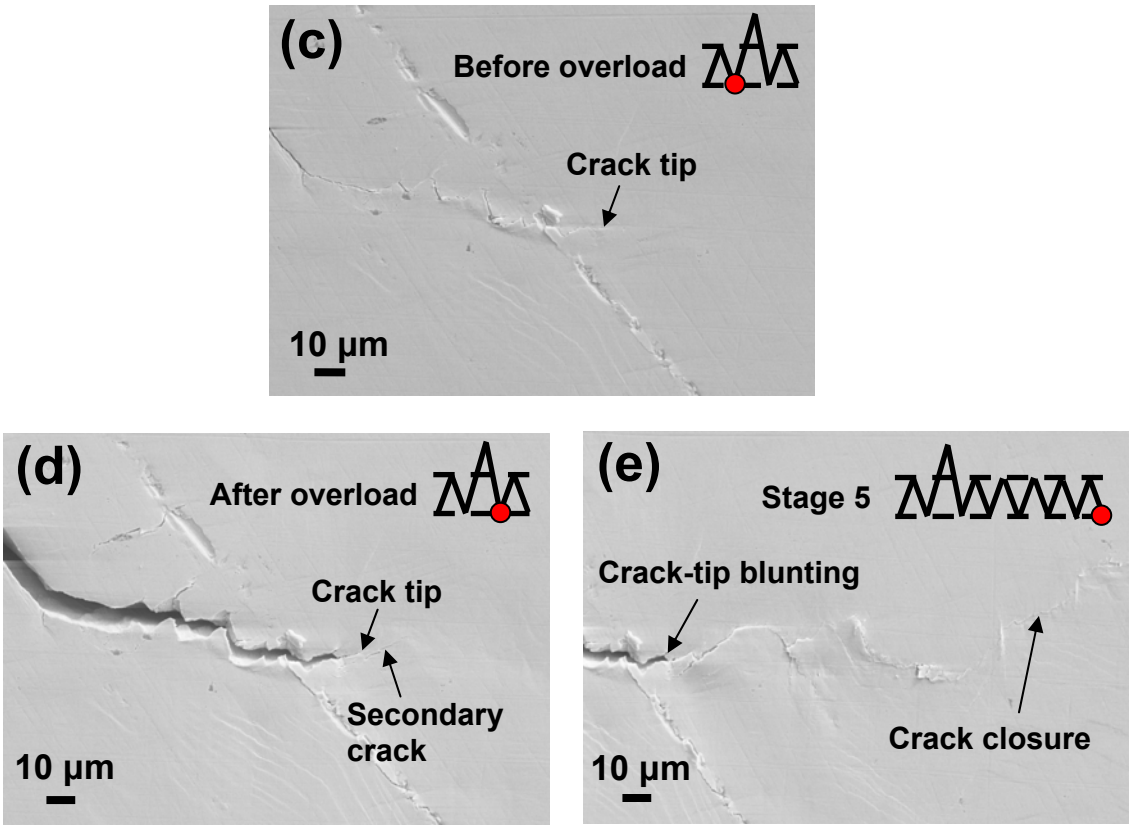

Figure 7.4: Continued.

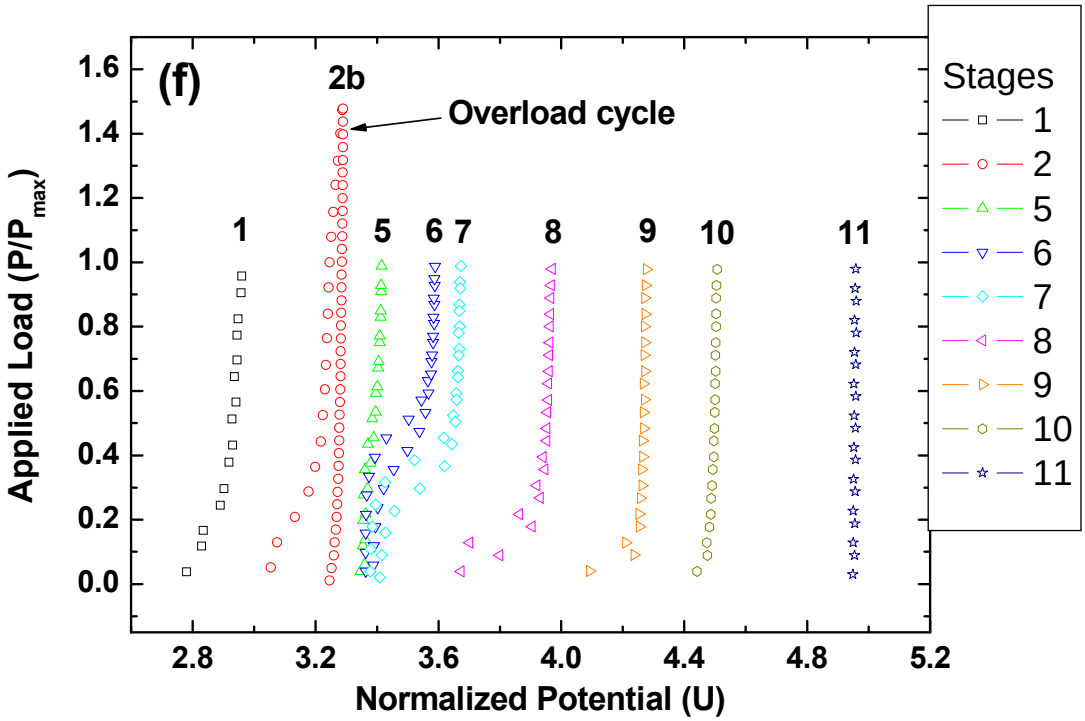

Figure 7.4: Continued.

behavior not following the loading curve. Only the potential decreased vertically down, followed by a small transition region at a lower load.

The potential change vs. applied load at the maximum retardation (the stage 5 marked in Fig. 7.1) was also shown in Fig. 7.4(b). This potential change shows quite a different behavior compared to that at the stage 2a. When the load increases up to 0.35 $P_{max,}$ the potential did not change. As a higher load was applied, the potential began to increase linearly up to 0.59 P_{max}, followed by a transition region (from 0.59 P_{max} to 0.68 P_{max}) and a sharp increase of the potential (from 0.68 P_{max} to P_{max}). During unloading, the potential change showed a similar trend following a loading curve.

Figures 7.4(c)-(e) show scanning-electron microscope (SEM) micrographs at the crack tip without load before and after the overload, and at the stage 5. Before the overloading [Fig. 7.4(c)], the crack was completely closed, while the crack-tip blunting was clearly observed with a few secondary cracks near the tip after the overloading [Fig. 7.4(d)]. Figure 7.4(e) (stage 5) showed that the crack-tip blunting still remained and the fatigue crack was closed in the crack-wake region, where further cyclic deformation was applied after the tensile overloading.

Figure 7.4(f) shows the potential measurements during a single loading-unloading cycle at eleven different crack-growth stages through the retardation period. At the stage 1 (constant-amplitude crack growth before the overloading), a loading and unloading potential curve showed the reversible behavior. At the stage 2b (an overloading cycle), after applying a single tensile overload, the potential did not change nearly during unloading indicating the irreversible behavior. At the stage 5 (a maximum

retardation point), it was found that the potential did not change when the load below 0.35 P_{max} was applied. At the stages 6-8, the magnitude of load, at which the potential did not change, became smaller. Finally, the shape of a potential curve at the stage 9 was similar to the stage 1 and the first linear region in the potential was gradually decreased as the crack further propagated (stages 10 and 11).

7.3.3 Neutron-diffraction measurements

Figure 7.5 shows the transverse residual-stress distribution as a function of the distance from the overload point. Note that the overload point is corresponding to the crack-tip position at the stage 2. In Fig. 7.5(a), the compressive residual stresses with a maximum of about –70 MPa were measured near a fatigue crack tip (–4 ~ 1 mm) at the stage 2a, right before the overloading. After an application of a single tensile overload, a relatively much larger compressive residual stresses were observed in a larger range from the crack tip (–4 ~ 4 mm). The highest compressive residual stress of –225 MPa was examined at 0.5 mm ahead of the crack tip. Figure 7.5(b) shows the residual-stress evolution after the tensile overloading. As the fatigue crack propagates through the retardation period, the compressive residual stresses were relaxed and became smaller.

Figures 7.6(a)-(e) show the internal-strain evolutions as a function of the applied load at various locations with different distances from the crack tip. A dot is an experimental data measured from a neutron-diffraction technique and a solid line is the fitting result obtained from a linear fitting Origin program. Figure 7.6(a) presents the internal-strain evolution at the stage 2a (just before overloading). The lattice strain did

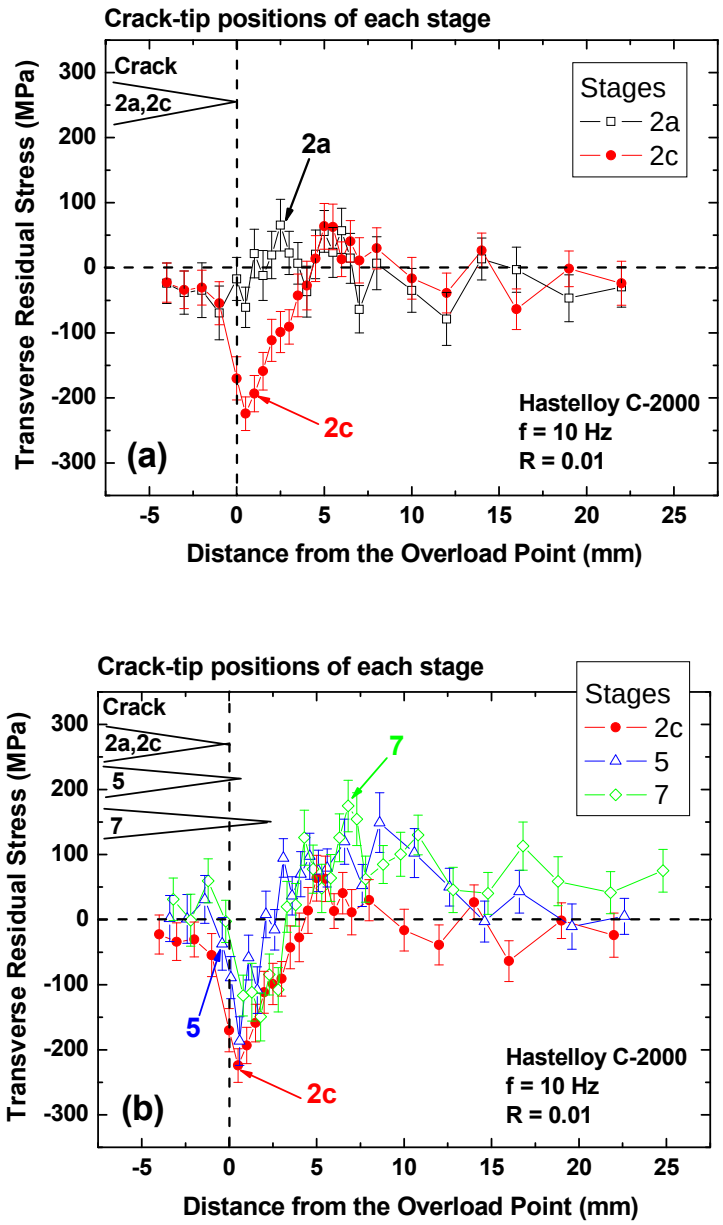

Figure 7.5: Transverse residual-stress profiles at (a) the stages 2a and 2c; (b) the stages 2c, 5, and 7 measured along the crack-growth direction (x).

Figure 7.6: Internal-strain evolutions as a function of the load at various locations from the crack tip at the (a) stage 2a, right before the overloading; (b) stage 2b, right after the overloading; (c) stage 5, a maximum retardation point; (d) stage 6 marked in Fig. 7.1; and (e) stage 7 marked in Fig. 7.1.

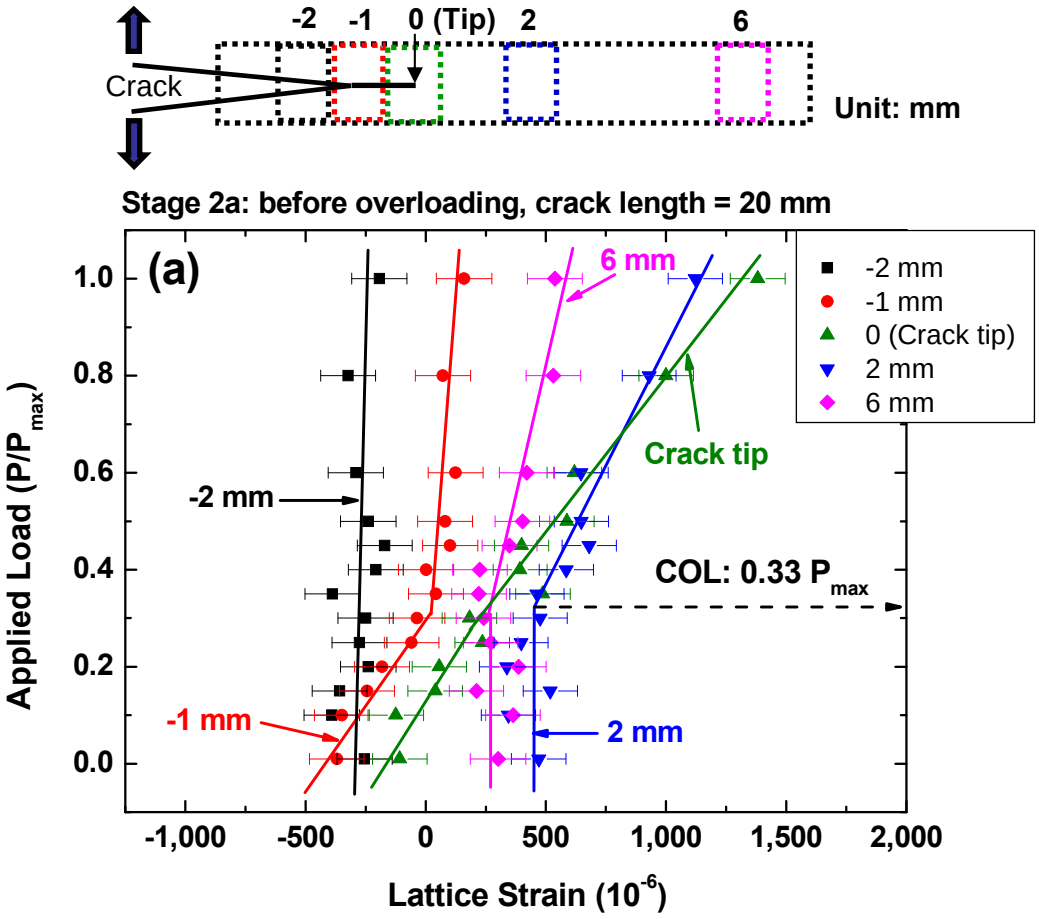
-2
-1
0 (Tip)
2
6
Crack
Unit: mm
Stage 2a: before overloading, crack length = 20 mm
(a)
6 mm
-2 mm
-1 mm
0 (Crack tip)
2 mm
6 mm
Crack tip
-2 mm
COL: 0.33 P max
-1 mm
2 mm
Applied Load (P/P max)
Lattice Strain (10-6)
1.0
0.8
0.6
0.4
0.2
0.0
-1,000
-500
0
500
1,000
1,500
2,000

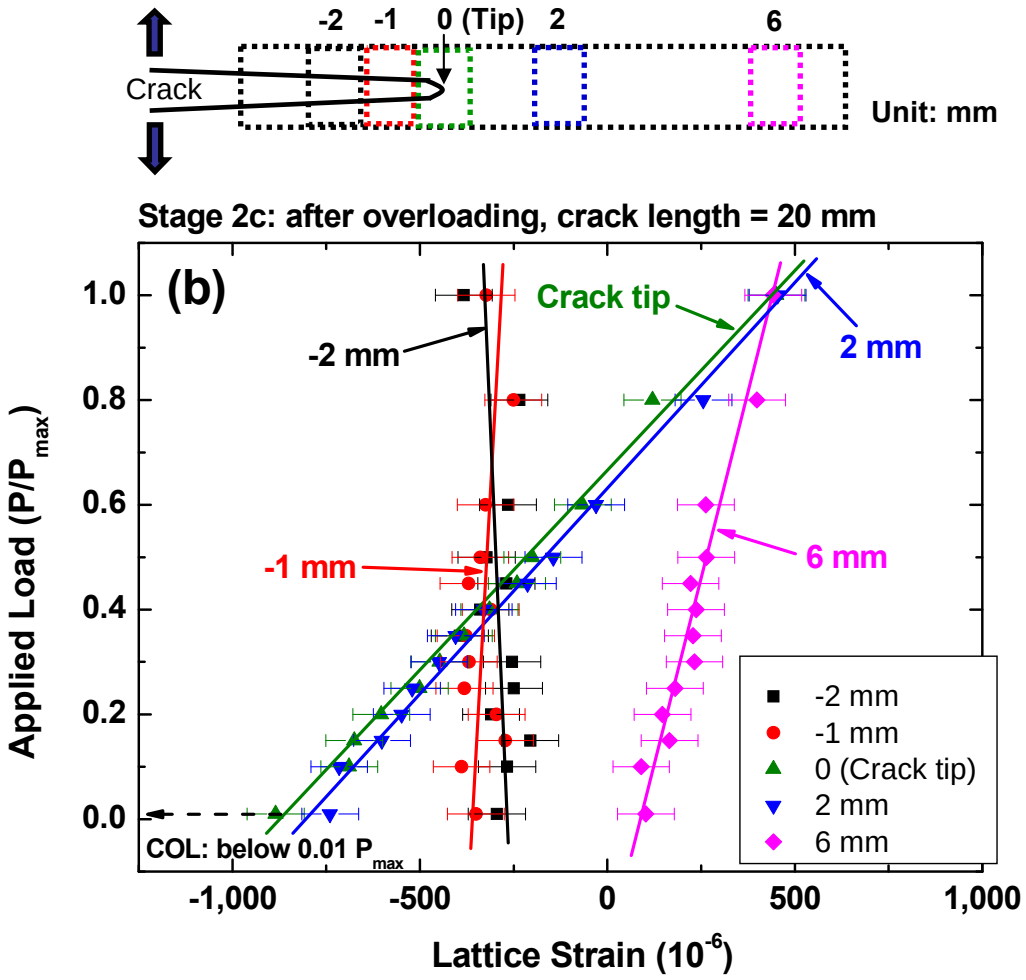

Figure 7.6: Continued.

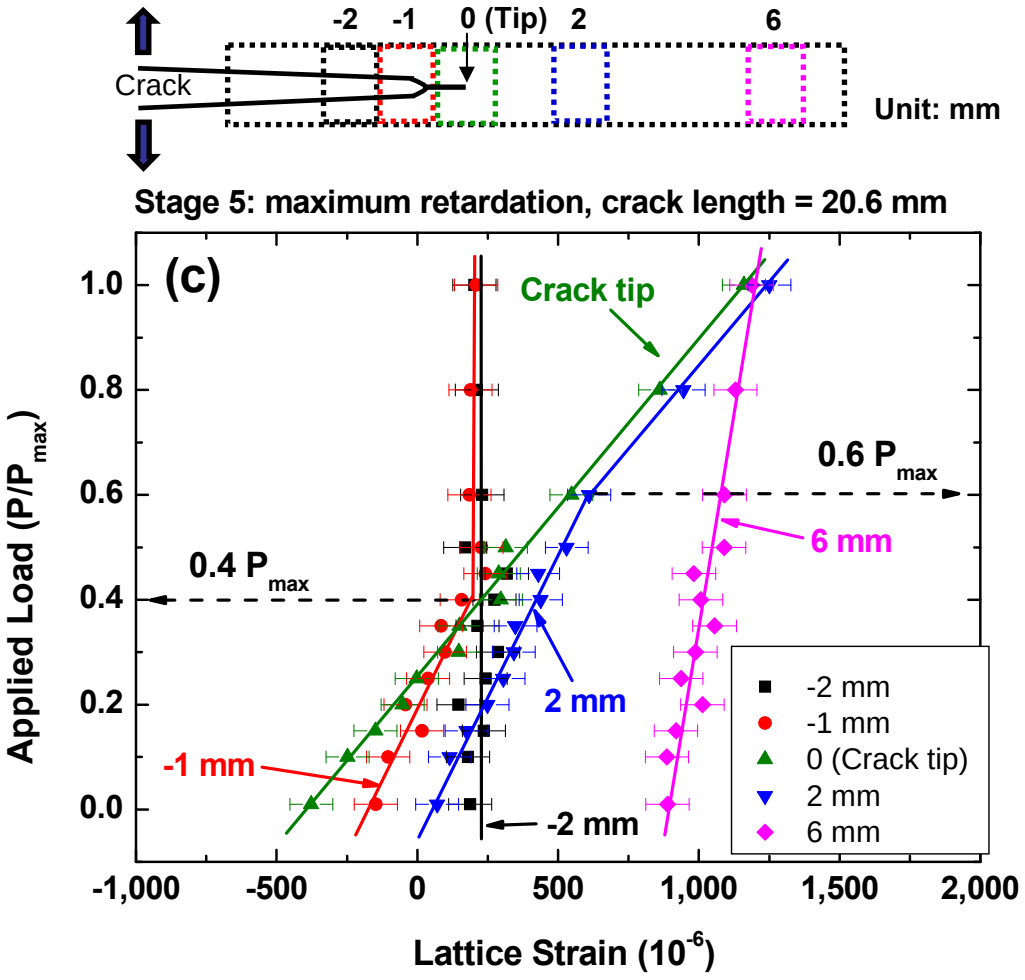

Figure 7.6: Continued.

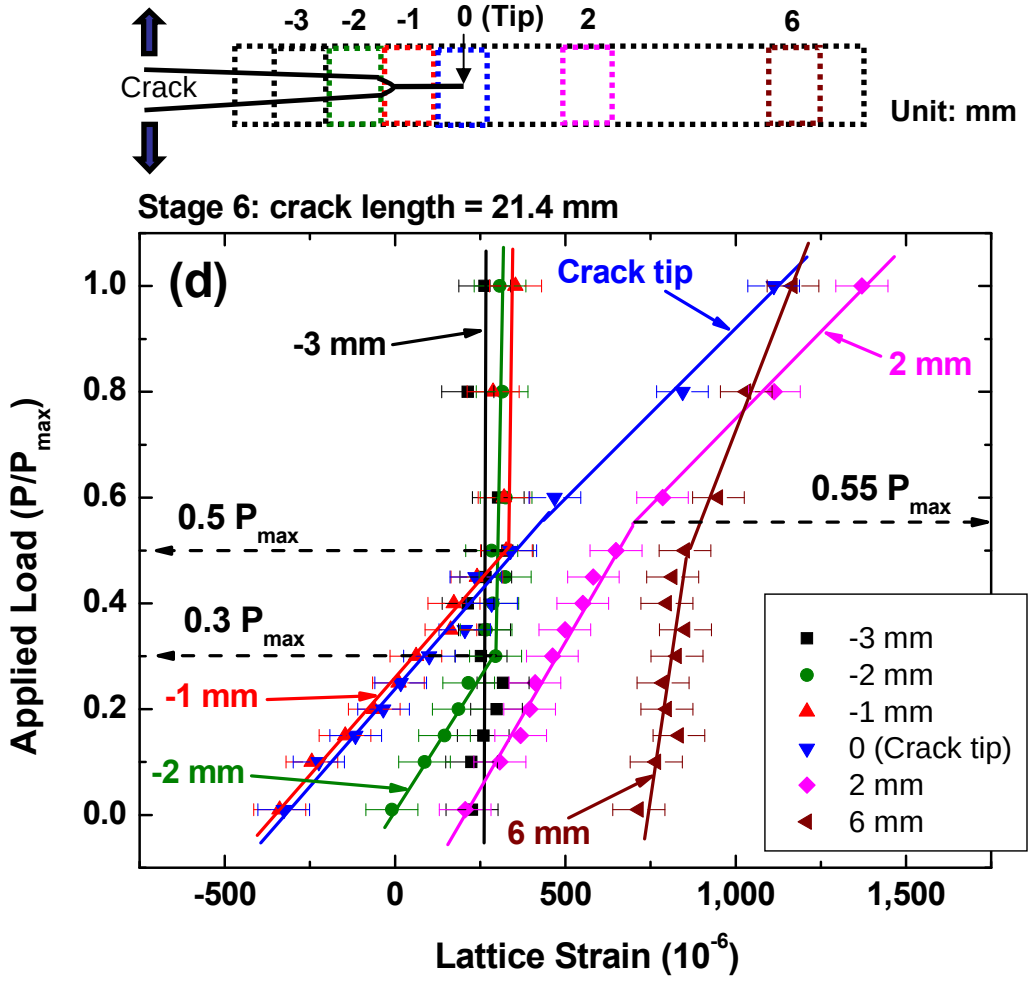

Figure 7.6: Continued.

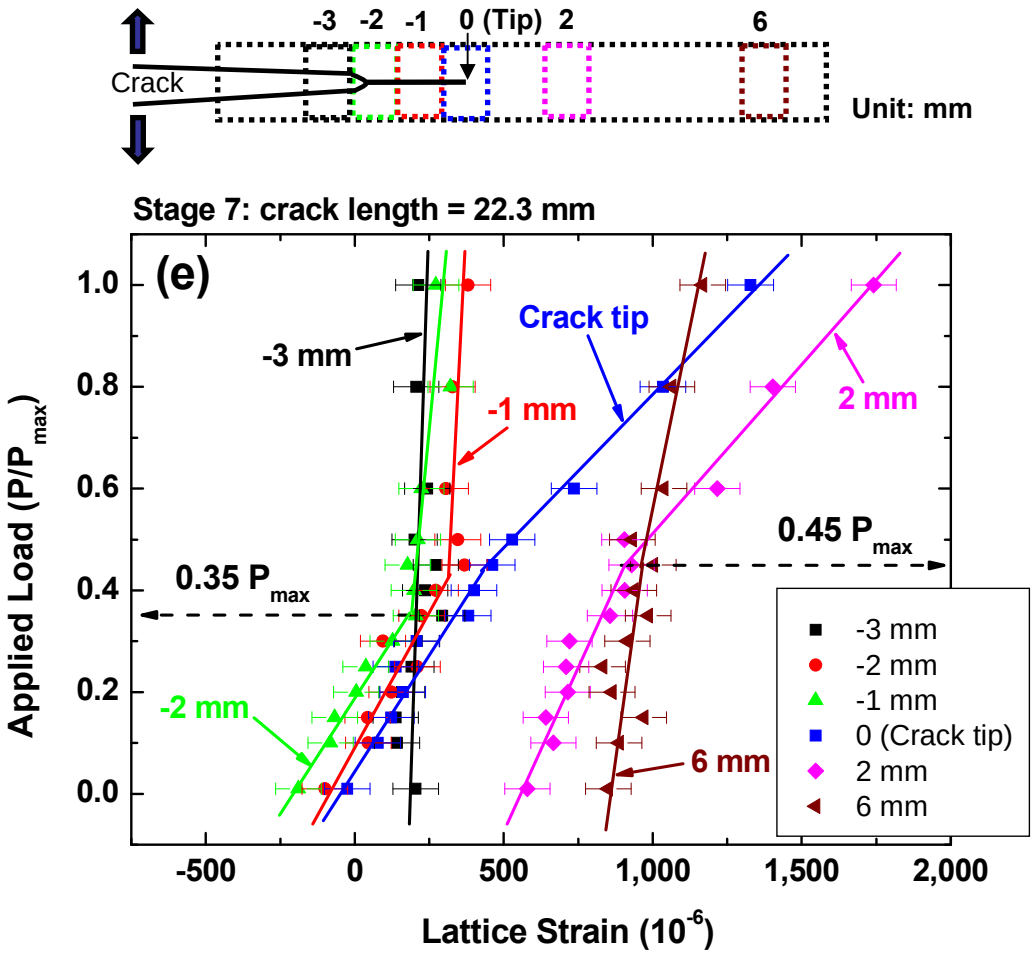

Figure 7.6: Continued.

not change with increasing the applied load at the location of 2 mm behind the crack tip. At the position of 1 mm behind the crack tip, the lattice strain increased linearly, as the load below about 0.31 P_{max} was applied. However, the lattice strain did not nearly change as a higher load was introduced. The lattice strain at the crack tip increased gradually with increasing the applied load, indicating a slight change in the slope. At the locations of 2 and 6 mm in front of the crack tip, a clear change in the slope of lattice strain vs. load was examined. The lattice strain did not change when the load below about 0.33 P_{max} was imposed. On the other hand, the lattice strain increased linearly with increasing the load from 0.33 P_{max} to P_{max} at both locations. The larger change in the slope of lattice strain vs. load was observed at 2 mm than 6 mm ahead of the crack tip. It should be noted that the different lattice-strain evolutions were observed as a function of the distance from the crack tip.

Figure 7.6(b) shows the lattice-strain evolutions at the stage 2c (right after the tensile overloading) at the same positions indicated in Fig. 7.6(a). Interestingly, the lattice strain at the location of 1 mm behind the crack tip did not change with increasing the applied load and the changes in the slope at the locations 2 and 6 mm ahead of the crack tip were not examined.

Figure 7.6(c) shows the lattice-strain evolutions at the stage 5 (a maximum retardation point). At the location of 1 mm behind the crack tip, the lattice strain initially increased, but it did not change when the load greater than 0.4 P_{max} was applied. At the location of 2 mm in front of the crack tip, the change in the slope of lattice strain vs. load was observed at 0.6 P_{max}.

Figure 7.6(d) shows the lattice-strain evolutions at the stage 6. The change in the lattice strain was not found at the location of 3 mm behind the crack tip. At the locations of 2 and 1 mm behind the crack tip, the change in the slope was examined at 0.3 P_{max} and 0.5 P_{max}, respectively. At the locations of 2 mm ahead of the crack tip, the lattice strain increased gradually with increasing the applied load, revealing the change in the slope at 0.55 P_{max}, which was lower than that of the stage 5. In Fig. 7.6(e) (the stage 7), the load value, where the slope is changed, at the location of 2 mm ahead of the crack tip further decreased to 0.45 P_{max}, as compared to that of the stage 6.

7.4 Discussion

7.4.1 Crack-Closure Phenomena and Crack-Opening-Load Variations through the Retardation Period

The first linear region shown in Fig. 7.4(a) (P_{min} ~ 0.25 P_{max}) during a loading cycle is caused by a gradual crack opening from the crack closure in a crack-wake region, i.e., the disappearance of the crack-face contact. In other words, the closed crack face [shown in Fig. 7.4(c)] from the previous unloading cycle begins to open with increasing the applied load, resulting in a significant change in the electric potential. The second linear region (0.54 P_{max} ~ 0.83 P_{max}) might be due to the dominant elastic deformation at the crack tip accompanying the elastic dimensional change of the material, after the crack tip is fully open. A transition region observed at the applied load from 0.25 P_{max} to 0.54 P_{max} might be owing to the different crack-opening levels

between the surface and interior of the material. Note that the electric-potential measurement shows the bulk response of the material.

As the load was applied from 0.83 P_{max} to P_{max}, the third linear region of the potential was observed. This linear region results from the actual crack-length increment accompanying the dominant plastic deformation at the crack tip. From such a potential measurement during a loading cycle, the bulk-averaged crack-opening load (COL) can be determined by a bilinear fitting from the first and second linear regions. Thus, the crack-opening load of 0.34 P_{max} was measured in case of the stage 2a. During unloading, the crack face is closed again, following a reverse step.

A large normalized potential change of 0.04 was examined at the stage 2b (during the overloading) shown in Fig. 7.4(b). It revealed that a tensile overload resulted in a higher increase of the actual crack advance with larger plastic deformation than that in the loading case just before the overloading. During unloading, the potential was slightly reduced due to elastic unloading, followed by a small transition region at a lower load. As a result, it turned out that there is no crack closure in a crack wake region and only new crack face created by an overload was closed showing a small transition region. In order to confirm the results of the potential measurement, the shape of the crack tip was investigated using SEM. Right after the tensile overloading, the large crack-tip blunting with small secondary cracks was observed, which confirmed that there was no crack face contact behind the crack tip.

As the load increases up to 0.35 P_{max} at the stage 5 (a maximum retardation point), the potential did not change. It means that the closed crack face between crack-

tip blunting region and actual crack-tip position did not open (i.e., crack arrest), even though the load were imposed from P_{min} to 0.35 P_{max}. As a higher load was introduced, the electric potential began to increase linearly (0.35 P_{max} ~ 0.59 P_{max}), followed by a transition region (0.59 P_{max} ~ 0.68 P_{max}) and a slight increase of the potential (0.68 P_{max} ~ P_{max}), corresponding to the gradual closed-crack opening, crack-tip fully opening, and the dominant elastic loading, respectively. During unloading, the crack was closed again following a reverse step of a loading curve. From the bilinear fitting, high bulk-averaged crack-opening load of 0.63 P_{max} was obtained at the maximum retardation point (stage 5).

Potential measurements at various crack-growth stages marked in Fig. 7.1 were put together to compare, as exhibited in Fig. 7.4(f). At the stage 1 (constant-amplitude fatigue-crack growth before the overloading), a loading and unloading potential curve showed the reversible behavior and the COL of 0.34 P_{max} was measured. At the stage 2b (an overloading cycle), the potential curve showed the irreversible behavior indicating that the crack closure did not occur and the COL sharply dropped down. As the crack propagated to the stage 5 (a maximum retardation point) after applying a single tensile overload, the largest crack arrest portion appeared up to 0.35 P_{max} and the highest crack-tip opening load of 0.63 P_{max} was examined. When the crack grew from the stages 5 to 9, the crack arrest portion became smaller and it completely disappeared at the stage 9, which led to a gradual decrease of the crack-opening load (COL of the stage 9 = 0.16 P_{max}), Finally, the shape of potential curve at the stage 9 was very similar to the stage 1 (constant-amplitude crack growth before the overloading), which supported that the

crack-growth rate was already fully recovered to a pre-overload slope. As the crack grew further to the stage 11, the crack-opening load became smaller and finally zero at the stage 11.

The COL variations at eleven crack-growth stages through the da/dN vs. ΔK curve were presented in Fig. 7.7(a). As the fatigue crack propagated from the stages 1 to 2a (see Fig. 7.1), the COL was reduced from 0.36 P_{max} to 0.34 P_{max}. Right after the tensile overloading (stage 2c), the COL was dropped down to about 0.06 P_{max}. As the crack grew from the stages 3 to 5 (a maximum retardation point), the COL was sharply increased, revealing the highest COL of 0.63 P_{max}. As the crack further grew from the stages 5 to 11, the COL was gradually reduced and finally reached zero at the stage 11. It should be noted that such changes in the COL are related to those in the experimentally measured crack-growth rate (Fig. 7.1).

7.4.2. Correlation between the Crack-Growth Behavior and ΔK_{eff}

Figure 7.7(b) shows the effective-stress-intensity-factor range (ΔK_{eff}) vs. ΔK at eleven crack-growth stages marked in Fig. 7.1. As the ΔK increases from the stages 1 to 2a (cycle just before the overloading), the ΔK_{eff} increased from 20.95 to 23.93 MPa.m$^{1/2}$. Immediately after a single tensile overload was introduced (stage 2c), the ΔK_{eff} increased instantaneously to 34.27 MPa.m$^{1/2}$, which corresponds to an instantaneous acceleration of the crack-growth rate. At the stages 3, 4, and 5, the ΔK_{eff} sharply decreased with increasing the ΔK. Note that the minimum ΔK_{eff} of 13.84 MPa.m$^{1/2}$ was obtained at the stage 5 (the lowest crack-growth-rate point within the

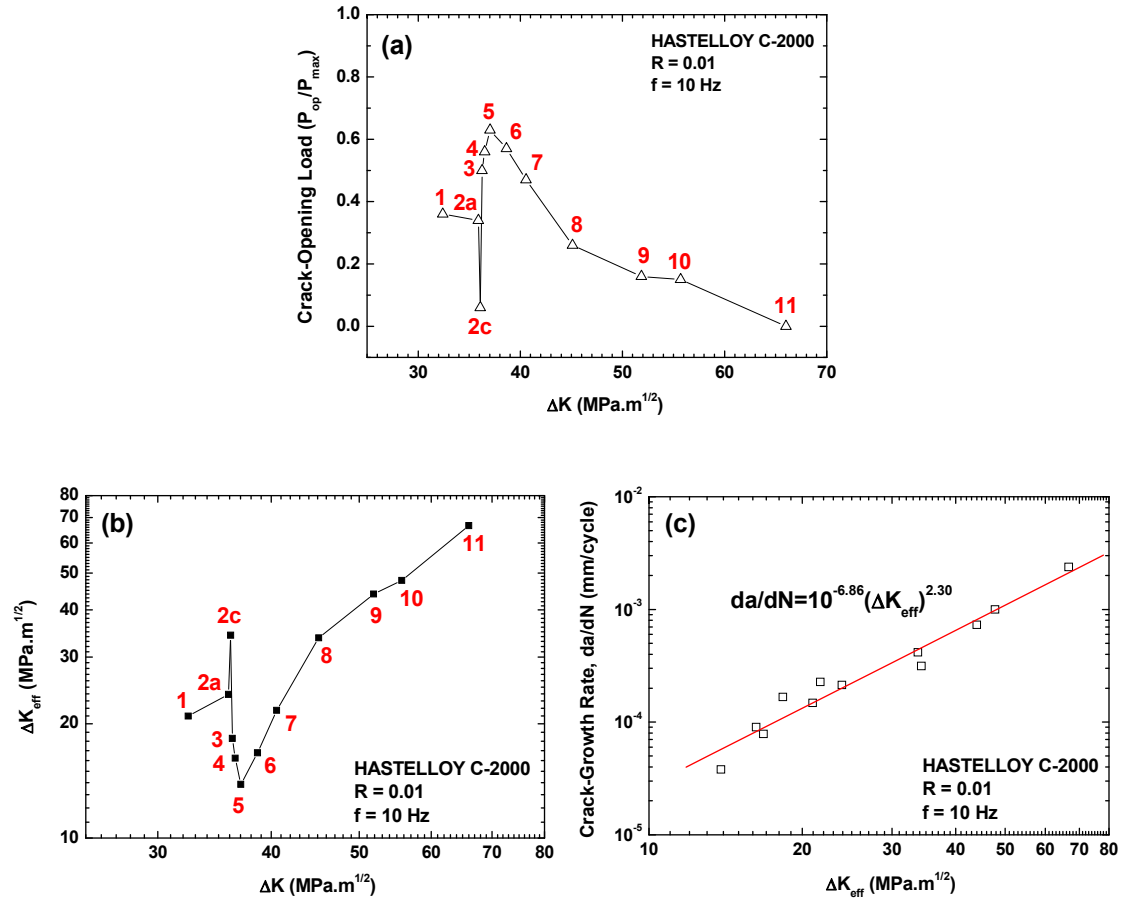

Figure 7.7: (a) Crack-opening load vs. ΔK, (b) ΔK_{eff} vs. ΔK, and (c) da/dN vs. ΔK_{eff} at various crack-growth stages marked in Fig. 7.1.

retardation period). This trend was consistent with a sharp decrease in the crack-growth rate after the tensile overloading (stages 3–5 in Fig. 7.1). As the crack propagates further from the stages 5 (a maximum retardation point) to 11, the ΔK_{eff} increased gradually with increasing the ΔK, which was in good agreement with a gradual increase in the crack-growth rate after the stage 5. Thus, it is noted that the changes in the ΔK_{eff} were closely associated with those in the da/dN shown in Fig. 7.1.

Four distinct slopes from the curve of da/dN vs. ΔK were found, as shown in Fig. 7.1: (case1) a slope (between stage 1 and 2a, and stage 8 and 11) from pre-overload constant-amplitude crack growth; (case2) a slope indicating an initial acceleration right after the tensile overloading; (case 3) a slope showing a sharp decrease between stage 2c and 5; (case 4) a slope between stages 5 and 7, which is larger than that in the case 1, but smaller than that in the case 3. Note that the slope change in crack-growth rate is depending on the change in the ΔK_{eff}, which is a function of the COL. As shown in Fig. 7.7(a), the COL in the constant-amplitude crack-growth without overload decreased slowly with increasing the ΔK (see the COL change in the stage 1–2a and 8–11), and, thus, the change in the ΔK_{eff} was also increased slowly. After a single tensile overload was introduced, very low COL was obtained, resulting in a sharp increase of ΔK_{eff}. In the case 3, the COL increased so fast with a short increment of crack length (i.e., 0.6 mm from an overload point), which resulted in a sharp decrease of ΔK_{eff}. Likewise, in the case 4, the gradual decrease of COL, which has higher reduction rate than that in the case 1, was examined. Thus, an increase rate in the ΔK_{eff} from stages 5 to 8 is faster than that in the case 1. It can be noted that the change of the ΔK_{eff} shown in

Fig. 7.7(b) was exactly corresponding to a slope change of experimentally measured crack-growth rate, as exhibited in Fig. 7.1.

To investigate the applicability of ΔK_{eff} as the actual fatigue-crack-tip-driving force, the crack-growth rate (da/dN) was plotted as a function of the ΔK_{eff}, as presented in Fig. 7.7(c). The crack-growth rate had a good correlation with the ΔK_{eff} following a linear line, which suggests that the ΔK_{eff} can be considered as fatigue-crack-tip-driving force.

7.4.3 Internal-Strain Evolution, Determination of Crack-Opening Load, and Stress-Transfer Observation using Neutron Diffraction

The different lattice-strain evolutions shown in Fig. 7.6(a) (stage 2a, before the overloading) are related to the crack-closure phenomenon in a fatigue crack-wake region and the stress distribution varying with the applied load. When the load is imposed, the stress field is initially distributed near the closed crack (e.g., –1 mm and 0). Thus, the only lattice strains at the locations of –1 mm and 0 (tip) increased linearly with increasing the applied load, while the lattice strain did not change at the locations of –2 mm (the crack was fully open) and the positions of 2 and 6 mm, where the stress field was not reached. As a higher load was introduced, the stress concentration moved toward the crack-tip position with a gradual opening of the closed crack, and, hence, the invariant lattice strains at the location of –1 mm were observed at the load values above about 0.31 P_{max}, indicating that the closed crack was already open at the location of –1 mm. Finally, when the 0.33 P_{max} is imposed, the crack tip, where the stress

concentration takes place, is fully open and the locations away about 2 mm in front of the crack tip are subjected to these crack-tip stress fields. As a result, the lattice strains at the locations of 2 and 6 mm began to increase linearly with increasing the applied load above 0.33 P_{max}, as exhibited in Fig. 7.6(a). Based on the distinct lattice-strain evolutions at various locations from the crack tip, it should be noted that the bulk-averaged crack-opening load, 0.33 P_{max}, can be reasonably determined from a bilinear curve fitting at about 2 mm ahead of the crack tip (the most distinguishable change in a slope) using in-situ neutron diffraction.

Figure 7.6(b) showed quite different lattice-strain evolutions right after the overloading at the exactly same position examined in Fig. 7.6(a). Note that the change in a slope shown at the locations of –1, 2, and 6 mm in Fig. 7.6(a) disappeared. It is evident that such a difference in the strain evolution after the overloading also supports the fully crack-opening, i.e., the crack-tip blunting immediately after the overload, as shown in Fig. 7.4(b). The crack-tip blunting leads the stress distribution not behind the crack tip but in front of the crack tip, as the load increases. Thus, the resulting lattice strain at –1 mm behind the crack tip did not change and the lattice strains at 2 and 6 mm ahead of the crack tip increased linearly with increasing the applied load, corresponding to the stress distributions in front of the crack tip. It should be emphasized that distinct load responses of the lattice strain at various locations from the crack tip result from the difference in the stress distributions around the crack tip, as similarly observed in the 316 stainless steel (Lee et al., 2008).

The change in a slope (at about 0.4 P_{max}) at the location of –1 mm shown in Fig. 7.6(c) represents the transfer in the stress distribution from a blunting region to actual crack-tip position. As the load is initially imposed, the stress concentration occurs at a crack-tip blunting region due to the crack closure in a fatigue-wake region caused by the large compressive residual stresses after the overloading. The occasional crack branching occurring right after the overloading partially contributes the stress concentration at a blunting region. As a result, the stresses are distributed as a function of the distance from the blunting region and the lattice strain initially increases at the location of –1 mm (a crack-blunting region) as well as the locations ahead of the crack tip. When about 0.35 P_{max} [approximately the maximum crack-arrest load shown in Fig. 7.4(b)] is applied, the closed crack starts to open by overcoming the overload-induced compressive residual stress fields in a crack-closure region. When a higher load is applied, the closed crack is gradually open, resulting in the transfer of stress concentration from the blunting region to actual crack-tip position. The invariant lattice strain above about 0.4 P_{max} at the location of –1 mm clearly revealed that the closed crack was already open at this location and the stress concentration was moved toward the actual crack tip. When about 0.63 P_{max} is applied, the crack tip is fully open [Fig. 7.4(b)], and, finally, the stress concentration occurs at the crack tip. The lattice-strain response at the location of 2 mm also showed similar bulk-averaged COL, 0.6 P_{max}, from the change in a slope, as exhibited in Fig. 7.6(c).

Figures 7.6(d) and (e) also show the stress-transfer phenomena from distinct internal-strain evolution at various locations from the crack tip. In Fig. 7.6(d), when the

load is applied, it is revealed that the stress is not applied at the location of –3 mm from the invariant lattice strain. However, at the location of –2 mm, which is slight behind a blunting point, it was found that the stress was only applied until 0.3 P_{max}, and, then, the stress concentration was transferred above this load level. It is noted that this load value was consistent with the maximum crack-arrest load, 0.32 P_{max}, at the stage 6, Fig. 7.4(f). As the applied load was introduced from 0.3 P_{max} to 0.5 P_{max}, the lattice strain at the location of –1 mm still increased linearly, revealing that the stress concentration currently stays at this range. When a higher load was applied, the invariant lattice strain at the location of –1 mm showed that the stress concentration was already moved at 0.5 P_{max}, and, finally, it was transferred at the crack tip at 0.55 P_{max}, as revealed in the change of a slope at the location of 2 mm.

Likewise, Fig. 7.6(e) showed that the stress concentration was gradually transferred from –2 mm (at 0.35 P_{max}) to the crack tip, resulting in the bulk-averaged COL of 0.45 P_{max}. Figure 7.8 shows the comparison of the COL measured from two different techniques, i.e., the electric potential and *in-situ* neutron diffraction. It is noted that the COLs obtained from *in-situ* neutron diffraction were in good agreement with those measured from the electric potential.

In summary, the distinct load responses at various locations away from the crack tip clearly showed the stress distributions in the vicinity of the crack tip under applied loads. Before the overloading, the stresses were initially distributed near a crack-closure region, and they were transferred and concentrated at the crack tip with increasing the applied load. Bilinear curves in the plot of lattice strain vs. load shown in the crack-

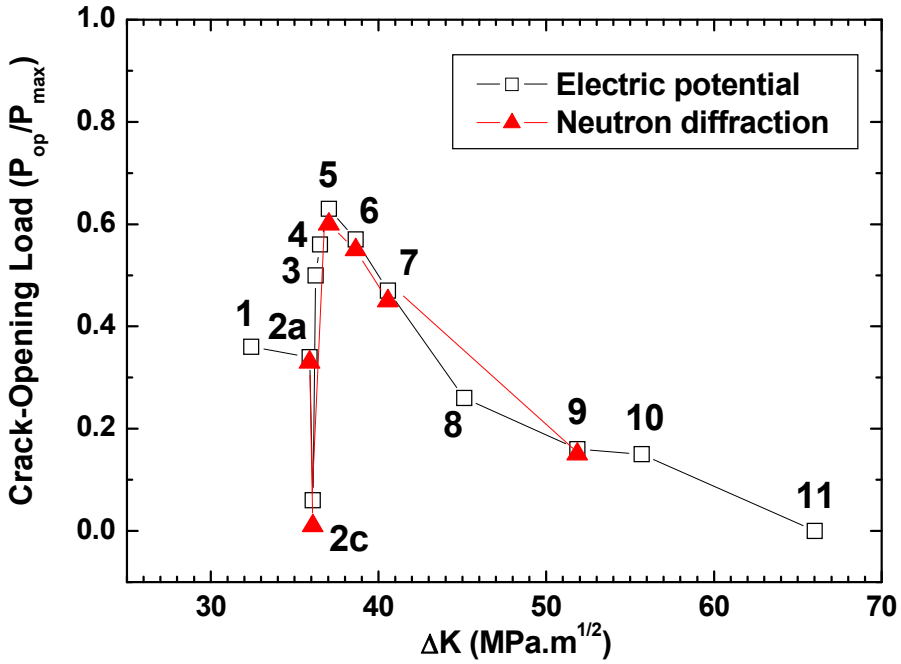

Figure 7.8: Comparison of the crack-opening loads between the electric potential and neutron diffraction.

closure region and about 2 mm ahead of the crack tip clearly revealed the effect of crack closure in the wake of a fatigue crack on the internal-strain evolution and the stress distribution under applied loads. In the retardation period after the tensile overloading, the combined effects of crack-tip blunting at an overload point and the crack closure accompanying the compressive residual stresses in the fatigue wake caused the stress concentration at a blunting region until a certain load value (related to the crack-arrest load), and, then, the stress concentration was gradually transferred from the blunting region to actual crack-tip location with a higher applied load. Finally, the stress concentration at the crack tip resulted in the most distinct strain response at about 2 mm ahead of the crack tip, which made it possible to determine the bulk-averaged COL using neutron diffraction.

7.4.4 Effects of Compressive-Residual Stress and Crack-Tip Blunting on the Crack-Opening Load

After a tensile overload was applied, the COL was gradually changed from stages 2c to 8, as exhibited in Fig. 7.6(a). The change in the COL within this period is associated with the combined effects between large compressive residual stress and the crack-tip blunting with secondary cracks. At the stage 5, the crack length was increased to 0.6 mm from an overload point (i.e., the crack-tip blunting region). The neutron-diffraction measurement revealed that large compressive residual stresses were applied in this closed crack [Fig. 7.5(b)]. To make the crack tip fully open, the fatigue crack should overcome this large compressive residual stress field applied in the wake of the

crack, and, thus, a higher COL was required. Furthermore, the observed crack-arrest load, 0.35 P_{max}, at the stage 5 would be associated with a load value to remove this large compressive residual-stress field.

The crack-tip blunting could be considered as another factor to influence the crack arrest and the determination of the COL. It is known that the crack-tip blunting behaves like a notch. As the load is applied, the stress field would be initially concentrated near a blunting region (i.e., an overload point), reducing the actual magnitude of the stresses applied in a crack wake as well as the crack-tip position. The crack branching (or secondary cracks) occasionally occurring immediately after the overloading could partially contribute the reduction of the stresses in a wake region by maximizing the blunting effect. Hence, a higher load should be required to reach the stress fields large enough to open the closed crack face. If the large compressive residual stress is also applied in the closed crack ahead of the crack-tip blunting, much higher load should be imposed to reach a certain critical stress value to open the closed crack face. Therefore, the crack arrest could be observed until a required stress value is obtained.

It should be pointed out that the crack-opening-variations with the retardation period highly depends on the crack length grown from the crack-tip blunting (an overload point), the degree of the crack-tip blunting, and the magnitude of compressive residual stress. If an actual crack-tip position is very close from an overload point (e.g., between the stages 2c and 3), the crack face will be open with a lower load. In contrast, if the crack-tip position is far away from an overload point (stage 8), the stress can

easily concentrate on the crack tip with increasing the applied load. Thus, the closed crack face will be also open with a lower load. It might be thought that there is a certain critical crack length away from an overload point, similar to the critical crack length of the fatigue threshold region. The stage 5 is usually observed at 0.3 – 0.6 mm from the overload point. This distance might be thought as a critical point where the combined effects between the large compressive residual stress and crack-tip blunting with secondary cracks are maximized. In summary, the combined effects of the large compressive residual stress and crack-tip blunting with secondary cracks are responsible for the observed changes in the COL within the retardation period, based on the crack-closure approach.

7.5 Conclusions

Electric-potential and neutron-diffraction experiments were carried out to investigate the overload-induced fatigue-crack-growth mechanisms. The main results are summarized as follows:

(1) Before overloading, the stresses were initially distributed near a crack-closure region, and they were transferred and concentrated at the crack tip with increasing the applied load.

(2) Immediately after the tensile overload was applied, the crack tip became blunt and the large compressive residual stresses were observed around the crack tip.

(3) An initial acceleration of the crack-growth rate is due to the crack-tip blunting with secondary cracks.

(4) In the maximum retardation point (stage 5), the highest crack-opening load was examined, indicating the smallest ΔK_{eff} value.

(5) As the crack propagates into the overload-induced plastic zone, the residual stresses were relaxed and stress values became smaller.

(6) In the retardation period after the tensile overloading, the combined effects of the crack-tip blunting at an overload point and compressive residual stresses accompanying the crack closure induced the stress concentration at a blunting region until a maximum crack-arrest load was reached. Then, the stress concentration was transferred from the blunting region to actual crack-tip location with gradual crack opening, requiring a higher applied load.

(7) Finally, the stress concentration occurred at the crack tip, resulting in the most distinct strain response at about 2 mm ahead of the crack tip, which made it possible to determine the bulk-averaged COL using an *in-situ* neutron diffraction technique.

(8) The combined effects of the compressive residual stress and crack-tip blunting with secondary cracks are responsible for the changes in the crack-opening load within the retardation period, resulting in the stress transfer from an overload point to the actual crack-tip position.

(9) The crack-opening levels measured from in-situ neutron diffraction were in a good agreement with those obtained from the electric potential.

(10) The post-overload crack-growth rates were normalized with the ΔK_{eff}. Therefore, the ΔK_{eff} can be considered as the fatigue-crack-tip-driving force.

Chapter 8

Conclusions

During constant-amplitude fatigue-crack growth, one of the following loading conditions was applied to study the effects of overloading, underloading, and their combinations on fatigue-crack growth: (*Case 1*) continuing with the fatigue loading under the same baseline condition, (*Case 2*) a single tensile overloading, (*Case 3*) a single compressive underloading, (*Case 4*) overloading-underloading, or (*Case 5*) underloading-overloading. After applying the various loading conditions, the constant-amplitude fatigue experiment was resumed for all cases to monitor the crack-growth behavior. *Case 1* showed a linear increase of the crack-growth rate with increasing ΔK. After *Case 2* (a single tensile overload) was introduced, the crack-growth rate was instantaneously accelerated, and, then, a large crack-growth-retardation period was observed. *Case 4* (overload-underload sequence) showed the significantly reduced crack-growth retardation, as compared to that of *Case 2*. On the other hand, after *Case 3* (a single compressive underload) was introduced, the crack-growth rate was initially accelerated, but the subsequent crack-growth rate was similar to that of *Case 1*. When *Case 5* (underload-overload sequence) was imposed, the crack-growth rates were similar to those of *Case 2*, indicating a large retardation period.

In order to understand these transient crack-growth behaviors, *in-situ* neutron-diffraction experiments were performed to examine the internal-strain evolution around a fatigue-crack tip under the five different loading conditions. The results showed how the residual strains were developed in the vicinity of the crack tip, and different crack-growth behaviors were closely related to the distinct residual-strain distributions developed near the crack tip under the various loading conditions.

The spatially-resolved neutron-diffraction measurements were performed to directly determine residual-stress distributions in the vicinity of the crack tip, immediately after applying five different variable-amplitude fatigue loadings (i.e., fatigued, tensile overloaded, compressive underloaded, tensile overloaded-compressive underloaded, and compressive underloaded-tensile overloaded) during fatigue-crack growth. The residual stresses were measured as a function of the distance from the crack tip along the crack-propagation direction. Among three principal residual-stress components, the transverse residual-stress distributions near the crack tip revealed the most distinct profiles, which can be closely associated with the experimentally measured different crack-growth behaviors under the five different loading cases.

The effects of a single tensile overload *(Case 2)* were studied in detail to probe the crack-growth retardation miromechanisms. The lattice-strain distributions and plastic deformation were examined around a crack tip after the overload using *in-situ* neutron-diffraction and polychromatic X-ray microdiffraction techniques. After the overload, the large compressive residual strains of –410 με (microstrain) were observed within ± 3 mm near a crack tip. It was found that the load response of lattice strain was

strongly dependent on the location from the crack tip. Dislocation densities were calculated as a function of the distance from the crack tip in the light of the diffraction-peak broadening. The high dislocation densities of approximately 8.5 x 10^{10} cm^{-2} are examined within ± 3 mm from a crack tip, supporting that the overload induced the severely large plastic deformation near the crack tip. Moreover, crystallographic tilts are considerably observed beneath surface around a crack tip, which are consistent with high dislocation densities near a crack tip measured by neutron-peak broadening.

Neutron diffraction was employed to investigate the evolution of residual-strain distributions through an overload-induced retardation period. The results reveal a large compressive residual-strain field near the crack tip immediately after the overload. As the fatigue crack propagates through the overload-induced plastic zone, the compressive residual strains are gradually relaxed, and new compressive residual-strain field is developed around the propagating crack tip, illustrating that the subsequent fatigue-induced plastic zone grows out of the large plastic zone caused by the overloading. The obtained results clearly show the interactions between the overload-induced plastic zone and subsequent fatigue-induced plastic zone; and its influence on the residual-strain distributions in the perturbed plastic zone.

In-situ neutron-diffraction and electric-potential techniques were employed to investigate the crack-opening/closing processes and internal-stress distributions near the crack tip during fatigue-crack propagation following a tensile overload. Before overloading, the stresses were initially distributed near a crack-closure region, and they were transferred and concentrated at the crack tip with increasing the applied load.

Immediately after applying a tensile overload, the crack tip became blunt and the large compressive residual stresses were developed around the crack tip. In a retardation period after the overload, the combined effects of crack-tip blunting occurring at an overload point and compressive residual stresses accompanying crack closure in a crack wake induced the stress concentration at a blunting region until a maximum crack-arrest load was reached. Then, the stress concentration was transferred from the blunting region to actual crack-tip position with a gradual crack opening, requiring a higher applied load. Finally, the stress concentration occurred at the crack tip, resulting in the most distinct strain response at about 2 mm ahead of the crack tip, which made it possible to determine the bulk-averaged crack-opening load using an *in-situ* neutron diffraction technique. It is revealed that the crack-opening loads obtained from in-situ neutron diffraction were in good agreement with those measured from the electric potential. The measured crack-growth rate can be normalized with the ΔK_{eff}, which suggests that the ΔK_{eff} can be considered as a fatigue-crack-tip-driving force.

It is expected that current results will have a great impact not only on developing the lifetime-prediction model, but also on improving the design for critical applications subjected to fatigue failures with random loadings. Moreover, the gained knowledge should be used as important references for providing the guidance and suggestions for understanding the fatigue-crack deformation and fracture behavior of other materials system, such as bulk metallic glasses and nanomaterials, and for the development of new materials with a better cracking resistance.

Chapter 9

Future work

Finite-element modeling (FEM) will be carried out using a cohesive-interface model that is described as follows: The irreversible, hysteretic-cohesive-interface model will be implemented into the commercial FEM software, ABAQUS, through a user-define element (UEL) subroutine (Nguyen et al, 2001; Serebrinsky & Ortiz, 2005; Gao & Bower, 2004; Xia et al., 2007). In this model, during monotonic loading, the traction, T_n, and separation, Δ_n, are related to the interface tensile strength, $\sigma_{\max}$, and characteristic length scale, δ_n, as shown in the following equation:

$$T_n = \sigma_{\max} \frac{\Delta_n}{\delta_n} \exp\left(1 - \frac{\Delta_n}{\delta_n}\right) \tag{9.1}$$

During unloading and reloading, the traction, T_n, and separation, Δ_n, are given as follows:

$$\dot{T}_n = \begin{cases} K^- \dot{\Delta}_n, & \dot{\Delta}_n < 0 \\ K^+ \dot{\Delta}_n, & \dot{\Delta}_n > 0 \end{cases} \tag{9.2}$$

where K^- and K^+ are the unloading and reloading stiffnesses, respectively. It is assumed that the unloading curve directs towards the origin,

$$K^{-} = T_n^{unload} \big/ \Delta_n^{unload} \tag{9.3}$$

On the other hand, the reloading stiffness, K^{+}, varies with the following kinetic relation:

$$\dot{K}^{+} = \begin{cases} -K^{+} \dfrac{\dot{\Delta}_n}{\delta_f}, & \dot{\Delta}_n > 0 \\ \left(K^{+} - K^{-}\right) \dfrac{\dot{\Delta}_n}{\delta_a}, & \dot{\Delta}_n < 0 \end{cases} . \tag{9.4}$$

where δ_f and δ_a are phenomenological constitutive parameters.

Using this model, the crack-growth behaviors under five different loading conditions (see Chapters 3 and 4) will be simulated. Internal-strain evolutions near the crack tip (see Chapter 3) will be investigated during overloading, underloading, and their combinations to observe the development of residual strains using FEM. Residual-stress distributions right after applying five loading cases will be compared to those of neutron-diffraction measurements (see Chapter 4). Furthermore, the residual-strain evolutions will be examined through an overload-retardation period (see Chapter 6), and internal-strain developments under applied loads will be studied at the different crack-growth stages after the overload (see Chapter 7). Strain responses at various locations from the crack tip will be investigated with increasing the applied load. Consequently, the crack-opening load can be determined from the plot of the load versus elastic strain using FEM. The crack-opening levels at the various crack-growth stages through the retardation period after the overload will be obtained and compared to help understand the crack-closure behavior after the overload. Moreover, these crack-opening levels

calculated by FEM will be compared to those from the electric-potential and *in-situ* neutron-diffraction measurements.

Bibliography

Allen AJ, Bourke MAM, Dawes S, Hutchings MT, Withers PJ, Acta Metall. Mater. 40 (1992) 2361-2373.

Almer JD, Cohen JB, Winholtz RA, Metall. Mater. Trans. 29A (1998) 2127-2136.

Andersson M, Persson C, Melin S, Int. J. Fatigue 28 (2006) 1059-1068.

ASTM Standard E647-99: Standard Test Method for Measurement of Fatigue Crack-Growth Raters, 2000 Annual Book of ASTM Standards, Vol. 03.01, pp. 591-630.

Bachmann V, Munz D, J. Testing. Eval. 4 (1976) 257-260.

Barabash R, Mater. Sci. Eng. A 309 (2001) 49-54.

Barabash RI, Ice GE, Liu W, Einfeldt S, Roskowski AM, Davis RF, J. Appl. Phys. 97 (2005) 013504.

Barabash R, Gao YF, Sun YN, Lee SY, Choo H, Liaw PK, Brown DW, Ice GE, Philos. Mag. Lett. 88 (2008) 553-565.

Barenblatt GI, The mathematical theory of equilibrium cracks in brittle fracture. Advances in applied mechanics VII. Academic Press (1962) 55-129.

Bathias C, Vancon M, Eng. Fract. Mech. 10 (1978) 409-424.

Benoit D, Namdar-Irani R, Tixier R, Mater. Sci. Eng. 45 (1980) 1-7.

Bichler CH, Pippan R, Eng. Fract. Mech. 74 (2007) 1344-1359.

Borrego LP, Ferreira JM, Pinho da Cruz JM, Costa JM, Eng. Fract. Mech. 70 (2003) 1379-1397.

Bourke MAM, Dunand DC, Ustundag E, Appl. Phys. Lett. 74 (2002) 1707-1709.

Brahma KK, Dash PK, Dattaguru B, Int. J. Fatigue 11 (1989) 37-41.

Bucci RJ, Thakker AB, Sanders TH, Sawtell RR, Staley JT, ASTM STP 714 (1980) 41-78.

Budiansky B, Hutchinson JW, J. Appl. Mech. 45 (1978) 267-276.

Carlson RL, Kardomateas GA, Bates PR, Int. J. Fatigue 13 (1991) 453-460.

Christensen RH, Metal Fatigue, New York: McGraw-Hill (1959).

Clarke CK, Cassatt GC, Eng. Fract. Mech.9 (1977) 675-88.

Codrington J, Kotousov A, Eng. Fract. Mech. 76 (2009) 1667-1682.

Croft MC, Jisrawi NM, Zhong Z, Holtz RL, Sadananda K, Skaritka JR, Tsakalakos T, Int. J. Fatigue 29 (2007) 1726-1736.

Dabayeh AA, Topper TH, Int. J. Fatigue 17 (1995) 261-269.

Damri D, Knott JF, Int. J. Fatigue 15 (1993) 53-60.

Davidson DL, Eng. Fract. Mech. 38 (1991) 393-402.

Daymond MR, Priesmeyer HG, Acta Mater. 50 (2002) 1613-1626.

Daymond MR, Young ML, Almer JD, Dunand DC, Acta Mater. 55 (2007) 3929-3942.

Dias A, Lebrun JL, Bignonnet A, Fatigue Fract. Eng. Mater. Struct. 22 (1999) 133-144.

Donald DR, Anderson WE, Crack Propagation behavior of some airframe materials. In: Proceedings of the Crack Propagation Symposium - Cranfield, England, vol 2. (1961) 375-441.

Donald K, Paris PC, Int. J. Fatigue 21 (1999) 47-57.

Dougherty JD, Srivatsan TS, Padovan J, Eng. Fract. Mech. 56 (1997) 167-187.

Dugdale DS, J. Mech. Phys. Sol. 8 (1960) 100-104.

Elber W, ASTM STP 486 (1971) 230-242.

Ellyin F, Ozah F, Int. J. Fract. 143 (2007) 15-33.

Faber KT, Evans AG, Acta Metall. 31 (1983) 565-574.

Fellows LJ, Nowell D, Int. J. Fatigue 26 (2004) 1075-1082.

Fleck NA, Smith IFC, Smith RA, Fatigue Eng. Mater. Struct. 6 (1983) 225-239.

Fleck NA, Eng. Fract. Mech. 25 (1986), 441-449.

Gan D, Weertman J, Eng. Fract. Mech 15 (1981) 87-93.

Gao YF, Bower AF, Model. Simul. Mater. Sci. Eng. 12 (2004) 453-463.

Goel HS, Chand S, J. Eng. Mater. Technol. 116 (1994) 168-172.

Gray GT, Williams JC, Thompson AW, Metall. Trans 14 A (1983) 421-433.

Gray TGF, Mackenzie PM, Int. J. Fatigue 12 (1990) 417-423.

Guvenilir A, Breunig TM, Kinney JH, Stock SR, Acta Mater. 45 (1997) 1977-87.

Haase JD, Guvenilir A, Witt JR, Stock SR, Acta Mater. 46 (1998) 4791-4799.

Haynes online literature, HASTELLOY C-2000 alloy brochure:
http://www.haynesintl.com/pdf/h2118.pdf.

Hertzberg RW, Deformation and Fracture Mechanics of Engineering Materials, Fourth Edition (1996).

Hornbogen E, Acta Metall. 26 (1978) 147-152.

Hou CY, Charng JJ, Int. J. Fatigue 18 (1996) 463-474.

Huang EW, Barabash RI, Wang Y, Clausen B, Li L, Liaw PK, Ice GE, Ren Y, Choo H, Pike LM, Klarstrom DL, Inter. J. Plasticity 24 (2008) 1440-1456.

Hung YC, Bennett JA, Garcia-Pastor FA, Michiel M Di, Buffiere JY, Doel TJA, Bowen P, Withers PJ, Acta Mater. 57 (2009) 590-599.

Ice GE, Larson BC, Yang W, Budai JD, Tischler JZ, Pang JWL, Barabash RI, Liu W, J. Synchrot. Radiat. 12 (2005) 155-62.

Ice GE, Pang JWL, Barabash RI, Puzyrev Y, Scr. Mater. 55 (2006) 57-62.

Irwin GR, J. Appl. Mech. 24 (1957) 361-364.

Jame MN, J. Eng. Des. 9 (1998) 329-342.

James MN, Hattingh DG, Hughes DJ, Wei L-W, Patterson EA, Fonseca JQD, Fatigue Fract. Eng. Mater. Struct. 27 (2004) 609-622.

Johnson HH, Materials Research and Standards 5 (1965) 442-445.

Jones RE, Eng. Fract. Mech. 5 (1973) 585-604.

Khor KH, Buffiere JY, Ludwig W, Sinclair I, Scr. Mater. 55 (2006) 47-50.

Kim JK, Shim DS, Int. J. Fatigue 25 (2003) 335-342.

Knott JF, Pickard AC, Metal Science 11 (1977) 399-404.

Lam YC, Lian KS, Theor. Appl. Fract. Mech. 12 (1989) 59-66.

Larson AC, Von Dreele RB, General Structure Analysis System, Los Alamos National Laboratory Report LAUR 86-748 (2004) 160.

Larson BC, Yang W, Ice GE, Budai JD, Tischler JZ, Nature 415 (2002) 887-90.

Lee CS, Livne T, Gerberich WW, Scripta Metall. 23 (1986) 1137-1140.

Lee SY, Barabash RI, Chung JS, Liaw PK, Choo H, Sun Y, Fan C, Li L, Brown DW, Ice GE, Metall. Mater. Trans. 39A (2008) 3164-3169.

Lee SY, Choo H, Liaw PK, Oliver EC, Paradowska AM, Scr. Mater. 60 (2009) 866-869.

Liaw PK, Leax TR, Williams RS, Peck MG, Acta Metall. 30 (1982) 2071-2078.

Liaw PK, Leax TR, Williams RS, Peck MG, Metall. Trans. 13A (1982) 1607-1618.

Liaw PK, Saxena A, Swaminathan VP, Shih TT, Metall. Trans. 14A (1983) 1631-1640.

Liaw PK, Burke MG, Saxena A, Landes JD, Metall. Trasns. 22A (1991) 455-468.

Logsdon WA, Liaw PK, Eng. Fract. Mech. 24 (1986) 737-751.

Louat N, Sadananda K, Duesbery M, Vasudevan AK, Metall. Trans A 24 (1993) 2225-2232.

Makabe C, Purnowidodo A, McEvily AJ, Int. J. Fatigue 26 (2004) 1341-1348.

Marshall DB, Cox BN, Acta Metall. 35 (1987) 2607-2619.

McClung RC, Sehitoglu H, Eng. Fract. Mech. 33 (1989) 237-252.

Miller KJ, Proc. Inst. Mech. Eng. Part L-J, Mater.-Des. Appl. 217 (2003) 1-21.

Mughrabi H, Acta Metall. 31 (1983) 1367-79.

Newman, JC, Mechanics of Fatigue Crack Growth. Special Technical Publication. Philadelphia ASTM 590 (1976) 282-301.

Newman JC Jr., ASTM STP 748 (1981) 53-85.

Nguyen O, Repetto EA, Ortiz M, Radovitzky RA, Int. J. Fract. 110 (2001) 351-369.

Ohji K, Ogura K, Yoshiji O, Eng. Fract. Mech. 7 (1975) 457-464.

Okayasu M, Chen DL, Wang ZR, Eng. Fract. Mech. 73 (2006) 1117-32.

Pacey MN, James MN, Patterson EA, Exp. Mech. 45 (2005) 42-52.

Pang JWL, Holden TM, Mason TE, Acta Mater. 46 (1998) 1503-1518.

Paris PC, Gomez MP, Anderson WP, A Rational Analytic Theory of Fatigue, The Trend in Engineering 13 (1961) 9-14.

Pineau AG, Pelloux RMN, Metall. Trans. 5A (1974) 1103-1112.

Pommier S, Eng. Fract. Mech. 69 (2002) 25-44.

Pommier S, De Freitas M, Fatigue Fract. Eng. Mater. Struct. 25 (2002) 709-722.

Ramos MS, Pereira MV, Darwish FA, Motta SH, Carneiro MA, Fatigue Fract. Eng. Mater. Struct. 26 (2003) 115-121.

Reynolds AP, Fatigue Fract. Eng. Mater. Struct. 15 (1992) 551-562.

Rice JR. ASTM STP 415 (1967) 247-309.

Rietveld HM, J. Appl. Crystallogr. 2 (1969) 65-71.

Roberson LJ, Kirk MT, ASTM STP 982 (1988) 230-246.

Robertson SW, Mehta A, Pelton AR, Ritchie RO, Acta Mater. 55 (2007) 6198-6207.

Rokhlin SI, Kim JY, Int. J. Fatigue 25 (2003) 51-58.

Roychowdhury S, Dodds RH Jr., Fatigue Fract. Eng. Mater. Struct. 28 (2005) 891-907.

Rushton PA, Taheri F, Mar. Struct. 16 (2003) 517-539.

Sadananda K, Vasudevan AK, Metall. Trans 29A (1998) 1359-1360.

Sadananda K, Vasudevan AK, Holz RL, Lee EU, Int. J. Fatigue 21 (1999) 233-246.

Sadananda K, Ramasqamy DNV, Phil. Mag. A 81 (2001) 1283-1303.

Sarma VS, Jaeger G, Koethe A, Int. J. Fatigue 23 (2001) 741-45.

Saxena A. Nonlinear Fracture Mechanics for Engineers, Boca raton, FL: CRC Press, (1998).

Schijve J, Fatigue crack propagation in light alloy sheet materials and structures. NRL Report MP 195, National Aeronautical and Astronautical Research Institute, Amsterdam, Holland, (1960).

Schijve J, Broek D, Aircraft Eng. 34 (1962) 314-316.

Schijve J, Fatigue crack propagation in alloy sheet material and structure. In: Advances in Aeronautical Sciences, vol 3, Pergamon, (1962) 387-408.

Schijve J, Arkema WJ, Report VTH-217, Delft University of Technology, The Netherlands (1976).

Schijve J, ASTM STP 982 (1988) 5-34.

Schwalbe KH, Hellman D, J. Test. Eval. 9 (1981) 218-220.

Serebrinsky S, Ortiz M, Scr. Mater. 53 (2005) 1193-1196.

Shih TT, Wei RP, Eng. Fract. Mech. 6 (1974) 19-32.

Shin CS, Hsu SH, Int. J. Fatigue 15 (1993) 181-192.

Singh KD, Khor KH, Sinclair I, Acta Mater. 54 (2006) 4393-4403.

Skorupa M, Fatigue Fract. Eng. Mater. Struct. 21 (1998) 987-1006.

Smith J, Bassim MN, Liu CD, Holden TM, Eng. Fract. Mech. 52 (1995) 843-851.

Steuwer A, Edwards L, Pratihar S, Ganguly S, Peel M, Fitzpatrick ME, Marrow TJ, Withers PJ, Sinclair I, Singh KD, Gao N, Buslaps T, Buffiere JY, Nucl. Instr. Meth. Phys. Res. B 246 (2006) 217-225.

Sunder R, Int. J. Fatigue 7 (1985) 3-12.

Sun Y, Choo H, Liaw PK, Lu Y, Yang B, Brown DW, Bourke MAM, Scr. Mater. 53 (2005) 971-975.

Sun Y, An K, Tang F, Hubbard CR, Lu YL, Choo H, Liaw PK, Physica B 385 (2006) 633-635.

Suresh S, Zamiski GF, Ritchie RO, Metall. Trans. 12 A (1981) 1435-1443.

Suresh S, Scr. Metall. 16 (1982) 995-999.

Suresh S, Eng. Fract. Mech. 18 (1983) 577-593.

Suresh S, Fatigue of Materials, Second Edition, Cambridge University Press (1998).

Su X, Gu M, Yan M, Fatigue Fract. Eng. Mater. Struct. 9 (1986) 57-64.

Toda H, Sinclair I, Buffiere JY, Maire E, Khor KH, Gregson P, Kobayashi T, Acta Mater. 52 (2004) 1305-1317.

Trebules VW Jr., Roberts R, Hetzberg RW, ASTM STP 536 (1973) 115-146.

Tzou JL, Suresh S, Ritchie RO, Acta Metall. 33 (1985) 105-116.

Ungar T, Dragomir I, Revesz A, Borbely A, J. Appl. Crystallogr. 32 (1999) 992-1002.

Vallellano C, Vazquex J, Navarro A, Dominguez J, Fatigue Fract. Eng. Mater. Struct. 32 (2009) 515-524.

Vasudevan AK, Sadananda K, Louat N, Scr. Metall. Mater. 27 (1992) 1673-1678.

Vasudevan AK, Sadananda K, Louat N, Mater. Sci. Eng. A 188 (1994)1-22.

Wallhead IR, Edwards L, Poole P, Eng. Fract. Mech. 60 (1998) 291-302.

Wang CH, Rose LRF, Newman JC Jr., Fatigue Fract. Eng. Mater. Struct. 25 (2002) 127-139.

Ward-Close CM, Blom AF, Ritchie RO, Eng. Fract. Mech. 32 (1989) 613-638.

Wheatley G, Hu XZ, Estrin Y, Fatigue Fract. Eng. Mater. Struct. 22 (1999) 1041-1051.

Wheeler OE, J. Bas. Eng. 94 (1972) 181-186.

Willenborg JD, Engle RM, Wood HA. A crack growth retardation model using an effective stress concept, Report AFFDL-TM-71-1-FBR, Dayton (OH): Air Force Flight Dynamics Laboratory, Wright–Patterson Air Force Base (1971).

Withers PJ, Bennett J, Hung YC, Preuss M, Mater. Sci. Technol, 22 (2006) 1052-1058.

Withers PJ, Rep. Prog. Phys. 70 (2007) 2211-2264.

Wong SL, Bold PE, Brown MW, Allen RJ, Fatigue Fract. Eng. Mater. Struct. 23 (2000) 659-66.

Xia SM, Gao YF, Bower AF, Lev LC, Cheng YT, Int. J. Solids Struct. 44 (2007) 3685-3699.

Yisheng W, Schijve J, Fatigue Fract. Eng. Mater. Struct. 18 (1995) 917-921.

Yuen BKC, Taheri F, Int. J. Fatigue 28 (2006) 1803-1819.

Zhang J, He XD, Du SY, Inter. J. Fatigue 27 (2005) 1314-1318.

Zhang X, Chan ASL, Davies GAO, Eng. Fract. Mech. 42 (1992) 305-321.

Vita

Soo Yeol Lee was born in Jecheon, South Korea, on July 8, 1976. He obtained the B.S. degree in Materials Science and Engineering from Korea University, Seoul, South Korea in 2003 and earned his M.S. degree in Materials Science and Engineering from Seoul National University, Seoul, South Korea in 2005. In August 2005, he started his Ph.D. study in Materials Science and Engineering at The University of Tennessee, Knoxville and completed his Doctor of Philosophy degree in Materials Science and Engineering in December 2009.